Environmental Impacts on Dielectric Barrier Discharge Plasma Actuators

Einfluss der Umgebungsbedingung auf Plasma-Aktuatoren mit dielektrischer Barriereentladung

Master-Thesis of Sebastian Bürkle, B.Sc., B.Sc.

Mai 2013

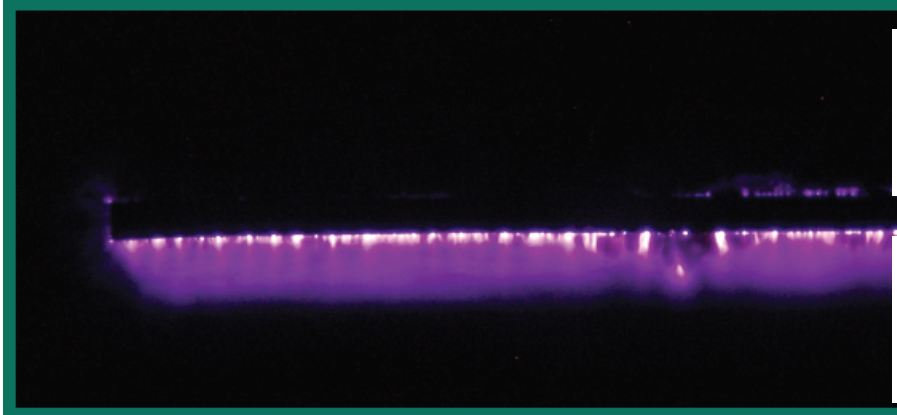

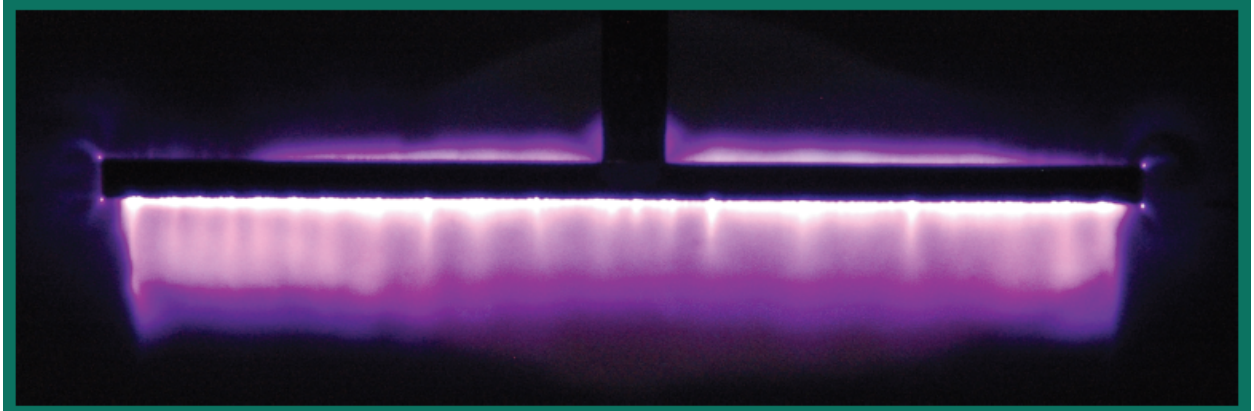

TECHNISCHE UNIVERSITÄT DARMSTADT

Department of Mechanical and Process Engineering
Center of Smart Interfaces
Drag and Circulation Control Group

Prof. Dr.-Ing. Cameron Tropea

Center of Smart Interfaces

Environmental Impacts on Dielectric Barrier Discharge Plasma Actuators
Einfluss der Umgebungsbedingung auf Plasma-Aktuatoren mit dielektrischer Barriereentladung

Vorgelegte Master-Thesis von Sebastian Bürkle, B.Sc., B.Sc.

1. Gutachten: Prof. Dr.Ing. Cameron Tropea
2. Gutachten: Dipl. Ing. Katrin Barckmann

Tag der Einreichung:

Erklärung zur Master-Thesis

Hiermit versichere ich, die vorliegende Master-Thesis ohne Hilfe Dritter nur mit den angegebenen Quellen und Hilfsmitteln angefertigt zu haben. Alle Stellen, die aus Quellen entnommen wurden, sind als solche kenntlich gemacht. Diese Arbeit hat in gleicher oder ähnlicher Form noch keiner Prüfungsbehörde vorgelegen.

Darmstadt, den May 21, 2013

(Sebastian Bürkle)

Abstract

Plasma actuators based on dielectric barrier discharge promise a bright future in aerodynamical applications. By creating a body force in the surrounding gas through plasma – gas interaction, plasma actuators, operated in quiescent air, induce a weak flow above their surface with a velocity of typically 5-8 m/s, the so called ionic wind. The ionic wind can influence the boundary-layer of any externally applied flow. Thus, plasma actuators are used for flow-control applications with a wide range of different flow velocities, temperatures and pressures.

In the present work, the impact of these environmental conditions on the power consumption, plasma length and resonance behavior of the plasma actuators is studied. It is shown that an increase of the temperature or decrease of the pressure favor the discharge, as they increase the plasma length and the power consumption for a constant voltage amplitude. During the experiments temperatures from ambient temperature up to 600 °C were tested and the pressure ranges from ambient pressure down to p = 0.11 bar. Scaling numbers and power laws were found to describe the impact of these parameters on the power consumption and plasma length. A hypothesis that the mean free path of the ions and electrons could be the dominant impact factor on the discharge was derived. Thus, the temperature and pressure dependence on the mean free path leads to the observed effects. Also, it is shown that the impedance of the plasma actuator, which is a product of an active and passive component of the actuators capacitance, is increased by an increasing temperature or decreasing pressure. This effects lead to a decrease of the resonance frequency of the circuit.
External flows with small velocities between 0 m/s and 21 m/s have no effect on the power consumption and resonance behavior of an actuator. High velocities decrease the power consumption and the impedance, as they reduce the discharge volume and relative discharge duration. These effects are shown in different experiments of a plasma actuator exposed to flow Mach numbers between 0.42 and 0.7.

The second part of this thesis focuses on the investigation of the environmental and voltage impact on filaments in the discharge that are caused by an instability in the discharge process. It is shown that increasing the pressure or flow velocity stabilizes the discharge and thus delays the onset of the formation of filaments towards higher voltages. The temperature seems to have no impact on the onset voltage. These effects are in good agreement with the predications by a theoretical model of the filaments. With the help of streak-camera images it is shown that the filaments only occur during the negative half-cycle. Increasing the voltage amplitude or temperature increases the spacing between the filaments, which typically ranges in between 2 mm and 4 mm. The same effect is achieved by decreasing the pressure. Measurements with a Pitot tube and particle image velocimetry show that the filaments increase the local velocity of the ionic wind by a factor of roughly 1.1 - 1.6. Thus, the ionic wind of a discharge with filaments looses its two-dimensional character and becomes three-dimensional. This effect may allow advanced flow-

control strategies, for example active vortex generation using the discharge filaments.

Kurzfassung:

Plasma-Aktuatoren mit dielektrischer Barriereentladung verheißen eine viel versprechende Zukunft in der Aerodynamik. Durch die Erzeugung einer Volumenkraft im Gas aufgrund der Plasma-Gas-Wechselwirkung können sie in ruhender Luft eine langsame Strömung von 5-8 m/s nahe ihrer Oberfläche erzeugen, den sogenannten ionischen Wind. Dieser ionische Wind kann die Grenzschicht einer beliebigen angrenzenden Strömung beeinflussen. Aus diesem Grund werden Plasma-Aktuatoren zur Strömungskontrolle auf die Eignung von Anwendungen mit unterschiedlichstem Druck, Temperatur oder Strömungsgeschwindigkeit untersucht.

In dieser Arbeit wurde der Einfluss dieser Umgebungsbedingungen auf den Leistungsverbrauch, die Plasmalänge und das Resonanzverhalten von Plasma-Aktuatoren untersucht. Es wird gezeigt, dass eine Erhöhung der Temperatur oder Absenkung des Drucks die Entladung verstärkt, da die Plasmalänge und der Leistungsverbrauch bei konstanter Spannung gesteigert werden. In den Experimenten dazu wird die Temperatur zwischen Umgebungstemperatur und 600 °C variiert und der Druck zwischen 0.11 bar und atmosphärischem Druck. Es zeigt sich, dass sich der Umgebungseinfluss unter diesen Bedingungen gut durch Exponentialgesetze und Skalierungskenngrößen beschreiben lässt. Daraus entstand die Hypothese, dass die mittlere freie Weglänge der Ionen und Elektronen der effektive Einflussparameter sein könnte, sodass die Temperatur- und Druckabhängigkeit der mittleren freien Weglänge zu den beobachteten Effekten führt. Zusätzlich wird gezeigt, dass die Impedanz des Plasma-Aktuators durch eine Erhöhung der Temperatur oder eine Verringerung des Drucks gesteigert wird. Die wachsende Impedanz führt zu einer Verringerung der Resonanzfrequenz des Gesamtsystems.
Eine externe Strömung mit einer Geschwindigkeit zwischen 0 m/s und 21 m/s scheint keinen Einfluss auf Resonanzverhalten und Leistungsverbrauch des Aktuators zu haben. Hohe Strömungsgeschwindigkeiten hingegen verringern den Leistungsverbrauch und die Impedanz, da sie das Entladungsvolumen und die Dauer der Entladungen pro Zyklus reduzieren. Diese Effekte werden mit Hilfe verschiedener Experimente, bei denen ein Plasma-Aktuator einer Strömung mit Machzahlen zwischen 0.42 und 0.7 ausgesetzt wird, gezeigt.

Der zweite Teil dieser Arbeit wittmet sich dem Einfluss der Umgebungsbedingungen und Spannungsparameter auf Filamente in der Entladung, die durch eine Instabilität im Entladungszyklus entstehen. Es wird gezeigt, dass eine Erhöhung der Temperatur oder der Strömungsgeschwindigkeit einen stabilisierenden Einfluss haben und daher die Entstehung der Filamente zu höheren Spannungsamplituden verschieben. Die Temperatur scheint in erster Näherung keinen Einfluss auf auf Entstehungsspannung zu haben. Diese Effekte sind in guter Übereinstimmung mit den Vorhersagen aus vorab entwickelten theoretischen Modellen. Mit Hilfe von Streak-Kamera Aufnahmen wird gezeigt, dass die Filamente nur in der Entladung des negativen Halbzyklus entstehen. Eine Erhöhung der Temperatur oder der Spannung sorgt dafür, dass sich der Abstand der Filament im Bereich zwischen 2 mm und 4 mm erhöht. Ein verringerter Druckes hat den gleichen Effekt.

Geschwindigkeitsmessungen mit einem Pitotrohrs und Particle Image Velocimetry zeigen, dass die Filamente die Geschwindigkeit des ionischen Windes lokal um den Faktor 1,1-1,6 erhöhen können. Daher ist der verliert der ionische Wind der Entladung mit Filamenten sein zweidimensionales Verhalten und erzeugt ein dreidimensionales Strömungsfeld. Dieser Effekt ermöglicht möglicherweise Konzepte zur fortgeschritten Strömungskontrolle, wie zum Beispiel aktive Wirbelerzeugung durch die Verwendung der Filamente.

Environmental Impacts on Dielectric Barrier Discharge Plasma Actuators

TECHNISCHE UNIVERSITÄT DARMSTADT

Einfluss der Umgebungsbedingung auf Plasma-Aktuatoren mit dielektrischer Barriereentladung

Center of Smart Interfaces

Degree program M.Sc. Mechanical Engineering for Sebastian Bürkle, B.Sc. B.Sc.
Supervisor: Dipl.-Ing. Katrin Barckmann
Start of thesis: October, 1st 2012

In recent years, Dielectric Barrier Discharge (DBD) plasma actuators have become a promising device for aerodynamic flow-control applications. The Drag and Circulation Control Group (DCC) of the Center of Smart Interfaces at TU Darmstadt uses the ionic wind induced by the plasma actuator to influence boundary-layer flows. The discharge of plasma actuators that induces the ionic wind is not completely understood yet. Studies of the group showed that the discharge is strongly influenced by the environmental parameters, e.g. ambient temperature, pressure and Mach number of the air flow.
Furthermore, preliminary studies showed equidistantly distributed filaments in cord-wise direction within the homogeneously glowing plasma at higher power levels. These filaments seem to be strongly dependent on the environmental conditions, too, and to have a great influence on the lifetime, power consumption and performance of the plasma actuators at higher power levels. The phenomenon lacks an analytical description and explanation as well as an experimental measurement of the environmental impact on the filaments. Also, it is desirable to find practical methods to prevent the negative effects on the performance of the actuators or, on contrary, to find a beneficial use of the filaments in flow-control applications.

Scope of work:

- The dependency of power consumption, resonance behavior, plasma length and performance of a plasma actuator on pressure will be investigated in a pressure chamber at different pressure levels.
- The dependency of power consumption, resonance behavior, plasma length and performance of a plasma actuator on temperature will be studied in different types of ovens or cooling chambers. Temperature levels between -10°C and 600°C will be used. New actuator designs have to be developed to withstand the high temperatures.
- The dependency of power consumption and performance on Mach number and pressure will be investigated in the trisonic wind-tunnel of the TU Darmstadt. High-speed streak camera images will show the interior structure of the discharge and its dependency on Mach number and pressure simultaneously.
- The origin of the large scale filaments will be studied in detail and a corresponding theory should be developed. A focus will be on the onset conditions for the development of the filamentary structures in the discharge and on the plasma physics involved. The theory will be compared to experimental results of the onset condition dependency on pressure, temperature and flow velocity.
- The influence of the filaments on power consumption of the actuator and a corresponding heating of the dielectric barrier will be studied.
- The influence of the filamentary structures on the velocity of the ionic wind should be investigated using a Pitot tube and Laser Doppler Anemometry (LDA) measurements.
- For different environmental and operation conditions, the dependency of the average distance between filaments will studied, since it is assumed that the filaments could lead to vortex generation in the flow due to the three-dimensional flow field.
- New strategies for the prevention of the filaments will be developed as well as new, robust actuator designs for the beneficial use of them.

Prof. Dr.-Ing. C. Tropea

Contents

List of Figures

1 Introduction

1.1 Motivation

A high voltage between two electrodes can partially ionize a surrounding gas and form a area of thin non-thermal plasma. The displacement of the charged particles in the plasma by the electric field can produce a net body force due to momentum transfer between the charged particles and surrounding neutral molecules and atoms. Depending on the arrangement of the electrodes, the body force can produce a local flow, the so called electric or ionic wind.
Since the ionic wind is a direct conversion of electric to kinetic energy, it is of special interest for aerodynamic research, especially in flow-control.

J. R. Roth [1] in 1997 first studied the influence of the ionic wind of a Dielectric Barrier Discharge (DBD) plasma actuator in an aerodynamic application, specifically boundary-layer control (Roth called it "“one atmosphere uniform glow discharge surface plasma"', OAUGDSP). The DBD plasma is an AC surface discharge plasma.
The arrangement of the electrodes in a DBD plasma actuator has been widely used in ozone generation applications before, as by Kogelschatz *et al.* [2].
The actuator consists of two electrodes, separated by a dielectric barrier that prevents the actuator from arcing. One electrode, the lower electrode, is grounded and encapsulated by the dielectric material (Kapton, Al_2O_3 etc.). The other electrode, usually called exposed or upper electrode, is exposed to a surrounding gas. A high AC voltage of sinusoidal, square, saw tooth or triangle wave type is applied to this electrode.

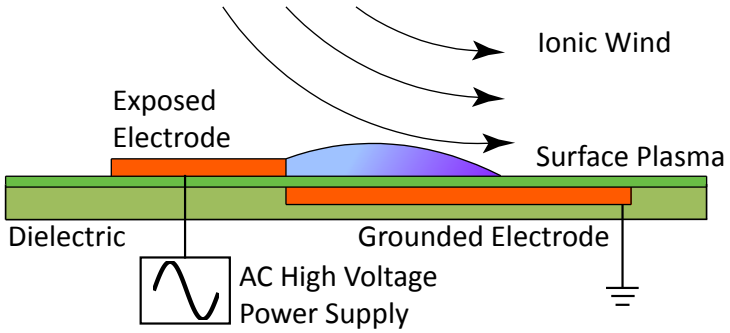

Figure 1.1: Design of a typical DBD plasma actuator

The electric field generates a discharge above the dielectric barrier resulting in a plasma. The ionic wind of this plasma creates a wall jet sheet along the exposed electrode with a momentum flow from the upper to the lower electrode and a velocity in a range of typically 5-8 m/s. As Roth showed, the wall jet can be used for flow control applications, such as separation control, by influ-

encing the boundary-layer of the flow around the actuator.

(a) (b)

Figure 1.2: Low-speed separation control on a wing profile with a DBD plasma actuator operated in an external airflow, according to Roth [3]. Image (a) shows the flow with the plasma actuator off and (b) with plasma actuator on. Without an actuator the flow separates from the wing and a recirculation zone arrises.

DBD plasma actuators are expected to improve the performance (higher angles of attack) [3], reduce the broadband noise [4] and minimize the fuel consumption (suppression of laminar-turbulence transition) [5] of future aircrafts.
In future applications, plasma actuators will have to operate in a wide range of different environmental conditions, ranging from a pressure of 0.25 bar and a temperature of -45 °C for actuators on civil airplane wings to 30 bar and 1500 °C for internal-flow applications, such as jet engine combustion chambers. The flow velocity in possible applications ranges from almost quiescent air to supersonic flow with military aircrafts.
Recent investigations have proven that the environmental conditions of the gas in which the discharge occurs have a strong influence on the discharge. Abe *et al.* [6], Benard *et al.* [7], Wu *et al.* [8] and Versailles *et al.* [9] showed that the pressure has an impact on the thrust and electric behavior of a plasma actuator. The impact of different temperature levels on a plasma actuators were studied by Versailles *et al.* [9]. Bernard showed in [7] that the effects of high altitude (low pressure and temperature) increase the discharge compared to ambient conditions. The power consumption and thus the discharge strength were higher for a given voltage amplitude in higher altitudes. Abe *et al.* [6] also described the impact of different gas species on the thrust. Barckmann *et al.* [10], Kriegseis *et al.* [11] [12] studied the impact of the flow on a plasma actuator separatly. They showed that not only the discharge of a plasma actuator has an influence on an applied airflow, but also the airflow can have an influence on the discharge in reverse. At higher Mach numbers, the air flow decreases the discharge and higher voltage amplitudes are necessary to maintain the same power consumption of the actuator.
Throughout this work, the impact of flow velocity, temperature and pressure will be studied systematicly.

1.2 Aim of this work

The first aim of this work is to investigate the impact of gas temperature, pressure and flow velocity on the discharge of a plasma actuator, independently of each other. This is done with different experimental setups, both qualitatively and quantitatively. The measure of comparison are the power-voltage characteristics, the plasma length and the resonance behavior of the actuators. Additionally, theories for the origins of some of the effects are provided.

In a previous work (Bürkle [13]), on which this thesis is based on, it was shown that large-scale filaments – instabilities of the discharge – can occur in the other wisely homogeneous gas discharge. According to a newly developed theory, the instabilities are influenced by gas velocity, pressure and temperature as well. Prior to this work it was shown that the impact of the gas velocity correspond to the prediction of the theory quite well.
The second aim of this work is to study the impact of gas velocity, pressure and temperature on the instabilities in further detail. The dependency of the onset-voltage for an instable development and the spacing between the filaments on the environmental conditions are studied.

As shown by Bürkle as well, the instabilities increase the velocity of the ionic wind locally. The third aim of this work is to measure this dependency in further detail and higher accuracy.

2 Theoretical model of plasma actuators

Throughout this chapter the theories necessary for the understanding of the environmental impact on plasma actuators, are provided. First, a general overview of the physics of gas discharges in plasma actuators is given. The second section is a short introduction into the current knowledge of the dependency of a plasma actuator on voltage parameters, such as impedance effects, power-voltage characteristics and scaling numbers. The third section describes the process that leads to instabilities in the plasma qualitatively and the onset conditions for an instable development quantitatively.
It is important to note that some parts of this chapter are adapted from Bürkle [13] with only minor variations.

2.1 Theory of plasma and gas discharges

The main properties of the plasma generated in the discharge of a plasma actuator are described next, followed by a short introduction to the main processes of a plasma discharge. Later, the discharge processes that occur in a DBD plasma actuator are described with a focus on streamer and corona discharge.

2.1.1 Classification of the dielectric barrier discharge plasma

In physics and chemistry, a plasma describes a mixture of partly or fully ionized atoms or molecules and electrons. The plasma state is commonly known as the fourth state of matter.
Plasmas span a wide range of temperatures and densities of charged particles with different physical and chemical properties and regimes. Thus plasmas can be found in various industrial and experimental applications and are subjects to a wide range of research projects. In order to provide a better insight into the discharges in DBD plasma actuators, a further distinction and classification of the DBD plasma is necessary.
At macroscopic scales, the concentrations of negative and positive charges in a plasma are approximately equal, thus the plasma is quasi-neutral. At microscopic scales, this is not necessarily the case. Space charges can form up, for example due to newly injected ions or electrons, externally applied electric or magnetic fields, or compression waves. The space charges attract either electrons or ions, since the plasma itself consists out of charges. Thus the space charge is compensated by the plasma macroscopically, and its electric field is shielded. According to Kegel [14] the poten-

tial of the space charge can be described as

$$\Phi(\mathbf{r}) = \frac{q}{r} e^{(-r/\lambda_D)} \tag{2.1}$$

i.e. the potential decays exponentially for distances greater than λ_D. λ_D is the Debye length, that defines the spatial range of the plasma, which can comprise a charge imbalance and characterizes the thickness of the sheath formed by the plasma around electrodes or walls. It is given by

$$\lambda_D = \sqrt{\frac{kT}{4\pi n_e e^2}} \tag{2.2}$$

with the plasma temperature T (or electron temperature in non-equilibrium plasma) and the electron density n_e. For non-thermal plasmas, the Debye length ranges from 10^{-4} to a few cm.

The DBD plasma is a non-equilibrium plasma, the ion temperature is significantly different from the electron temperature. The electron temperature, on one hand, ranges from one to ten eV, T_e=1..10 eV, where inelastic collision is relevant. The temperature of the ions, on the other hand, is in the order of the gas temperature and thus of the ambient temperature, $T_i \approx T_g \approx 300$ K. The charge number density n defines the number of charges per volume and ranges from 10^5 to 10^{13} cm^{-3}, according to Kriegseis [15]

Another parameter of interest in plasmas is the degree of ionization, that describes the ratio of the number density of ions n_i to the number density of the gas. The number density of the gas is the sum of the number density of neutral molecules n_n and that of ions.

$$\alpha = \frac{n_i}{n_i + n_n} \tag{2.3}$$

Since a surface DBD plasma is usually very thin (α=10^{-4}...10^{-3}«1) it can be assumed that the momentum transfer mainly occurs between charged and neutral particles and that momentum transfer between charged particles can be neglected. The mass of the electrons is significantly lower than that of ions and neutrals, thus the contribution of electrons to ionic wind can be neglected.
The charged particles drift along the direction of the electric field $\vec{E}$ superimposed with a random movement due to the collisions with neutrals [16]. The momentum transfer in the collisions slows the particles down. Thus the particles, on average, have a limited velocity $\vec{v}$ given by the strength of the electric field and their mobility μ

$$\mu_{e,i} = \frac{Ze}{m_{e,i}\nu_{e,i}} \tag{2.4}$$

with the charge number Z, the collision frequency of charges with gas particles ν and the ion and electron masses, m_i and m_e . Since the plasma is very thin, double ionization or electron attachment can be assumed to be negligible and thus Z is one. For this reason, the charge number is usually left out in literature. The average drift velocity is then

$$\vec{v}_{e,i} = \begin{cases} \mu_i \vec{E} & \text{for positively charged ions} \\ -\mu_{i,e}\vec{E}, & \text{for electrons and negatively charged ions} \end{cases} \tag{2.5}$$

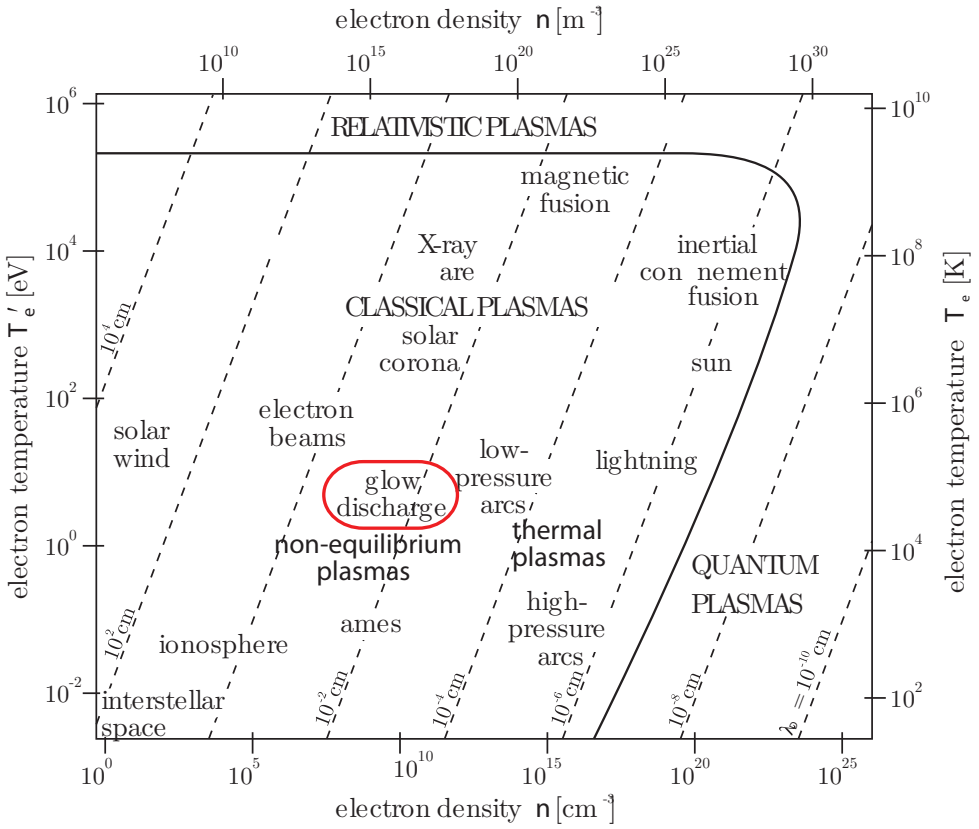

Figure 2.1: Two dimensional classification of the glow plasma in comparison to others, characterized by electron number density n and electron temperature T_e, analog to Kriegseis [15].

The kinetic energy of the ions is transfered to the neutral molecules during the collision and is responsible for the ionic wind.

The mass m_e of electrons is significantly smaller than the mass of ions and neutral molecules ($m_e/m_p = 1836$ for ionic hydrogen, mass ratios of 10^4 are typical for gas molecules or ions). Thus collisions of electrons with neutrals produce almost no momentum transfer. The mass of the ions, m_i, on the other hand, is in the order of the mass of the neutrals. Large amount of momentum can be transferred from the ions into the gas through elastic collision. Thus the ion movement is the main reason of the ionic wind. Since the ions loose most of their kinetic energy hereby, their temperature is in the order of the neutral gas temperature.

The mass m_e of electrons is significantly smaller than the mass of ions, which results in a higher mobility and thus average velocity. As soon as the kinetic energy of the electrons is sufficiently high for inelastic collision ≈ 1 eV, they can knock out valence electrons from the neutral gas. Thus, ions and free electrons are generated. The knocked-out electrons can also be accelerated in in the external electric field and knock-out further electrons. Through that process, an electron-avalanche is established, the so called *Townsend discharge*. At a certain voltage, the production of ions from the avalanche is high enough to maintain a self-sustaining discharge. This is due to the fact that these ions eject enough initial electrons from the surface for new avalanches. The self-sustainment of the discharge results in a sharp rise of the current for a given voltage. Paschen showed that the voltage V_b, necessary for this breakdown, is depended on the factor pd, with gas

pressure p and gap width d. He measured this dependency for various gases. The measurements yield the so called *Paschen curve* in Figure 2.2.

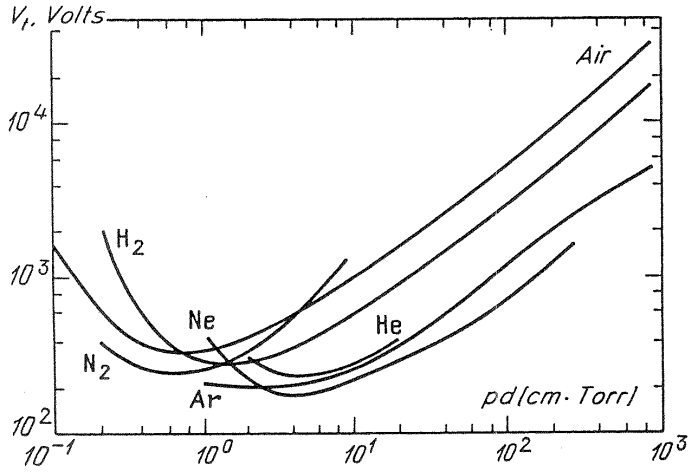

Figure 2.2: Breakdown voltages in various gases over a wide range of pd values, from [16]

2.1.2 Theory of the dielectric barrier discharge in a plasma actuator

The plasma actuator of Roth [1] creates a dielectric barrier surface discharge. This is different from the volume discharge of most gas discharge devices. The barrier prevents the gas discharge from arcing, even at ambient pressure. The charges produced in the discharge accumulate on the surface of the dielectric barrier and built up an electric field that reduces the voltage between exposed electrode and barrier. Thus, the discharge is self-limiting when the applied voltage is DC. Therefore, an AC sinusoidal voltage is used to maintain a long-lasting plasma discharge. The surface charges produced by the discharge during one half of the cycle are thus neutralized by those produced by the discharge in the other half-cycle and vice versa.

Kriegseis [15], who studied the charge-voltage characteristics of DB plasma discharges with the help of Lissajous-figures (see Figure 2.3 (b)), found only minor differences in the discharge behavior of both half-cycles. Thus, he treated them identically. Nevertheless, there are significant differences in the discharge of the two flanks, otherwise no net body force would be produced. All body force generated during one half-cycle of the periodic voltage would be reversed by the other half-cycle. In surface DBDs, positive and negative half-cycles have different types of discharges, as will be explained later.

As can be seen in Figure 2.4 where the monitored voltage and current of a DBD is shown, the discharge within a plasma actuator only occurs when the applied voltage increases or decreases, otherwise the potential of the surface charge built-up by the current ceases the discharge. After the voltage extremes, a dead-time without discharge follows, since there needs to be a minimal potential difference for a new, reversed breakdown, as it is the case in a Paschen-breakdown.

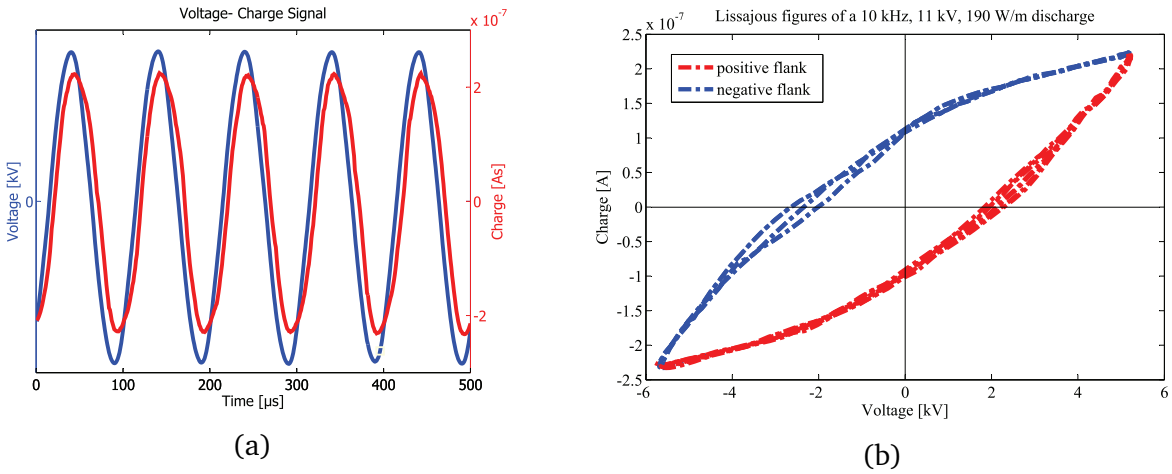

Figure 2.3: (a) Sinusoidal voltage and charge signal for a 10 kHz, 11 kV DB plasma discharge; (b) charge and voltage measurements plotted in a Q(t)-V(t) diagram. The trace of charge-voltage characteristics gives the corresponding so called Lissajous-figure of the discharge. The Lissajous-figure has an almond shap for surface discharges.

Wu [8] observed a transition between a continuous glow and a discontinuous, filamentary dis-

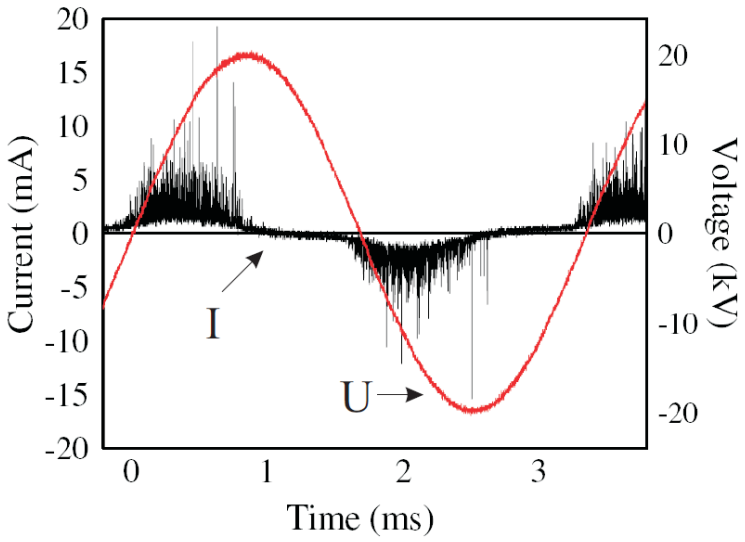

Figure 2.4: Voltage (red) and current (black) through the actuator for one discharge cycle, according to Pavon [17]. The current consists out of multiple peaks within a discharge cycle. The repetition period of these peaks is significantly less than a microsecond.

charge at very low pressures of 6 kPa. Choi [18] confirmed Wu´s experiments with the help of spectral analysis of the ions (identifying the transition point at 6.6 kPa instead of 6 kPa). At higher pressure levels, the current showed large peaks followed by a period without a discharge. The discharge obviously ends after a short time and restarts after a short pause. It is thus evident, that the discharge in a DBD plasma actuator consists out of multiple single peaks for atmospheric pressures. I studied these peaks intensively during my master-thesis. According to Benard *et al.* [19], the discharge in a DBD is composed out of two different regimes, dependent on the sign

of the voltage gradient applied to the actuator. For the negative half-cycle, i.e. the intervall from maximal to minimal voltage, Soloviev *et al.* [20] assumed the discharge to occur in a corona mode. Pavon *et al.* [21], Benard *et al.* [7] and Orlov *et al.* [22] proposed, that the discharge in the positive half-cycle, i.e. the intervall from minimum to maximum, is made out of streamers.
During the next subsections, the physics and properties of streamers and corona-discharge will be discussed as they are described in the literature mentioned above [19] [20] [21] [22] and by Raizer [16].

Positive micro-scale filaments

The physics of the streamer mode, usually described in an DC volume discharge, as in Pavon [17] or Raizer [16], will be discussed for an AD surface discharge herein.
During the case of the positive half-cycle, the exposed electrode is the anode. Electrons from the background ionization are pulled towards the anode by the electric field and start an avalanche. When the electric field of the avalanche is too small to significantly distort the applied electric field before reaching the anode, the discharge remains in the Townsend regime. As soon as the space charge exceeds a critical value, photo-ionization becomes dominant and the transition to a streamer occurs. This value corresponds to $e^{\alpha_i d} \geq N_{crit} \approx 10^{-8}$, according to Meek´s criterion, as mentioned by Meek in [23]. When the space charge exceeds that value, a steamer develops with the following steps:

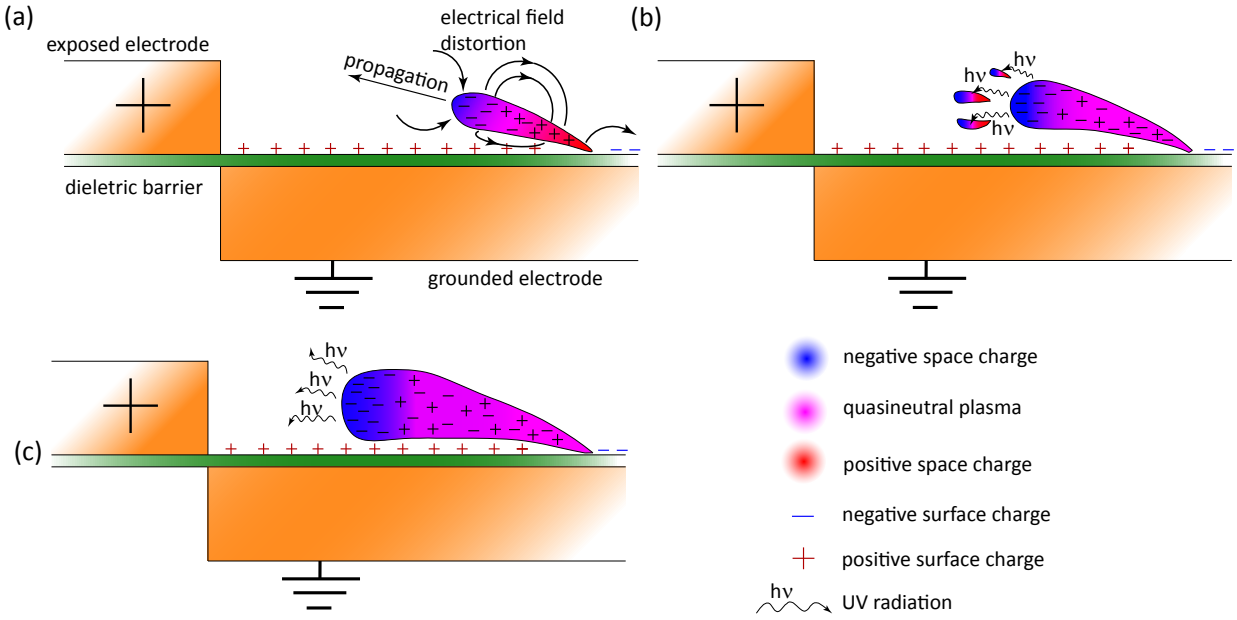

Figure 2.5: Development of anode-directed streamers. (a) initial Townsend-avalanche at t_1 (b) streamer transition through photo-ionization and creation of miniature-avalanches at $t_2 > t_1$ (c) streamer and creation of new miniature avalanches at $t_3 > t_2$

- Primary avalanche:
  A streamer first starts with an anode-directed avalanche by multiplication of primary elec-

trons, growing rapidly from the barrier towards the anode. When the applied electric field is sufficiently strong or the discharge long enough, the space charge of the avalanche dipole – electrons at the head, ions at the tail – becomes large enough to create an electric field that is in the order of the applied electric field. The effective electric field becomes a superposition of the external and the dipole field, seriously enhancing the field between the head and the anode while reducing the field between the head and the barrier (Figure 2.5a).
UV-radiation, emitted by the avalanche-head through recombination and relaxation of excited states, can randomly ionize the gas ahead of the discharge through photo-ionization. The knocked-out electrons lead to smaller Townsend avalanches, growing towards the anode (electrons) and towards the main-avalanche head (ions) simultaneously (Figure 2.5b). This is the transition to a streamer.

- Growth of anode-directed streamers:
  When the miniature avalanches spread to the avalanche head, the ions of the miniature avalanche tail mix with the electrons of the main discharge head, leading to a quasi-neutral plasma. The head of the miniature avalanche becomes part the "new" head of the avalanche. The main growth mechanism of the discharge changes from avalanche to radiation of UV-light, photoionization and growth of miniature avalanches. The discharge is now of streamer type. Since the miniature avalanches appear at stochastic positions due to the random nature of the photo-ionization, the streamers branch out into the direction of the miniature avalanches.
  According to Moreau *et al.* [25], the growth velocity of the avalanches is about 10^4 m/s. Since the main processes in streamers are photo-ionization and propagation of UV-radiation, the growth velocity is limited by their speed and the time needed for the photo-ionization process. The UV-radiation propagates with the speed of light, and the photo-ionization is a rather rapid process, thus the streamer growth velocity is in the order of 10^6 m/s, according to Pavon [17]. This is much faster than the avalanche discharges, and the growth of a streamer occurs within one to a few nanoseconds.

- Growth of cathode-directed streamers: For moderate gaps and moderate voltages, the avalanche-to-streamer transition takes place only when the primary avalanche has reached the anode. The avalanche has not grown strong enough and the space charge field is not sufficient to create miniature-avalanches before the avalanche has reached the anode [17]. When the avalanche reaches the anode, the ions in the tail of the avalanche remain in the gap, due to their slow drift motion ((a) in Figure 2.6). The space charge of the positive ions can significantly distort the applied electric field, as it was the case for anode-directed streamers. The strong field in connection with the UV-radiation triggers micro-avalanches by accelerating electrons ahead of the ion head towards the streamer (b). In this case the streamer is cathode-directed

- Filament discharge phase:
  Once the streamer (anode- or cathode-directed) spreads through the gas gap, the breakdown phase is finished and the discharge phase along the original streamer path begins. The ions remaining in the gap form a thin filament made out of weakly ionized plasma ((c) in Figure 2.6). In the DBD, the dielectric barrier prevents the transition from the filament to an arc due

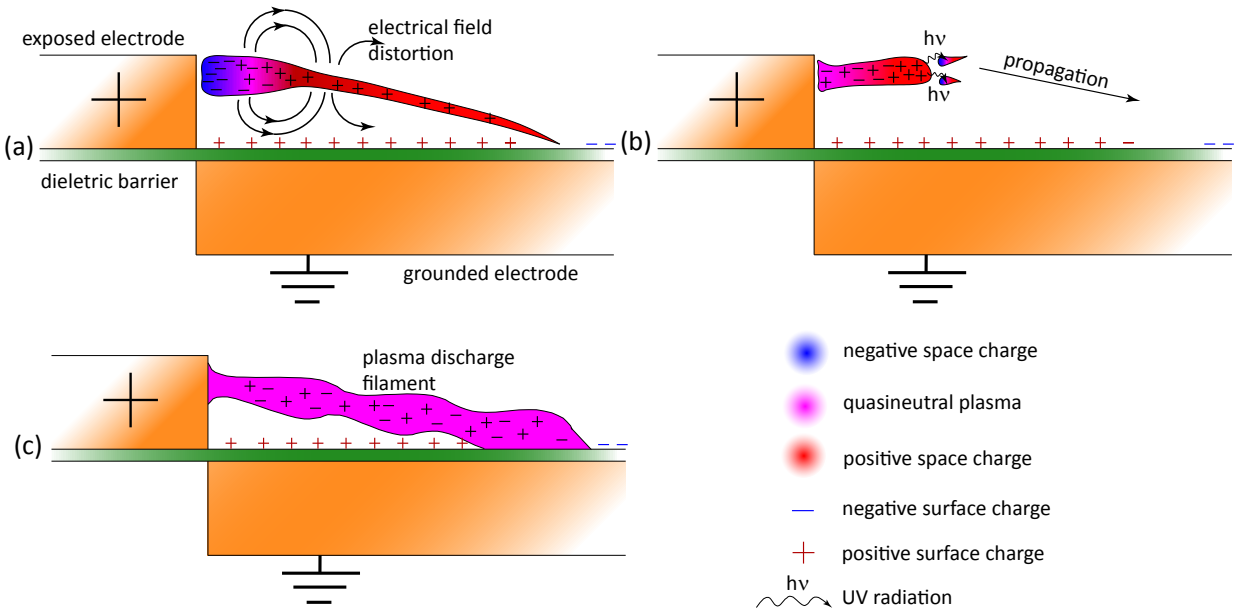

Figure 2.6: Process steps of cathode-directed streamers and discharge filament. (a) end of a Townsend-avalanche on the anode at t_1 (b) streamer transition through photo-ionization and creation of miniature-avalanches in the distorted electric field in front of the ion space charge at $t_2 > t_1$. (c) Filament discharge after (anode- or cathode-directed) streamer breakdown.

to the built up of a surface charge on the barrier. Thus the lifetime of the filament is limited to a few tens of nanoseconds. Afterwards most of the ions move to the barrier, becoming neutralizing with electrons from the surface. The discharge ends and can only be restarted by increasing the externally applied electric field.

Since both, the avalanche and the streamers, underlie stochastic processes, discharge filaments can appear independently at several positions of the actuator. The repetition period of the discharge is significantly less than a microsecond, as can be seen in Figure 2.4, and in the order of a few megahertz. Thus the discharge seems as an homogeneous glow to the unaided eye.

Negative micro-scale filaments

According to an semi-analytical analysis of Soloviev [20], the discharge in the negative flank is made out of a corona discharge. The theory is supported by high-speed images taken by Bernhard [19] and Orlov [22] and by force measurements by Forte [26] and Leonov [24]. The latter two showed a higher force production during the negative half-cycle, which presumably results from the negative ions in the corona discharge.

According to Soloviev, the ionization mainly occurs in a small zone between the upper electrode and a virtual anode, composed out of positive ions. This zone is called the cathode layer. Inside the cathode layer electron avalanches ionize neutral gas molecules. The electric field within the layer

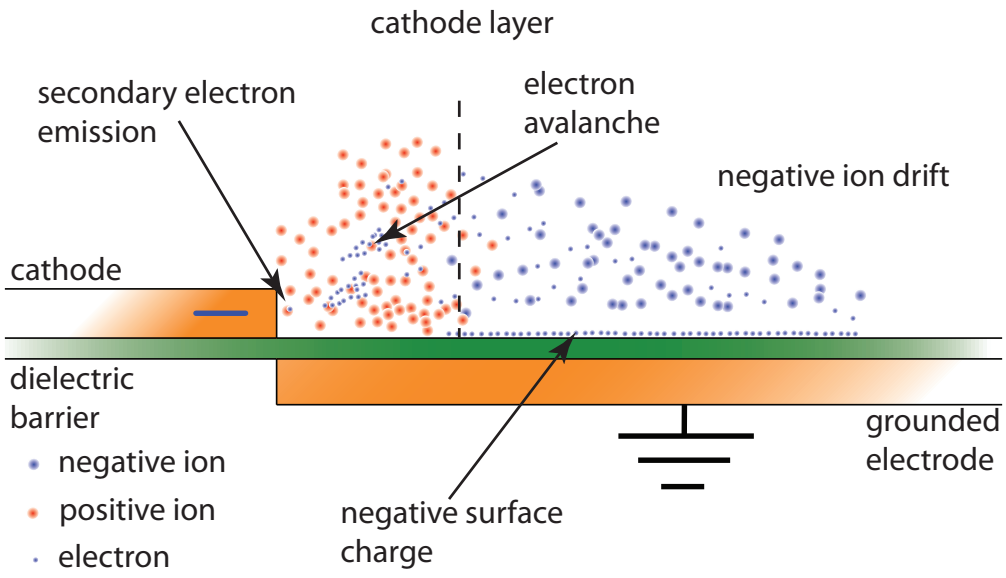

Figure 2.7: Corona discharge in a plasma actuator as described by Soloviev [20]. The streamwise extension of the cathode layer is strongly disproportionate, usually its streamwise extension is in the order of a few μm.

is intensified, whereas weakened in the region between the virtual anode and the point of lowest potential, the end of the lower electrode. Within the layer, the positive ions (mainly N_2^+) drift towards the cathode and knock out electrons from the surface through secondary electron emission and simultaneously become neutralized. The electrons are accelerated within the intensified field. Subsequently, they knock out electrons from neutral gas molecules and create an avalanche discharge. After they crossed the virtual anode, they drift along the dielectric barrier towards the end of the grounded electrode, until they reach the end of the negative surface charge. On their path through the weakened electric field they can create negative ions out of neutral molecules due to electron attachment. The negative ions, mainly O^- ions, drift within the weakened electric field behind the virtual anode and contribute to the ionic wind.
The electrons on the dielectric barrier built up a weakening electric field, contrary to the externally applied electric field. Thus the discharge ends when enough charge is transferred from cathode to the dielectric barrier which reduces the effective field to zero. The remaining ions recombine or drift out of the discharge zone. The downstream drift of the negative ions is the main source of the ionic wind. The positive ions reduce the ionic wind, since they drift upstream. Nevertheless, since the cathode layer containing the positive ions is very thin, its contribution to the wind is negligible.

The discharge is very similar to a negative DC corona discharge. The difference is in its transient nature: Since the surface charge on top of the barrier and the shielding positive ions built up an electric field opposed to the external one, the discharge is ceased within a short time. To restart the discharge, the voltage difference has to exceed the breakdown voltage again. It is expected that the formation velocity of a single corona-pulse is one order of magnitude lower than that of a single streamer.

In summary, it can be said, the discharge in a plasma actuator is made out of single micro-scale filaments with a very short duration. According to current research, the discharge is dominated by streamers in the positive half-cycle and by a corona-discharge in the negative half-cycle.

2.2 Impact of electrical parameters on plasma actuators

The power consumption dependency of plasma actuators on voltage amplitude and frequency can be described by a power law $P \propto V^{\eta} \cdot f^{\mu}$. According to Kriegseis [12] and Roth *et. al.* [27], the exponent η takes values between 2 and 4 for sufficiently high voltage amplitudes. Kriegseis determined it to be 7/2. The parameter μ is usually determined as close to 1, since an increase in the frequency linearly increases the discharge cycles per time. When the shape of the area enclosed by the cyclogram remains unchanged, an increase of the discharge per time linearly increases the energy consumed per time by the actuator, i.e. the power consumption. Experimental results confirm that theory. An increase in the plasma actuator length L also increases the power consumption linearly, when side effects are negligible. This dependencies can be combined in a power law, such as

$$\frac{P}{V^{7/2} \cdot f \cdot L} \propto \Theta \tag{2.6}$$

Θ depends on the actuator design and most likely on the environmental conditions. A low Θ means that a high voltage amplitude or frequency is needed in order to have high power consumption. Therefore, actuator concepts or environmental conditions with high Θ values are favorable from an efficiency point of view.

Generally, any electrical circuit including capacitive and inductive elements, such as a high-voltage generator with a plasma actuator connected, has a particular resonance frequency f_{res} and resonance behavior. At resonance frequency, low input voltages lead to a high output voltage on the plasma actuator. It is therefore reasonable to choose the resonance frequency to be the voltage frequency.

The resonance frequency of the circuit mainly depends on the load connected to it, i.e. the plasma actuator. Yang *et al.* [28] studied the influence of voltage parameters on the resonance behavior of a discharge device. For increasing voltage amplitudes, they identified a reduction of the resonance frequency. Figure 2.8 shows the resonance curve of a high-voltage generator – plasma actuator circuit for different input voltages, as will be shown in chapter 4. Obviously, the resonance frequency and the shape of the curve depend on the input voltage. As indicated by the black curve, the resonance frequency decreases for higher voltage amplitudes. A system initially aligned with the resonance frequency can thus be detuned by only increasing the voltage. Therefore, the plasma actuator with discharge consists not only out of a passive component (actuator), but also of an active component (discharge), also shown quantitativly by Kriegseis. They both contribute to the resonance behavior. In contrast to the passive component, the capacity of the discharge component changes actively with input voltage. The decrease of the resonance frequency at higher voltage amplitudes is probably due to an increase in the discharge length and volume. A larger volume is ionized and a larger number of ions is moved within the discharge volume. Due to the larger ionized volume, a higher charge can be stored within the actuator. Thus, the capacitance of

the active component is higher and the resulting resonance frequency smaller.

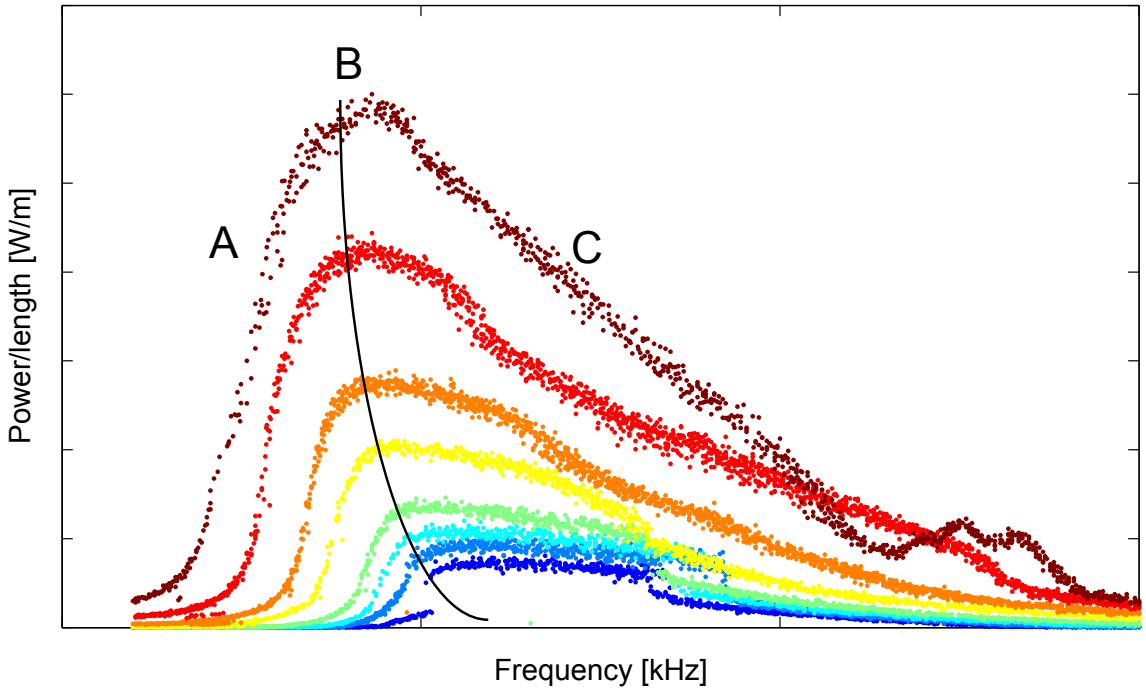

Figure 2.8: Resonance curves of a high-voltage generator - plasma actuator circuit.

The resonance curve obviously has three different sections:

(A) *Cliff:* For frequencies less than resonance frequency, the curve shows a very strong increase of the power consumption for small variations of the frequency. This section is not suitable for uncontrolled experiments including voltage amplitude or power consumption, since small variations in the frequency lead to significant variations in these parameters. The voltage amplitude behavior is instable in this section, too, due to the decrease of the resonance frequency with amplitude. A highly-dynamical controller might use this effect for high-performance voltage control. Without such a controller a stable section of the resonance has to be chosen.

(B) *Resonance plateau:* At resonance frequency, the slope of the resonance curve is very small. Thus, this section is well suitable for experiments. Also, for a given input-voltage to the high-voltage generator, the power consumption is highest here. For experiments with significant changes in voltage amplitude it is meaningful to choose a frequency slightly above resonance frequency in order to maintain in the stable section.

(C) *Curve back:* Above resonance frequency, the curve shows a slow decrease of the power consumption with increasing frequency. Since the slope is negative and small variations in the voltage amplitude damp out, this section is usable for both uncontrolled and controlled experiments.

Given the increase of discharge volume and ion number lead are the main origin of the decrease in resonance frequency at higher voltage amplitudes, as considered above, the environmental condi-

tions should have a significant impact on the resonance behavior. This will be studied in section 4.

2.3 Theory of discharge-instabilities

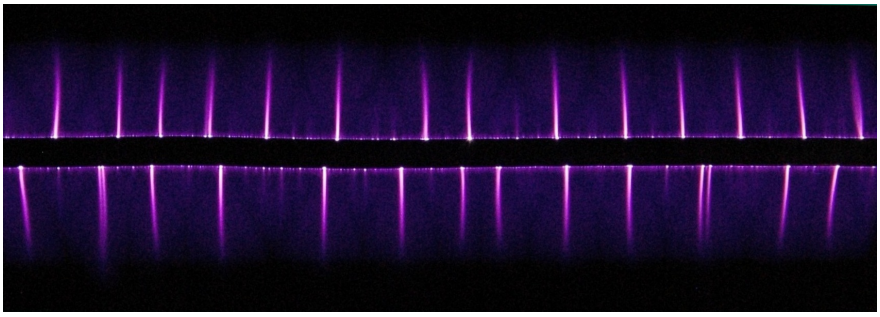

Figure 2.9: Image of large-scale filaments in the glow discharge of a two sided symmetric DBD plasma actuator.

Several researchers, like Pavon *et al.* [21] and Brauer *et al.* [29], directly observed large, long-lasting filamentary structures in the otherwise homogeneously glowing plasma for certain environmental conditions and applied voltages. The filaments are of technical interest, since they significantly damage the actuators due to massive heating and electro erosion of the dielectric barrier. During electro erosion, molecules of the dielectric barrier are detached from the solid state material due to ion collission. They also seem to induce a tree dimensional flow. These facts, on one hand, show the necessity to prevent the filaments. On the other hand, it seems that the velocity of the ionic wind within the large-scale filaments is significantly larger than in between the filaments. Thus the filaments might be of practical use for flow control, for example in bondary layer control using vortices generated by the three-dimensional flow.
Different workgroups tried different approaches to explain these filaments, like assuming them to be streamers or avalanche-discharges. Brauer *et al.* [29] simulated the glow discharge for high voltages in the streamer regime, and observed filamentary structures of large-scales. Nevertheless, they did not take the photo-ionization by UV-radiation into account in their simulations, which is shown to be the main mechanism for streamer formation. Also, the properties gained from the simulation, such as the lifetime of the filaments, were different from those observed in the experiments of this work. Streamers, for instance, are much smaller and have a significantly shorter lifetime than the large-scale filaments. Also, the streamers ramify along their path due to the random nature of the photo-effect, but the large-scale filaments are straight. Thus, the theory of Brauer *et al.* does not explain the large-scale filaments sufficiently.

The following sections describes these filaments, introducing the theory developed in the previous work [13] based on a work of Chirokov [30]. Within that theory, the filaments are assumed as thermal instabilities in the plasma with corresponding physical laws. The theory is supported by experiments, where the environmental impact on the instabilities is studied and compared with the theory.

2.3.1 Theory of glow discharge instabilities

Instabilities (i.e. a catastrophic increase of initially small perturbations) grow in a non-steady process. The system either comes to a new, more stable state, or a steady state is never achieved, so that a periodically changing process is established.
Instabilities can be described through a chain of casual links of various processes involved in the cycle. Two types of instabilities in plasma are given in literature of volume discharges, longitudinal and transverse instabilities with respect to the electric field vector. The longitudinal instabilities, so called stritations, are manifests of ionization oscillations and waves. A stritated discharge may be caused by stepwise ionization, the maxwellization of the electron distribution function, and by any agent causing enhancement in longitudinal inhomogenities [16]. Since stritations have only been observed in volume discharges and not in dielectric barrier discharges, the focus in this section will be on transverse glow discharge instabilities, caused by thermal instabilities.

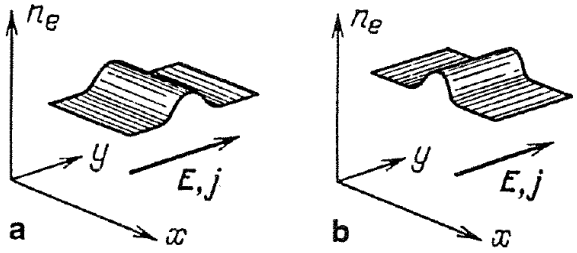

Figure 2.10: Longitudinal (a) and transverse (b) plasma instabilities with respect to the electric field vector, according to Raizer [16]

2.3.2 Description of the transverse thermal instability theory

The most common type of instabilities in a gas discharge plasma under atmospheric pressure is the so called thermal instability. Since they arise at high power levels, they limit the power of the active medium of CO_2 lasers. The topic of thermal instabilities for DC and RF discharges was thus subject to considerable research effort in the past, for instance by Velikhov [31], Chirokov [30] and Raizer [16]. Velikhov [31] and Chirokov [30] developed theories of the transition between stable glow discharge and the instabilities for a volume discharge. Starting from that theory, a theory of the instabilities in surface dielectric barrier discharges can be developed, as will be described in the following.

A stable glow discharge is never fully homogeneous. Geometrical imperfections in the setup of the actuator, such as sharp points in the electrodes or scratches in the dielectric barrier cause a slightly enhanced electric field in some areas of the discharge compared to others. Those inhomogeneities trigger a chain of processes, that lead to thermal instability when the electric field is sufficiently high. In detail, the processes steps of the chain are:

1. Imperfections in the actuator setup lead to a slightly increased electric field strength $\delta E \uparrow$.

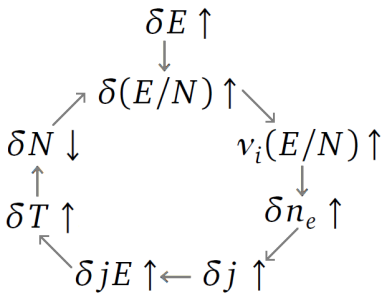

Figure 2.11: chain of process steps that lead to instability

2. An increase in the electric field obviously increases the reduced electric field $\delta(E/N) \uparrow$ (i.e. electric field over gas density).

3. An increase in the reduced electric field leads to a higher ionization coefficient α_i, since, according to Lagmich [32], α_i is a strictly monotonic increasing function of the reduced electric field. Higher ionization coefficients lead to an increase in the ion-production rate $\tilde{\nu}_i(E/N) = \alpha(E/N)/v_d$, and thus to an increased production rate of electrons. With a higher production rate of electrons the electron density δn_e increases

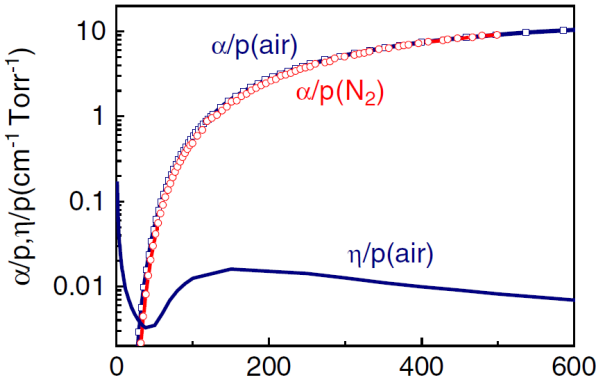

Figure 2.12: Reduced ionization α/p and attachment ν/p coefficients as function of the reduced electric field, according to Lagmich *et al.* [32]. The reduction was made with the pressure p instead of the gas density N, but p and N are linearly dependent through the ideal gas equation p=NkT.

4. Since the electric current density $j = nE$ in the discharge is mostly due to electron drift, an increase in the electron density n_e causes the current density to rise $\delta j \uparrow$. This happens only if the electric field E does not decrease simultaniously due to the higher consumed power, thus for highly stable external power supplies.

5. The higher electric current density leads to an increase in the dissipated power in the plasma $\delta jE \uparrow$.

6. Since most of the power consumption in a DBD plasma actuator is dissipated into heat (see Roth [3]), an increase in the power consumption obviously increases the gas temperature $\delta T \uparrow$.

7. With increasing temperature of the gas under constant pressure, the gas density $\delta N \downarrow$ decreases simultaneously, according to the ideal gas law p=NkT.

8. When the gas density decreases, the reduced electric field $\delta(E/N) \uparrow$ increases. The chain continues with the third step.

Imperfections in the actuator are not necessarily the origin of the instability, also fluctuations in temperature and density are possible triggers. Therefore the chain does not need to start with the first step.

The fourth and fifth steps of the chain exhibit the origin of an upper limit, where instable development ceases: when the power dissipated in the filaments exceeds the power delivered by the external circuit, the instable heating comes to an end. The instable development can be prevented by decreasing the electric field strength at the onset of instabilities.

2.3.3 Equation of the thermal balance of plasma

In order to prevent instabilities and the complications associated with them, it is necessary to understand under which conditions an instable process is triggered. In order to develop a stability criterion, the following assumptions can be made:

- A DBD is be considered to be created in an external airflow, as it is the case for common plasma actuator applications. The electric field within the actuator is assumed to be homogeneous. This is not necessarily the case, but can be assumed locally in a good approximation.
- The pressure is constant within the gas volume.
- All electrical energy is dissipated into heat within the gas volume. This approximation is valid, since only a small fraction of the input power (typically of the order of 0.1%, see [3]) is converted into kinetic motion of the gas.

The energy balance between the heat transfer (second term on the right side) and the dissipated electrical power (first term on the right side) can be written as:

$$c_p \rho \frac{dT}{dt} = j \cdot E - c_p \rho (T - T_0) \cdot \nu_{dc} \tag{2.7}$$

where T_0 is the temperature of the surrounding gas flow, c_p the heat capacity of the gas at constant pressure and ν_{dc} denoting the heat removal-frequency. The term on the left side describes the heating of the neutral gas. The heat-removal frequency ν_{dc}, a factor that describes how quickly heat is removed out of the control volume, is:

$$\nu_{dc} = \frac{\chi}{\Lambda_T^2} + \frac{2 \cdot u}{\Delta x} \tag{2.8}$$

The first term in equation 2.8 is the heat removal due to diffusion, the second term the heat transfer due to convection along the actuator. In the convective term, Δx is the plasma extension and u the velocity of the surrounding airflow. Since the released heat, on average, is transferred only half of the plasma length (due to molecular movement), the length has to be divided by two.
The diffusive term is the ratio of he thermionic conductivity $\chi = \frac{\Lambda}{N c_p}$ and a form factor Λ_T. The form factor has the dimension of a length and has to be calculated numerically for a DBD actuator geometry. Most importantly, it is constant for a given actuator geometry and can thus be assumed as a constant here.
A steady-state temperature is reached when the dissipated power corresponds to

$$j \cdot E = c_p \rho (T - T_0) \cdot \nu_{dc} \tag{2.9}$$

With the help of the frequency of heating ν_h, equation 2.7 can be rewritten in a simpler form:

$$\frac{dT}{dt} = T \cdot \nu_h - (T - T_0) \cdot \nu_{dc}, \tag{2.10}$$

whereas ν_h is a factor that describes how quickly heat is dissipated into the gas by the external power supply:

$$\nu_h = \frac{\gamma - 1}{\gamma} \cdot \frac{j \cdot E}{p} \tag{2.11}$$

with γ being the adiabatic index. Thus, the frequency of heating is just dependent on the input-power of the system and the pressure.

The second equation necessary for the determination of a stability criterion is the electron-density balance-equation:

$$n_e = \frac{\nu_i(E/N) - \nu_a(E/N)}{k_r} \tag{2.12}$$

with the coefficients for ionization and electron attachment ν_i and ν_a respectively, and the recombination rate k_r. The coefficients are only dependent on the reduced electric field E/N (see Lagmich [32]).
The variation of the logarithm of this function yields

$$\frac{\delta n_e}{n_e} = \frac{ln(\nu_i(E/N) - \nu_a(E/N))}{ln(E/N)} \cdot \left(\frac{\delta E}{E} - \frac{\delta N}{N} \right) \tag{2.13}$$

The factor

$$\nu^* = \frac{ln(\nu_i(E/N) - \nu_a(E/N))}{ln(E/N)}$$

is called logarithmic sensitivity and describes the sensitivity of the production rate is under variation of the reduced electric field.

The third important law is the ideal-gas law p=NkT. The variation of the law with the assumption of constant pressure yields

$$\delta p = k(T\delta N + N\delta T) = 0 \Rightarrow \frac{\delta N}{N} = -\frac{\delta T}{T} \tag{2.14}$$

The last equation necessary for a full description of the system is the variation of the rate of heat removal frequency with respect to variation of the electron density and electric-field strength. The variation of eqn. 2.11 yields

$$\frac{\delta \nu_h}{\nu_h} = \frac{\delta(jE)}{jE} = \frac{\delta(n_e E^2)}{n_e E^2} = \frac{E^2\delta n_e + 2n_e E\delta E}{n_e E^2} = \frac{\delta n_e}{n_e} + 2\frac{\delta E}{E} \tag{2.15}$$

$$\Rightarrow \frac{\delta \nu_h}{\nu_h} = \frac{\delta n_e}{n_e} + 2\frac{\delta E}{E} \tag{2.16}$$

The second equality in eqn. 2.15 is not self-evident and has to be discussed in detail. The current in a plasma can be written as $j = en_e\mu_e E$ under the given assumptions. With the help of eqn. 2.4, the formula can be rewritten as $jE = e^2 n_e E^2/(m_e\nu_e)$. The second equality in eqn. 2.15 directly results from $jE = e^2 n_e E^2/(m_e\nu_e)$ under the assumption that the collision frequency ν_e is approximately constant under variation of temperature. The assumption is valid, since the variation of factors in the varied product $\nu_e(T) = N(T)v(T)\sigma_{tr}$ have opposite signs and partially cancel each other out, according to Raizer [16] (with v being the velocity of random motion and σ_{tr} the cross section of elastic collision).

Combining equations 2.13, 2.14 and 2.16 with equation 2.7 finally produces the equation for thermal fluctuations:

$$\frac{d\delta T}{dt} = \delta T(\nu_h\nu^* + \nu_h - \nu_{dc}) + \nu_h(\nu^* + 2)T\frac{\delta E}{E} \tag{2.17}$$

Assuming the drop of the electric field strength across the plasma column to be fixed ($\Rightarrow \delta$ E = 0), an exponential Ansatz of $\delta T \propto \exp(\Omega$ t) solves the differential equation. This yields

$$\Omega = \nu_h\nu^* + \nu_h - \nu_{dc} \tag{2.18}$$

Even if $\delta E \neq 0$, the same result for Ω is achieved, when $\delta E/E$ is constant.
If the exponent Ω is greater than zero, $\Omega > 0$, the function grows exponentially and thus leads to instabilities. Therefore the system becomes instable for

$$\begin{aligned} \Omega = \nu_h\nu^* + \nu_h - \nu_{dc} &> 0 \\ \Rightarrow \nu_h = \frac{\gamma - 1}{\gamma}\cdot\frac{n_e\cdot E^2}{p} &> \nu_{dc}/(1+\nu^*) \\ \Rightarrow n_e E^2 > \nu_{dc}/(1+\nu^*)\cdot p\cdot\frac{\gamma}{\gamma-1} & \end{aligned} \tag{2.19}$$

or, with the help of the gas law

$$n_e E^2 > \nu_{dc}/(1+\nu^*)Nc_p T. \tag{2.20}$$

Since ν_{dc} is not dependent on temperature, an increase of the cooling rate stabilizes the process. This can be performed through a higher flow rate of the surrounding medium or a lower temperature.

3 Experimental setup

The experimental setups used for the investigations on the environmental impact on the discharge of plasma actuators are described in the following sections. The first section explains the power supply and the plasma actuator itself. For this work, a new type of plama actuators was developed in order to resist the high temperatures of the experiments. In the second section, the experimental setup of flow-velocity-impact measurements are explained, such as the *Trisonic Wind Tunnel with variable Mach Number*, the *Small Eiffel Wind Tunnel* and the streak camera for capturing high-speed images of the discharge. The third section presents the setup of pressure-related experiments, as the fourth does for temperature-related experiments. The setup of the experiments regarding the impact of the environment on instabilities is explained in section five. The sixth and last section describes the setup of the *Particle Image Velocimetry* (PIV) - System for measuring the velocity of the ionic wind precisely. The results of all experiments will be described in chapter 4.

3.1 Plasma actuator setup

In the following two subsections, the high-voltage power supply and the plasma actuator geometry are explained in detail. The third subsection describes the measurement of the high-voltage and the determination of the power consumed by the plasma actuator.

3.1.1 High-voltage generation

The plasma actuators need a supply of high-voltage with an alternating voltage of 3-20 kV and 1-20 kHz in order to create a discharge. The high-voltage power supply used during all experiments is the *MiniPuls 2.1*, except those on the impact of the flow velocity. For the flow velocity experiments, *MiniPuls 2.0* was used. Both *MiniPuls* devises are from *GBS Elektronik GmbH* they are identical, accept the integrated signal generation of *Minipuls 2.1* can be used optional, and thus both HV generators have the same principle of operation. The principle will explained on the example of *MiniPuls 2.1* since, in contrast to *MiniPuls 2.0*, the voltage amplification circuit and the oscillating circuit are installed on separate circuit boards. *MiniPuls 2.1* consists out of a *bridge* and a *transformer cascade*. In order to generate an AC voltage of radio frequency, the bridge is connected to a *Hameg HMF 2525* arbitrary signal generator that delivers a $\pm$ 5 V rectangle signal. The operation frequency of the signal has to be twice the frequency of the desired high-voltage output.
The main electrical input power of the bridge is generated by a *EA-PS 3032-05 B* 32 V DC laboratory power supply unit by *EA Elektro-Automatik GmbH & Co. KG*. Within the bridge, this voltage is modulated with the signal-generator frequency though an oscillating circuit made out of several capacitors and coils. Thus the signal is alternating with the frequency given by half the signal

Figure 3.1: Bridge and transformer cascade of high-voltage generator *MiniPuls 2.1*.

generators when leaving the bridge. It is of low voltage and moderate current. Using *MiniPuls 2.1*, the voltage amplitude of that signal can be adjusted between 0% and 100% by another voltage signal, produced by a *NI USB-6009 Multifunction DAQ* by *National Instruments* which is controlled by a computer using *Labview*.
The voltage on the output of the bridge is fed into the transformer cascade. The cascade consists out of multiple coils. A tunable reactor coil helps to adjust the impedance in order to meet the load impedance. The impedance of the plasma actuator and the voltage supply have to be matched carefully, otherwise no clean sinusoidal signal can be produced and the achievable voltage amplitude is decreased.

3.1.2 Plasma actuator geometry

Two different concepts of plasma actuators were used during the experiments. The first one is already established in the *Drag and Circulation Control Group* at the TU Darmstadt. The second one is a newly designed type which was developed in order to resist the high temperatures during the experiments of this work.

Both plasma actuators are made out of two copper electrodes, separated by a dielectric barrier. In the first concept, to which will be referred as *Kapton actuator* throughout this work, the dielectric barrier is made out of the polyimide *Kapton*, created by attaching two sheets of Kapton tape over another. It has a thickness of 0.33 mm. The dielectric barrier of the second concept, to which will be referred as *ceramic actuator*, is made out of an alumina (Al_2O_3) plate. The thickness of the plate is 0.38 mm and thus comparable to that of the Kapton actuator. The main difference between Kapton and alumina is the higher dielectric constant of alumina ($\sim$10 compared to $\sim$3.5). A higher permittivity usually leads to a greater dissipation of electric energy in the barrier and thus higher temperature. Nevertheless, the alumina was chosen as a second configuration as it able to resist significantly higher temperatures ($\sim$1200 °C) than Kapton ($\sim$200 °C). This is important for the temperature measurements. The thickness of all electrodes is 35 μm. The electrodes of the Kapton actuator are made out of self-adhesive copper-tape. The glue of the tape,

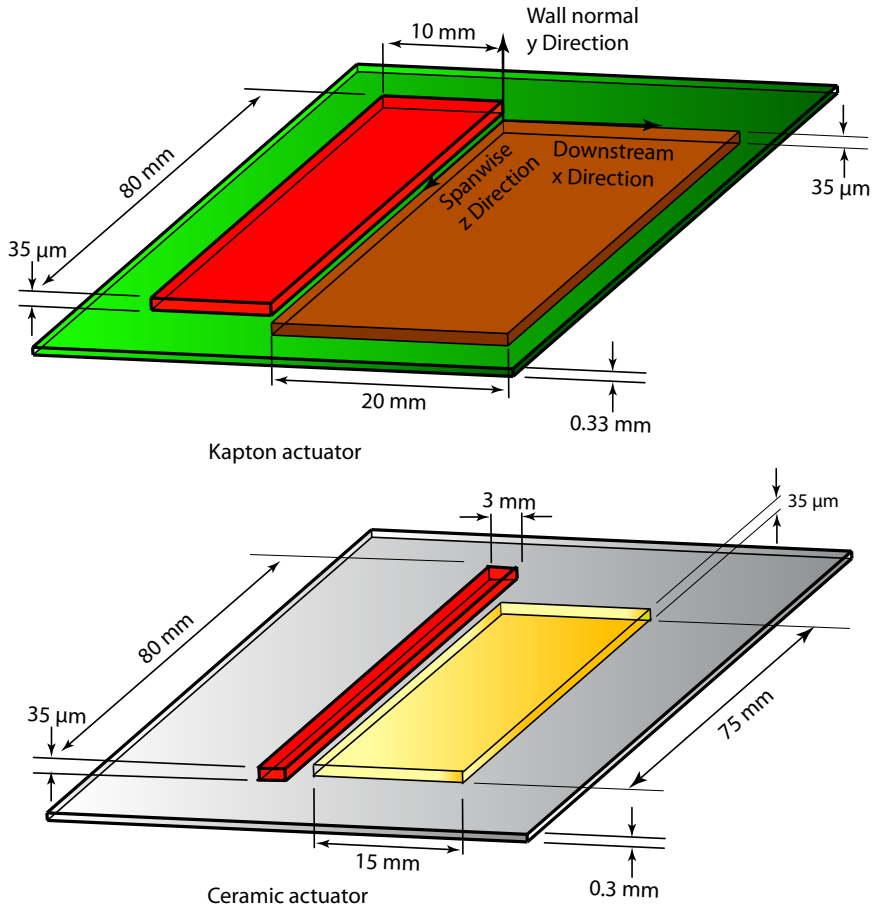

Figure 3.2: Geometry of the *Kapton actuator* (top), the *ceramic actuator* (bottom) and the used coordinate system. The coordinate origin is on top of the dielectric, at the contact line of upper and lower electrode.

unfortunately, begins to dissolve at temperatures above 150 °C. Therefore, a heat-proof glue by *Ulfalux Lackfabrick GmbH* was used instead. This was the most simple actuator design that resists high temperatures. Enormous effort was spend into the creation of *low temperature cofired ceramic* (LTCC) actuators that should be able to resist higher temperatures, but this technology did not lead to proper results yet. The geometry of both actuator configurations can be seen in Figure 3.2. They have slightly different dimensions due to spatial restrictions. The most important difference is the shorter lower electrode of the ceramic actuator due to limitations of the alumina plate. Nevertheless, they are very similar. The Kapton actuator was used during all velocity impact experiments, the ceramic actuator during all pressure and temperature impact experiments.

The temperature experiments required a new design for a separate holder of the ceramic actuator, since wires cannot simply be braced onto the electrodes. The soldering material would melt during the experiments. Therefore, the actuator is fixed by six screws onto an insulation ceramics plate. Two of the screws go through the plate, such that wires can be clamped on them at the backside. The electrodes are clamped in between the screws and the plate as well. This allows a

good electrical contact between the wires and the electrodes and the actuator is held in an upright position for optical experiments.

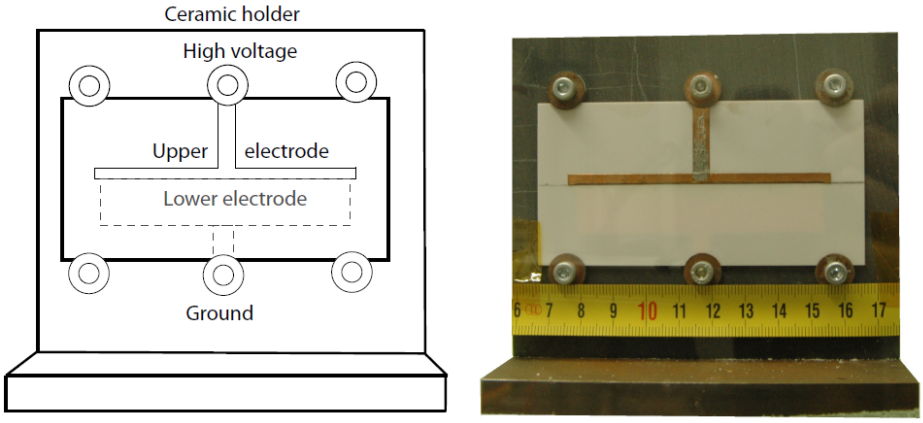

Figure 3.3: Geometry of the ceramic actuator holder for pressure and temperature experiments (left). Picture of the holder with actuator (right).

3.1.3 Determination of power consumption and voltage

The high-voltage of the plasma actuator is measured using a *TestTec HVP-15HF* high-voltage probe during the velocity experiments and a *PinTek HVP-39pro* during the temperature measurements. The electrical power consumption is determined with the help of a probe capacitor in the circuit. The low-voltage probes measuring the voltage drop across the capacitor are a *Tectronix P2220* and a *LeCroy PP06A*, respectively. The analog voltage signals are recorded and sent to a PC using a *PicoScope 4262* PC oscilloscope by *pico technologies*. The data processing is performed by *Labview*. Through the measurement of both, the high-voltage and the charge at the plasma actuator, the power consumption of the actuator can be derived using a method that was established by Bürkle in [13]. The power consumption during each measurement point i can be determined through

$$P_i = U_i \cdot \frac{Q_{i+1} - Q_{i-1}}{2\Delta t}, \tag{3.1}$$

The power consumption is averaged over two to three voltage periods in order to gain the mean power consumption using

$$\overline{P_i} = \frac{1}{N} \sum_{i}^{N} U_i \cdot \frac{Q_{i+1} - Q_{i-1}}{2\Delta t}, \tag{3.2}$$

For further information on the determination of the power consumption, see Bürkle [13].

3.2 Setup of experiments on flow velocity impact

Throughout this section, the setup of the experiments regarding the impact of the flow velocity on plasma actuators is described. First, a small overview over the experiments and the aims of those is given. In the second subsection, the two wind tunnels used during the experiments, the *Trisonic Wind Tunnel with variable Mach Number* TVM150 and the *Small Eiffel Wind Tunnel* (Eiffel), are explained. The third subsection describes the streak camera that is used to capture high-speed images of the discharge in the flow.

3.2.1 Experiments and aims

The first aim of the experiments on the flow velocity is to identify the impact of the flow on the power consumption of a actuator. Thus, the power consumption is recorded while the plasma actuator is used in a wind tunnel. In a first set of experiments, the power consumption-voltage characteristics of a Kapton actuator are measured in the Small Eiffel Wind Tunnel for flow velocities between 0 m/s and 21 m/s.
In a second experiment, the influence of the flow on the resonance behavior will be measured directly. Barckmann *et. al* already found out, that a flow of Mach number of Ma=0.42 and a static pressure of p_{stat}=1.16 can reduce the consumption by 30% for a constant input-voltage [10]. This experiment is be repeated, but more attention is paid to the influence of a resonance shift of the system due to the influence of the flow. For this purpose, the TVM150 is used, since it is able to deliver sufficient velocities.
The biggest set of experiments is to measure the influence of the flow on the discharge itself, using a high-speed streak camera. In order to see a great difference to the discharge at quiescent air, the high velocity flow of the TVM150 is used for these experiments as well.

During the experiments of the environmental impact on the discharge-instabilities, two additional flow experiments are made at the Small Eiffel Wind Tunnel using the Kapton actuator. In the first one, the impact of the flow velocity on the onset-voltage for discharge-instabilities is measured. In the second experiment, the impact of the flow on the temperature distribution in the dielectric barrier, caused by the heat generation of the plasma actuator, is investigated.

The following list shortly lists all experiments:

- Experiments of flow impact on plasma
    1. Power consumption – voltage characteristics (Eiffel)
    2. Resonance effects (TVM150)
    3. Power consumption-voltage characteristic and resonance effects (TVM150)
    4. Impact on discharge with streak camera (TVM150)
- Experiments of impact on discharge-instabilities

1. Impact on onset-voltage (Eiffel)
2. Impact on temperature-distribution

3.2.2 Wind Tunnels

Small Eiffel Wind Tunnel:

In order to measure the influence of an external flow on the instabilities and the power voltage characteristics, the plasma actuator is placed into the test-section of the *Small Eiffel Wind Tunnel* of the TU Darmstadt. The tunnel is able to deliver an air flow with a free-stream velocity between 0 and 30 m/s. The test section dimensions are 240 x 180 mm with a length of 800 mm. The test section is designed for maximum optical accessibility from three sides. The turbulence intensity of the flow inside the test section is estimated to be approximately 0.7%. The actuator is mounted on one wind-tunnel wall, parallel to a window, for a good optical access.

Figure 3.4: Test section of the Small Eiffel Wind Tunnel, flow direction top to bottom.

Trisonic Windtunnel with variable Mach number (TVM150):

The trisonic wind tunnel TVM150 (Trisonic wind-tunnel with variable Mach number) of TU Darmstadt is an intermittently working blow-down wind tunnel driven by an 8 m^3 high-pressure tank of maximum 50 bar. The flow conditions of the TVM150 can range from Mach 0.4 to Mach 4. Additionally, the Reynolds number can be varied within a certain range by adjusting the pressure,

and hence the density in the test section. During the experiments, the subsonic flow configuration was used, capable of delivering a flow at a Mach number between 0.4 and 0.7.
The test section has a cross section of 150 mm by 150 mm with a length of about 2 m and is divided into two parts: the subsonic and the supersonic test section. During the experiments, the upper and lower test section walls are replaced with perforated walls with an opening ratio of 6%, to reduce disturbances and shock reflection at the tunnel wall at transonic flow.
The Mach number is adjusted with the semi-flexible Laval nozzle during supersonic working conditions. For the subsonic working conditions, the Mach number is regulated by using a pressure difference to a valve in the diffuser downstream of the test-section. The static pressure can be adjusted in the subsonic setup. The plasma actuator is mounted on a glass-fiber reinforced-plastic plate that is fixed on a lance into the flow. The plate is thin and has a sharp edge in order to reduce the influence of the boundary layer on the plasma actuator. Observation windows in both test section parts allow optical access along one axis for the streak camera. [33]
In the subsonic configuration, the TVM150 is able to deliver a constant flow for 45-90 s until the pressure tank is emptied.

Working condition	
Test section	
Length	2.0 m
Width and height	150mm
Cross section C	22500mm^2
Flow condition	
Reynolds number	$4.5 \cdot 10^5$ to $1.5 \cdot 10^6$
*related to $0.1 \cdot \sqrt{C}$	
Mach number	0.4 to 4

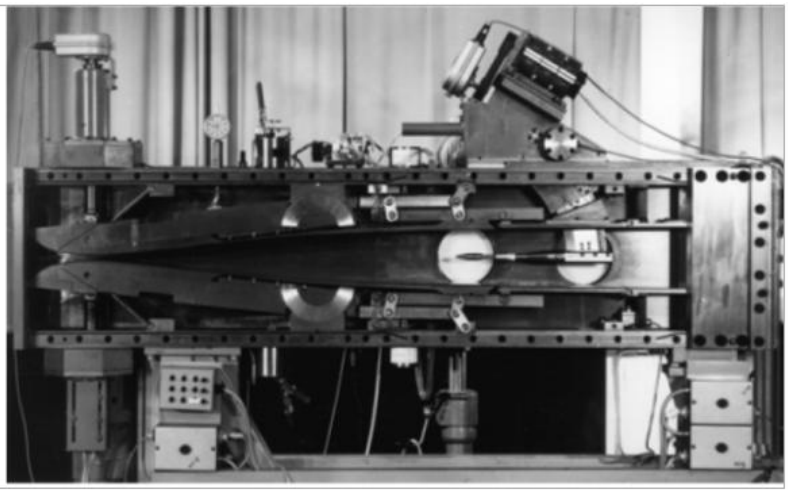

Figure 3.5: Image of the TVM150 test section and most important properties [33].

3.2.3 Setup of streak camera

The high-speed visualizations of the discharge are performed with a *C2830 Hamamatsu Streak Unit*, with a *C4742-95 camera for C2830 Hamamatsu* CCD attached. The used objective lens of the camera is a *Nikon F-mount*, with 20 mm focal length and an focal ratio of D=1.1. It is supported by an extension tube of 20 mm and an adapter to the C-mount connection of the camera. The trigger used to start the capturing is a *DG-535* delay-/pulse-generator from *Stanford Research*. The generator is connected to a Tectronix DTS 2004B oscilloscope that simultaneously measures the voltage and charge signal of the plasma actuator. The high-voltage probes that is used for this purpose is a *TestTec HVP-15HF*, the low-voltage probe for the charge signal is a *Tectronix P2220*. The pulse generator sends two trigger signals with a short delay time. The first pulse opens gate in the slow-speed sweep-unit (SSSU). The second pulse is split into two identical signals. One activates the SSSU and the other the camera to capture a streak-image of the plasma actuator.

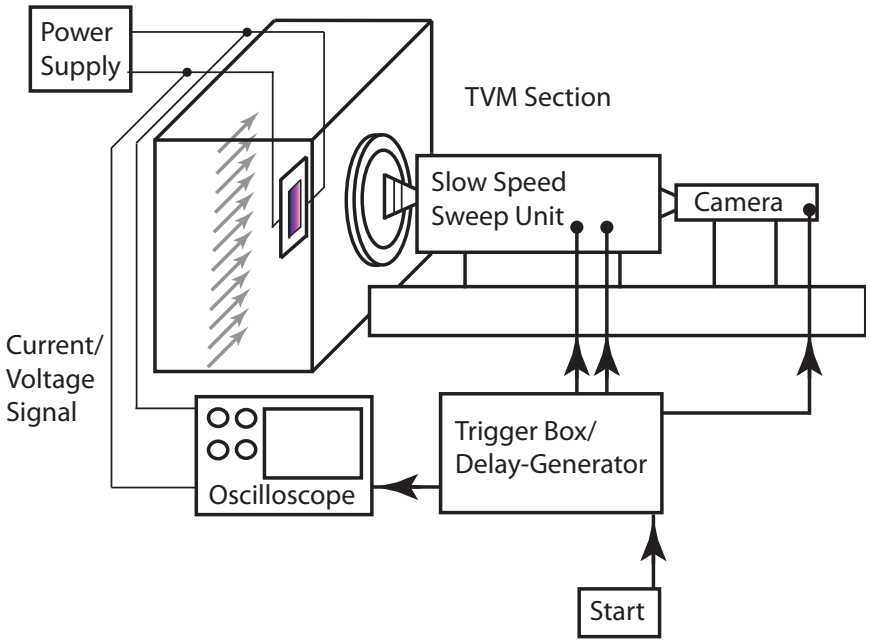

Figure 3.6: Experimental setup for the capturing of high-speed streak camera images of the discharge. The camera is mounted onto the TVM150 wall, and has an optical access to the Kapton actuator through a small window.

Simultaneously, the other triggers the oscilloscope to record the voltage and charge signal of the plasma actuator within a time interval. A streak camera consists out of a conventional camera and

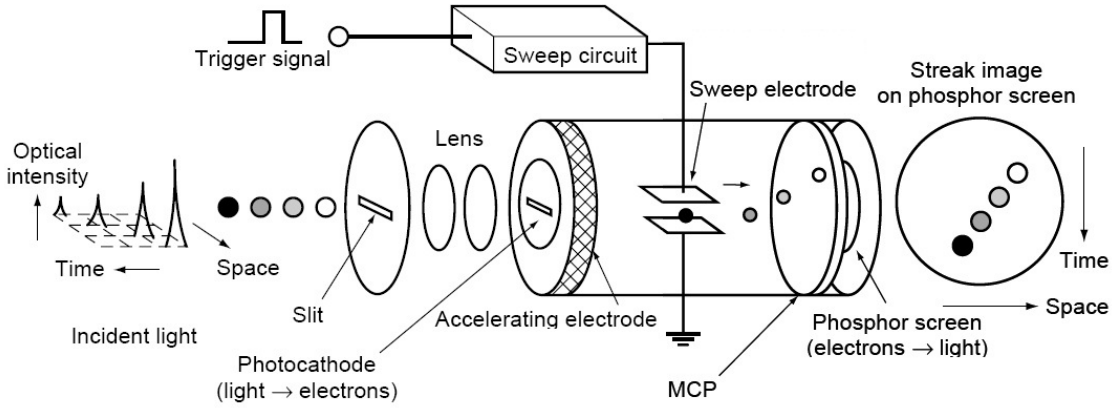

Figure 3.7: Schematic diagram of a conventional streak camera. An incident optical signal is transformed into a signal of electrons. The electrons are swept from top to bottom dependent on their time of arrival. Afterwards the signal strength is intensified with the help of a micro-channel plate. A phosphor screen transforms the electron signal back to a light signal that is recorded by an camera.

a SSSU. An incident light pulse first passes through a slit in the SSSU, extracting a one-dimensional time-dependent line out of the two-dimensional image. The photons of the light pulse knock out electrons from a photocathode. These electrons are accelerated and multiplied in an electric field

of a MCP inside of the SSSU. After the accelerating field is a second high-voltage electric field, orthogonal to both, the flight direction and to the slit-like transversal electron distribution. The field strength is increased by time, thus the electrons are deflected depending on their time of arrival. The one dimensional line is therefore swept into a two dimensional image, where the second dimension shows the schanges of the slit illumination with time. Finally, the electrons are stopped at a (phosphor) screen, which creates a visible image. This image is captured by the conventional camera and recorded on a computer.
The streak time (duration of image recording) can be adjusted between 10 ms and 1 ns. Also, the signal amplification in the MCP can be adjusted. Since luminosity of the discharge is small and the streak- time short, the contrast of the images is close to zero. Thus the brightness gain of the images has to be raised to maximum in order to be able to see a discharge.
The actuator is driven at a frequency of 10 kHz, thus the period is 100 μs. The streak-time of the captured images is 100 μs, respectively, corresponding to one period. Due to internal effects of the camera, not the complete streak-time can be captured. Important actuator voltages that are used for the high-speed images experiments are 14, 15 and 16.5 kV, corresponding to an electrical power consumption of 380, 440 and 500 Watt per meter actuator length, respectively. The power levels of 440 and 500 W/m lead to a filamentary (instable, see chap. 2.3) discharge. They are chosen since their bright discharges lead to images with sufficient contrast for small streak times. For post-processing of the data, see [13].

3.3 Setup of experiments on pressure impact

In this section, the experimental setup of experiments on the pressure impact on plasma actuators is described. The first subsection gives an overview of the experiments and their aims. The second subsection describes the pressure chamber that was specifically built for the experiments. Throughout the third section, the software control of the plasma actuator is explained together with the post-processing.

3.3.1 Experiments and aims

The first objective of the experiments on the pressure influence on plasma actuators is to identify the influence on the power consumption-voltage characteristics. For this purpose, the characteristics are recorded for different pressure levels between 0.21 bar and ambient pressure and voltage frequencies between 6 kHz and 20 kHz. The frequency range is the maximal range *MiniPuls 2.1* can deliver.
In a second set of experiments, the plasma length is captured as a function of the voltage amplitude for different pressure levels and frequencies as well. For this purpose, images of the plasma are made. The resonance behavior under different power and pressure levels is measured during a third set of experiments.

During the experiments of the environmental impact on the discharge-instabilities, two additional pressure experiments are made. In the first one, the impact of the pressure on the onset-voltage for an instable development is studied. In the second, the impact on the average spacing between the filaments is measured.

The following list shortly lists the experiments:

- Experiments of pressure impact on plasma
    1. Power consumption-voltage characteristics
    2. Plasma length
    3. Resonance behavior
- Experiments of impact on discharge-instabilities
    1. Impact on onset voltage
    2. Impact on filament spacing

3.3.2 Pressure chamber

For the pressure experiments, a vacuum chamber was constructed fully out of acrylic glass. It is designed to resist pressures between ambient pressure and 0.2 bar. Two wires in the walls allow access for the high-voltage supply and the grounding of the probe capacitor. The vacuum chamber is connected to a *PM20432* vacuum pump by *P&M GmbH* in order to create a vacuum. A valve at the pump allows controlling the pressure precisely and with high dynamic.

3.3.3 Plasma-actuator control and post-processing

The plasma actuator setup is controlled using the *Labview* software by *National Instruments*. With the help of a DAQ analog output box, the input voltage from the bridge to the cascade of *MiniPuls 2.1* can be controlled. A PID controller in the software allows to control either the output voltage or the power consumption.
Problems arise due to the usage of alumina as dielectric barrier: Since the permittivity is very high, lots of power dissipates into heat in the barrier. The heat rises the temperature of the barrier. Since the permittivity of alumina is strongly temperature dependent, the rise in the temperature changes the properties of the actuator and leads to measurements that are not reproducible. Therefore, the software is set to control the actuator not constantly, but rather in a pulsed mode. In this mode, the actuator is turned off periodically, and only turned on for a limited time of a few seconds. Through this process, the temperature rise is negligibly small.
For measuring the plasma length, the controller keeps the power consumption constant for a limited time, long enough to capture several images. Between different power levels, the actuator is turned off as well. Images of the discharge are taken using *a Nikon D 70 Coolpix* DSLR camera and an exposure time of 1/4 s. During the post-processing, the gray-scale values of the images

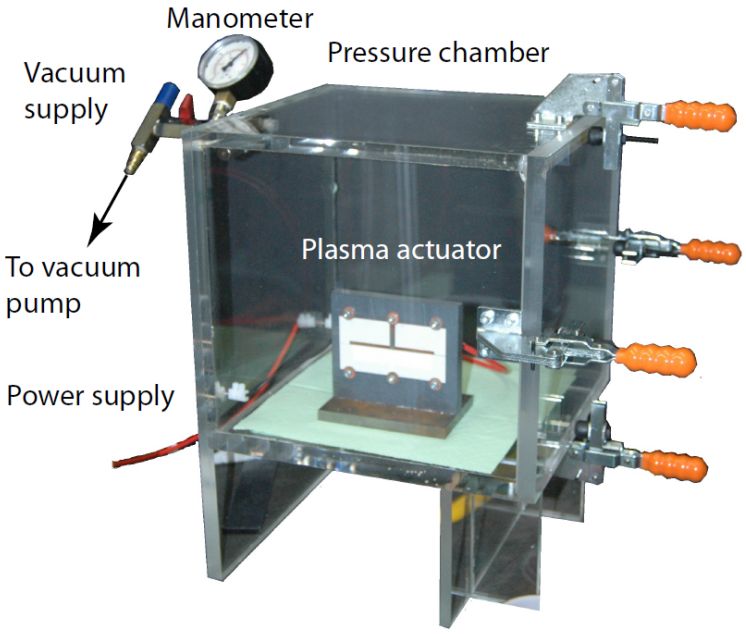

Figure 3.8: Setup of the pressure chamber. The inner size of the chamber is 20 cm x 20 cm x 20 cm and has thus a volume of 8 liter.

are averaged in spanwise direction first. Later, an algorithm searches the beginning and end of the bright plasma. The pixel size is determined from the known size of the ceramic actuator plate (10 cm x 5 cm) on the image.
For the resonance experiments, the input voltage necessary for the creation of different power levels at 10 kHz voltage frequency is measured first. Then, this voltage is kept constant and the frequency generator is set in a sweep mode, where the frequency sweeps in between 6 kHz and 20 kHz during 8 seconds. The controller used during the measurements of the instabilities and the corresponding post-processing will be explained in section 3.5.
The same controller and post-processing is used during the temperature-impact experiments that will be described during the next section.

3.4 Setup of experiments on temperature impact

In this section, the setup of the experiments on the temperature impact will be described. The first subsection gives a short overview of the experiments and the aims that are pursued with them. The second subsection describes the ovens used during the experiments. The plasma actuator control and the post-processing is the same as during the pressure experiments.

3.4.1 Experiments and aims

The aims and experiments on the temperature impact are very similar to those of the pressure impact. Two different types of ovens are used during the experiments, one baker oven for low temperatures and a furnace for high temperatures. The maximal used temperature is 600 °C. The first objective of the experiments is to identify the influence on the power consumption-voltage characteristics. For this purpose, the characteristics are recorded for different temperature between ambient temperature and 600 °C as well as voltage frequencies between 6 kHz and 20 kHz. In a second set of experiments, the plasma length is captured as a function of the voltage amplitude for different pressure levels and frequencies as well. For this purpose, images of the plasma are made, as for the pressure experiments. The resonance behavior under different power and pressure levels is measured during a third set of experiments.

During the experiments of the environmental impact on the discharge-instabilities, two additional temperature experiments are made. In the first one, the impact of the temperature on the onset-voltage for an instable development is studied. In the second, the impact on the average spacing between the filaments is measured. Experiments that require optical access are only possible in the baker oven, since the furnace allows no optical access. Therefore, the temperature of experiments on the plasma length and discharge-instabilities is limited to 250 °C.

The following list shortly lists the experiments:

- Experiments of temperature impact on plasma
    1. Power consumption-voltage characteristics
    2. Plasma length
    3. Resonance behavior
- Experiments of impact on discharge-instabilities
    1. Impact on onset-voltage
    2. Impact on filament spacing

3.4.2 Oven and furnace

For low temperatures, a *XBC805 Combi-Steam BakerTop Oven* by *UNOX* is used. This oven enables good optical access to the actuator through the front door window. The temperature range is ambient temperature to 260 °C. It is controlled by an internal controller in order to keep error in the temperature to less then ±3 °C. The second oven is a *H/K 2/3* furnace by *Heraeus GmbH*. It is able to generate chamber temperatures up to 1800 °C with a steady-state error less then ±6 °C for temperatures below 1000 °C. This furnace is used for experiments between 250 °C and 600 °C. Experiments in temperatures above 600 °C are not possible, since the copper electrodes of the

plasma actuator start to oxidize at higher temperatures. The furnace does not allow optical access since the walls are made out of mineral cotton. Opening the front door for images would instantaneously cool the actuator. Therefore, measuring the plasma length and discharge-instabilities is not possible in high temperatures. The only access to the plasma actuator is a small hole in the front door which is used for the wiring. This hole is too small for a camera. The actuator wires are isolated by ceramic pellets in order to resist the high temperatures.

(a)

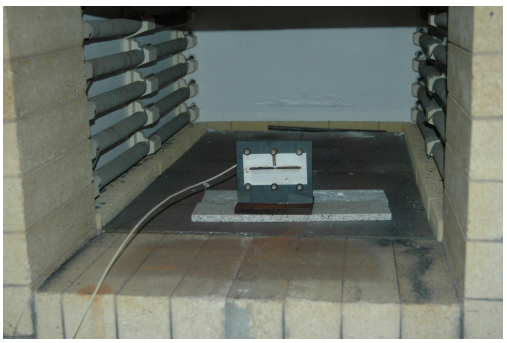

(b)

Figure 3.9: (a) *UNOX* baker oven and Nikon camera for low temperature experiments (b) plasma actuator in the *Heraeus* furnace for high temperature experiments.

3.5 Setup of experiments on instabilities

The main goal of the experiments on the discharge instabilities is to confirm the instability equation 2.20 and to measure the dependency of the filament spacing on the environmental conditions. As described in the previous sections, images of the discharge are taken for this purpose under the variation of flow velocity, pressure and temperature. The DSLR camera used for the capturing is a *Nikon P 70 Coolpix*. The exposure time is 1/4 s, since it gives the best results for various brightness levels of the discharge.

For the experiments on the onset-voltage, the output-voltage of *MiniPuls 2.1* is kept constant by a controller. Ten images are captured; afterwards the actuator is turned off to cool down. The voltage amplitude is increased in steps of 500 V. First, the size of the gray-scale value matrices of the images is reduced to the actual discharge. For this purpose, the plasma length is determined as described in subsection 3.3.3. Then, a stripe with a streamwise thickness of 50 pixel is cut out of the streamwise center of the plasma. The gray-scale values are averaged in streamwise direction in order to get a spanwise intensity profile of the discharge center. Next, the average of the profile is subtracted from it in order to have the variations only. The result is divided by the original average to make all profiles comparable in amplitude, no matter of the intensity. An exemplary result can be seen in Figure 3.10 as well as the images cut-outs. A fast Fourier transform is made of each intensity profile. In order to have a higher signal strength and a lower variation, the profiles of ten

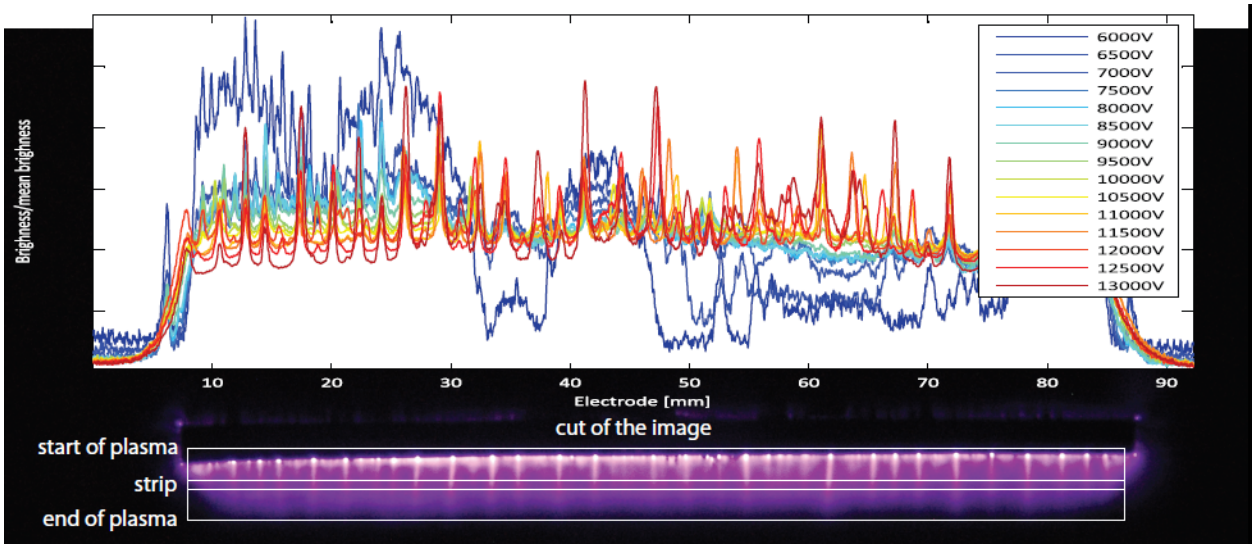

Figure 3.10: Intensity profile of the discharge center, exemplarily for ambient pressure and temperature. The voltage frequency is 10 kHz, the voltage of the discharge at the image is 11kV.

images of a voltage are combined to a single amplitude spectrum. As soon as discharge instabilities occurs, the spectrum shows not only noise but also a broad peak in between wave numbers of 0.2 mm^{-1} to 0.8 mm^{-1}. The corresponding voltage is the onset-voltage of the instable process. The wave number of the peak maximum corresponds to the average filament spacing.

During the experiments of the flow impact on the onset-voltage, this was not yet available. The onset-voltage was thus defined as when the discharge instability was visible to the unassisted eye. A look at the pressure and temperature experiments later confirmed that the results of the bare eye and the Fourier transform are in good agreement. Nevertheless, the accuracy is higher when the Fourier transform is used.

3.6 Setup of experiments on the impact of discharge-instabilities on ionic wind

The third objective of this work is to get a basic understanding of the impact of discharge-instabilities on the ionic wind. For this purpose, the velocity of the ionic wind downstream of both instabilities and the spacing in between is measured. First, the velocity is recorded with the help of a Pitot tube which is used as a Prandtl tube. Secondly, the two dimensional flow field is measured using particle image velocimetry (PIV). During both cases, a Kapton actuator is used. The voltage amplitude is 14.5 kV, the frequency 10 kHz.

Pitot tube:

A Pitot tube determines the velocity by comparing the total to the static pressure. The pressure is measured by a *Setra Static Pressure Probe, Model 267*. The Pitot tube is made out of a

glass to ensure electric insulation from the plasma discharge and has an inner diameter of 2 mm. The tube and the probe are connected with a 0.5 m rubber pipe. The Setra probe can measure pressures differences up to 250 Pa. The velocity is determined by measuring the total pressure p_t of the flow with the tube and the static pressure p_s with a pressure probe far off the flow. For subsonic flows, the stagnation pressure is

$$p_t = p_s + \left(\frac{\rho u^2}{2}\right) \tag{3.3}$$

The flow velocity thus corresponds to

$$u = \sqrt{\frac{2(p_t - p_s)}{\rho}} \tag{3.4}$$

The stagnation pressure of the ionic wind is measured downstream of the discharge area in x-direction, both behind large-scale filaments and in areas without the filaments. The measurement is repeated for different streamwise positions in order to find the maximum flow velocity of both areas, which is the main parameter of interest.

Particle image velocimetry

Particle image velocimetry (PIV) is a non-intrusive indirect velocity measurement. Tracer particles, the so called seeding, are brought into the flow. An example of seeding particles is droplets of *DEHS* fluid. Since the particles are very small, they have no impact on the flow, but follow it. A plane (Laser sheet) within the flow is illuminated twice with the help of a laser, with a small time difference Δt in between. It is assumed that the tracer particles move with local flow velocity between the two illuminations and do not leave the plane. The light scattered by the tracer particles during both illuminations is captured by a double-frame digital camera. Within *interrogation areas*, small sections of the image, the local displacement $\vec{\Delta s}$ is calculated by cross-correlation of the images. Then, the local velocity is

$$\vec{v} = \frac{\vec{\Delta s}}{\Delta t} \tag{3.5}$$

It is assumed, that all particles within one interrogation area have the same velocity. The flow velocity can be averaged over multiple velocity measurements. The main advantage of the technique is, that no instrumentation, such as pipes or wires, is necessary within the flow. Also, the complete flow field can be measured directly. The Laser used during the experiments is a *LDY 300* 2x 20 mJ, 1 kHz Nd:YLF Laser by *Litron Lasers*, the camera a *Phantom V12* by *VISION Research*, with 6.242 frames per second and resolution of 1280 x 800.
The flow field is measured both behind a filament and behind the spacing between the filaments. Figure 3.11 shows the setup of the experiment. The flow was turned off during the measurement to operate the actuator in quiescent air.

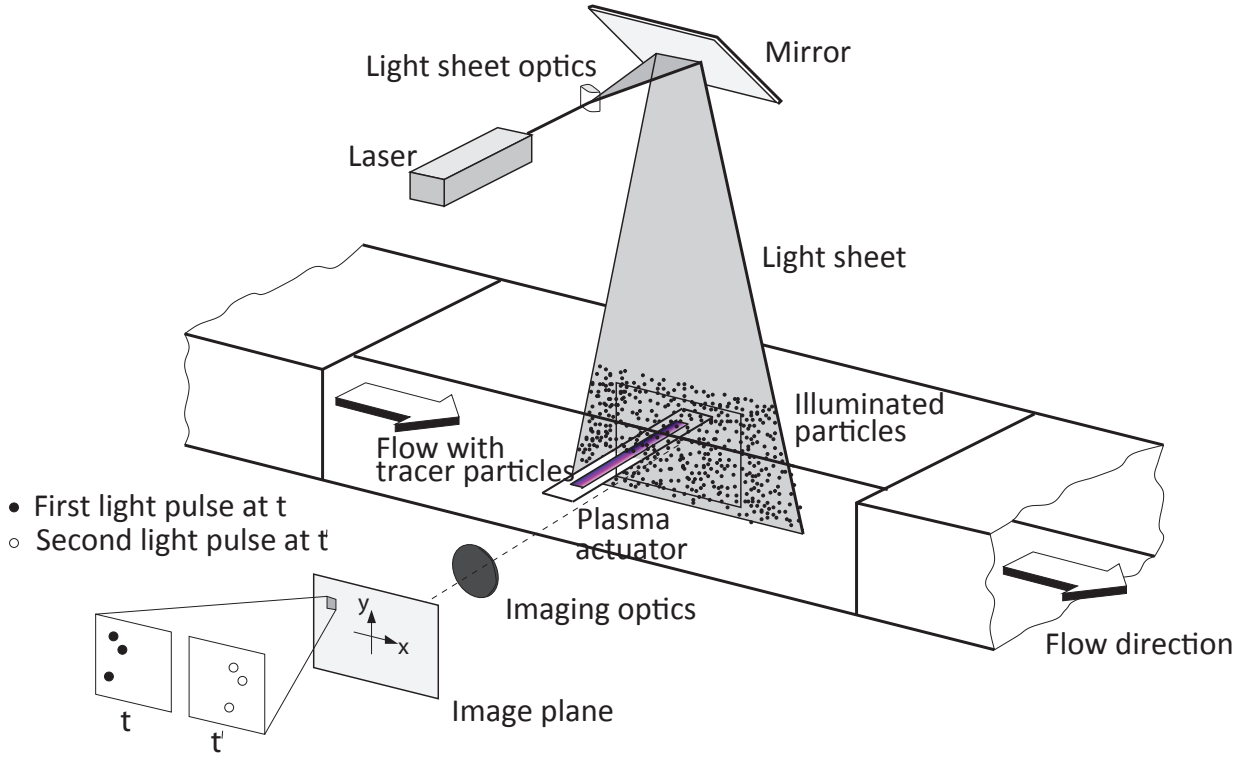

Figure 3.11: Experimental arrangement for particle image velocimetry in a wind tunnel (according to Raffel [34]).

4 Results and discussion of the experiments

Throughout this chapter, the results of the experiments on the environmental impact on plasma actuators are described and discussed, with the focus on the influence of flow velocity, pressure and temperature. The first section describes the impact of the flow velocity on the power consumption, resonance behavior and the visual appearance of the discharge. Throughout the second and third section, the impact of pressure and temperature on power consumption, plasma length and the resonance behavior are explained. The impact of environmental conditions on the voltage of the filament onset and filament spacing of discharge instabilities is described in the fourth section. The last section shows the results of experiments on the influence of discharge-instabilities on the ionic-wind velocity.

4.1 Impact of flow velocity

The impact of an external flow on the plasma actuator will be described in the following. First, the impact on the power consumption is studied for small flow velocities. In the second subsection, the influence of high Mach numbers on the resonance behavior is studied. With the results of this subsection, the experiment of Barckmann *et al.* [10] is repeated more carefully and explained in the third subsection. At last, the impact of flows with high Mach number on the discharge itself is studied using images of a streak camera.

4.1.1 Impact on power consumption

The impact of the flow velocity on the power consumption/ voltage-characteristics is studied for small flow velocities with the setup described in section 3.2. A Kapton actuator is exposed to an air flow between 0 m/s and 21 m/s. As can be seen in Figure 4.1, the minimal voltage amplitude that could be provide by the *MiniPuls 2.0* is roughly 6.5 kV. For higher amplitudes, the power consumption is strictly increasing with voltage amplitude. The measurement variance is higher at high voltages than at low ones. Nevertheless, the relative variance of roughly 7% is mainly constant.
In the linear representation of the measurement, no significant differences between the different flow velocities are evident. Small flow velocities seem to have a slightly greater slope around 13 kV, but this effect is not significant as it almost vanishes in the signal noise. Figure 4.2 shows the same measurement in a logarithmic representation. Again, no significant difference between the different flow velocities is evident. The exponent η in the power law $P_A \propto V^{\eta}$ is equal to 3.4 ± 0.1 for all flow velocities and therefore in good agreement wit the 7/2 proposed by Kriegseis [12]. At voltage amplitudes above 13 kV, the characteristics show minor variations from the power-law

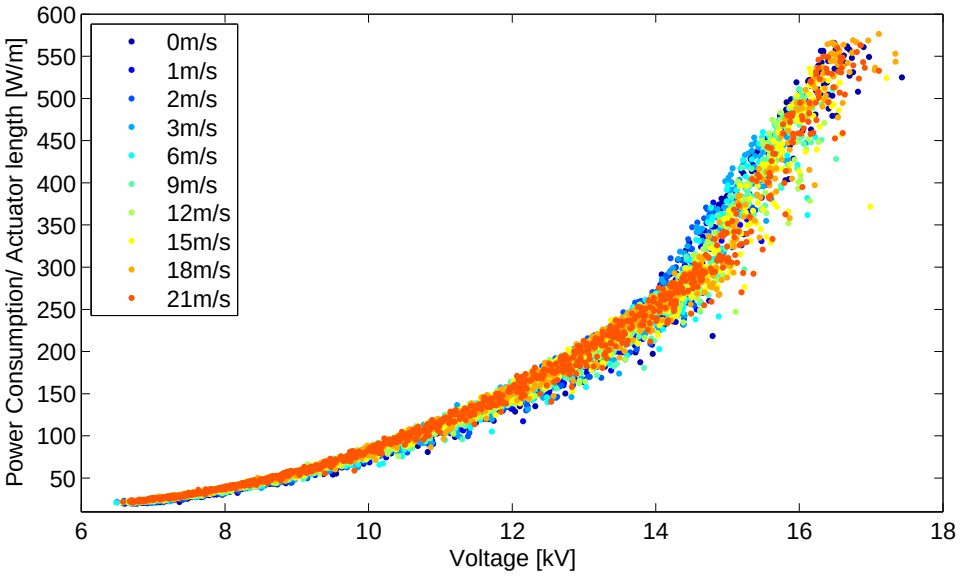

Figure 4.1: Power consumption – voltage characteristics for different low-speed flows in a linear plot. Each marker corresponds to a single power consumption measurement.

dependence in the logarithmic representation. This is probably due to heating of the actuator and thus a change in the actuator geometry and not to different flow velocities. As can be seen in the Figure, the power consumption of the actuator exposed to high flow velocities is slightly higher than during an exposure to small velocities. This means that the Θ value of the discharge in a high velocity flow could exceed that of a low velocity flow. During the next subsection it will be shown that this is not a significant effect but rather due to variances in the measuring process.

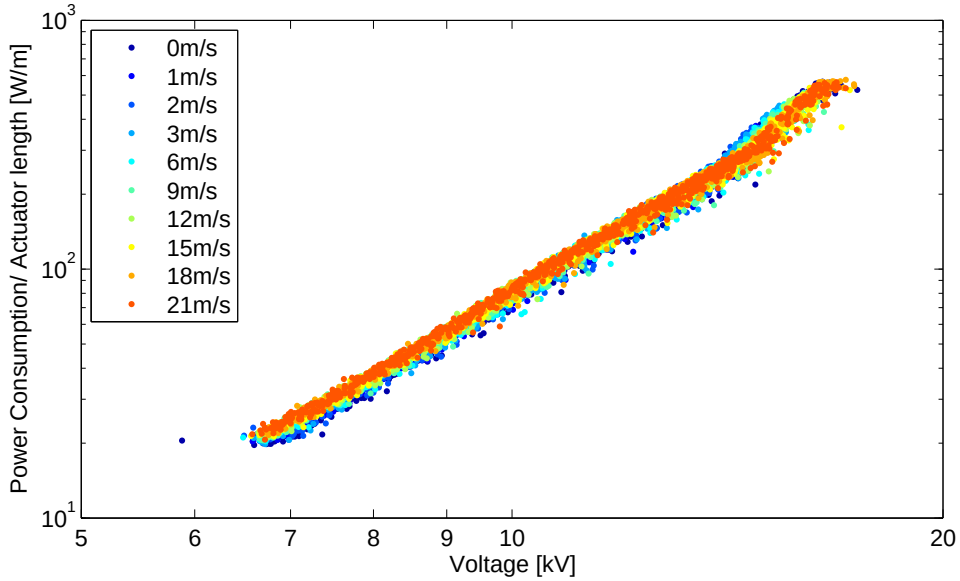

Figure 4.2: Power consumption – voltage characteristics for different low-speed flows in a logarithmic plot. Each marker corresponds to a single power consumption measurement.

4.1.2 Impact on resonance behavior

As shown in the previous subsection, the influence of the flow on the power consumption is negligible for small velocities. Therefore, the impact of a high velocity flow is studied experimentally. A Kapton actuator is inserted into the TVM150. The Mach number of the air flow is set to the highest subsonic level of Ma = 0.7. The resonance curve is measured for the actuator in quiescent air and in the gas flow. The static pressure in the flow increases slightly from ambient pressure to p_{stat} = 1.11 bar. The input voltage was chosen to generate a power consumption of 35 W at resonance frequency of 12.5 kHz, equal to a consumption per unit actuator length of 440 W/m. As can be

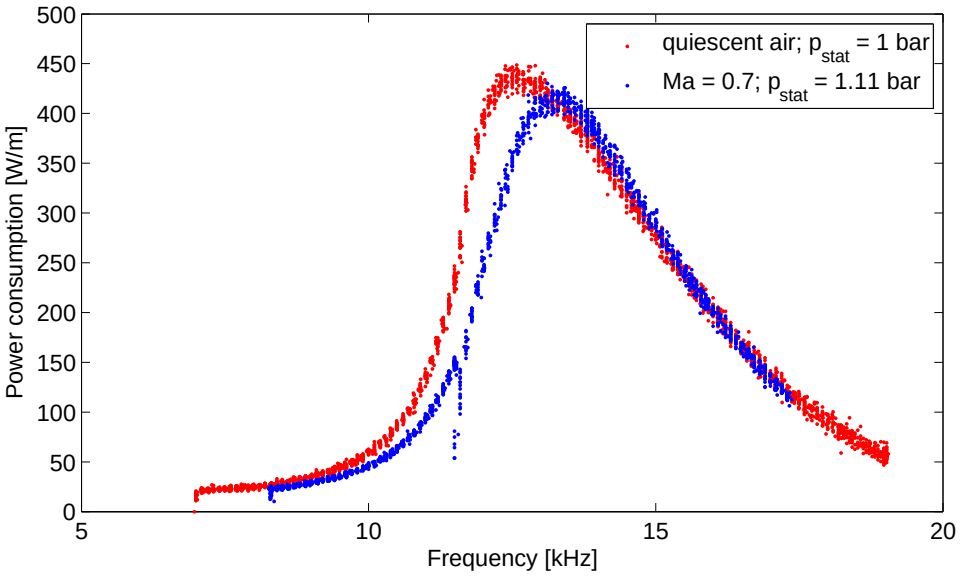

Figure 4.3: Resonance curve of a Kapton actuator in quiescent air and a subsonic flow of Ma = 0.7, p_{stat} = 1.11 bar.

seen in Figure 4.3, the resonance frequency of the actuator in the flow shifts to a higher frequency of roughly 13.2 kHz. Additionally, the maximum power consumption drops slightly to 33 W and 412 W/m, respectively. This effect is due to an increase of the impedance, caused by a decreasing capacitance of the plasma actuator. The flow reduces the number of ions in the discharge as well as the discharge volume. Thus, the active capacitance is decreasing. A system that is initially aligned with the resonance frequency will be detuned due to the impact of high-velocity flows. For example, the power consumption of the plasma actuator would drop from 375 W/m to 250 W/m when it is driven at a voltage frequency of 12 kHz and exposed to the flow, even though the input voltage remains constant. This is a reduction of 33 %. Therefore, despite the improvement in the efficiency, the resonance frequency should not be chosen as voltage frequency, since it is too sensitive to resonance shifts. It is more insightful to choose a frequency at the back of the resonance curve, since this section is less sensitive to resonance shifts due to an environmental impact. This effect was not taken into account during previous experiments. In fact, the resonance frequency was often chosen to be the voltage frequency, since it delivers the highest voltage amplitudes. The effect of such an error is shown during the next subsection.

4.1.3 Power consumption/ voltage-characteristic and resonance effects

In 2010, Barckmann *et al.* [10] made an insightful experiment: A Kapton actuator (geometry described in [10]) was exposed to a flow in streamwise direction with a Mach number of 0.42 and a pressure of p_{stat}=1.16. The resonance frequency of 8 kHz was chosen as the voltage frequency. Barckmann *et al.* compared the power consumption in the flow to that of the actuator in quiescent air under ambient pressure. The input voltage was constant during both experiments. The power consumption was 18.15 W in quiescent air and 12.21 W in the flow. Therefore, the power consumption was reduced by roughly 33%. Barckmann *et al.* assumed the reduction of the power consumption due to the slightly increased pressure to be less than 3%. Therefore, the reduction due to the flow was roughly 30%. Simultaneously, the voltage amplitude dropped from 13.5 kV to 12.9 kV. The authors assumed the influence of this effect to be negligible and the complete reduction in power consumption to be due to the flow. As shown during the previous subsection, this is not necessarily the case. The flow can easily change the location of resonance frequency and curve. When the chosen frequency is close to the cliff in the resonance curve, a shift in the resonance curve due to the flow can cause significant drops in the power consumption.

Therefore, the experiment of Barckmann *et al.* is repeated. First, the influence of the flow is identified by keeping the voltage amplitude constantly at 13.5 kV with the help of a voltage controller. In a second experiment, the influence of the resonance shift is identified by fixing the voltage at 12.9 kV and measuring the consumption drop. The pressure, flow Mach number, voltage frequency and actuator are the same as in the experiment of Barckmann. Figure 4.4 shows the development of the Mach number, static pressure and temperature in the test section of the TVM150 during the two experiments. The influence of the slightly changed temperature is assumed to be negligible as results of experiments presented later in section 4.3 show.

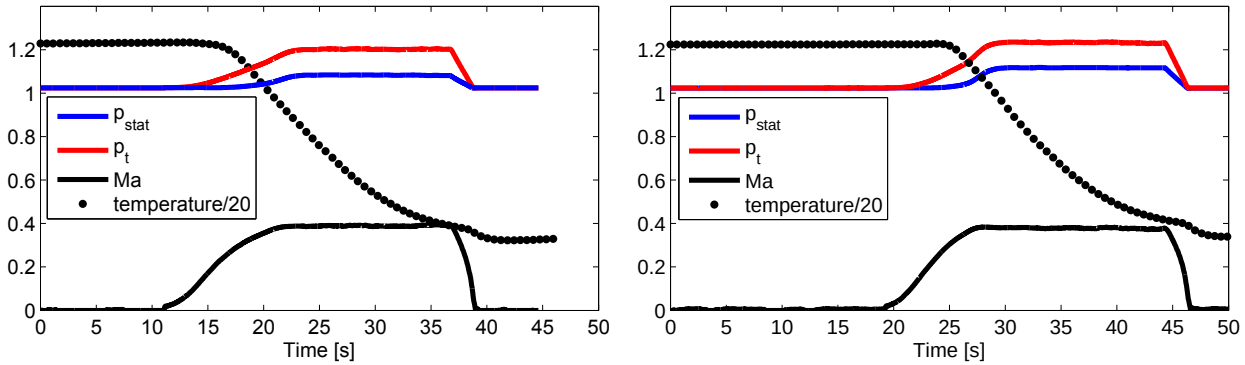

Figure 4.4: Development of Mach number, static pressure and temperature in the test section of the TVM150 during the two flow experiments regarding the flow impact. (a) Experiment on influence of the flow (b) Experiment on influence of the resonance shift.

During the first experiment, the power consumption decreases from 13.2 W (110 W/m) to 11.1 W (92.5 W/m). Therefore, the reduction is about 16%. Considering that the high voltage was kept

constantly at 13.5 kV this time, it is thus evident that the direct influence of the flow leads to a reduction of roughly 16%. During the second experiment, the power consumption reduces from 10.6 W (88.3 W/m) to 9 W (75 W/m) whilst the voltage amplitude is kept constantly at 12.9 kV. This is equivalent to a reduction by another 15%. Thus, the reduction due to the direct impact of the flow was only half of the origin of the drop observed by Barckmann *et al.*. The other half of the drop is due a shift of the resonance frequency that causes the voltage amplitude to decrease to 12.9 kHz. The lower voltage subsequently reduces the power consumption as well. Combining both effects, the overall reduction is 31% and thus in good agreement with the results of Barckmann *et al.*.

The experiment proves that the power consumption is smaller in high velocity flows than in quiescent air for constant voltage amplitude. Therefore, the minor increase of the power consumption with the flow velocity that was observed during the experiments in section 4.1.1 is most likely due to measurement variances, since the experiments of this section showed, that high velocity flows decrease the power consumption. Θ is thus decreasing with higher flow velocities. The precise dependence should be investigated in future experiments. Also, that research should take the impact of the increasing impedance into account. Thus, the voltage amplitude should be controlled.

4.1.4 Impact on discharge behavior

Within [13], Bürkle captured high-speed images of the discharge in a Kapton actuator using a streak camera. With this images the dominant discharge regimes during the different half-cycles of a discharge could be identified.

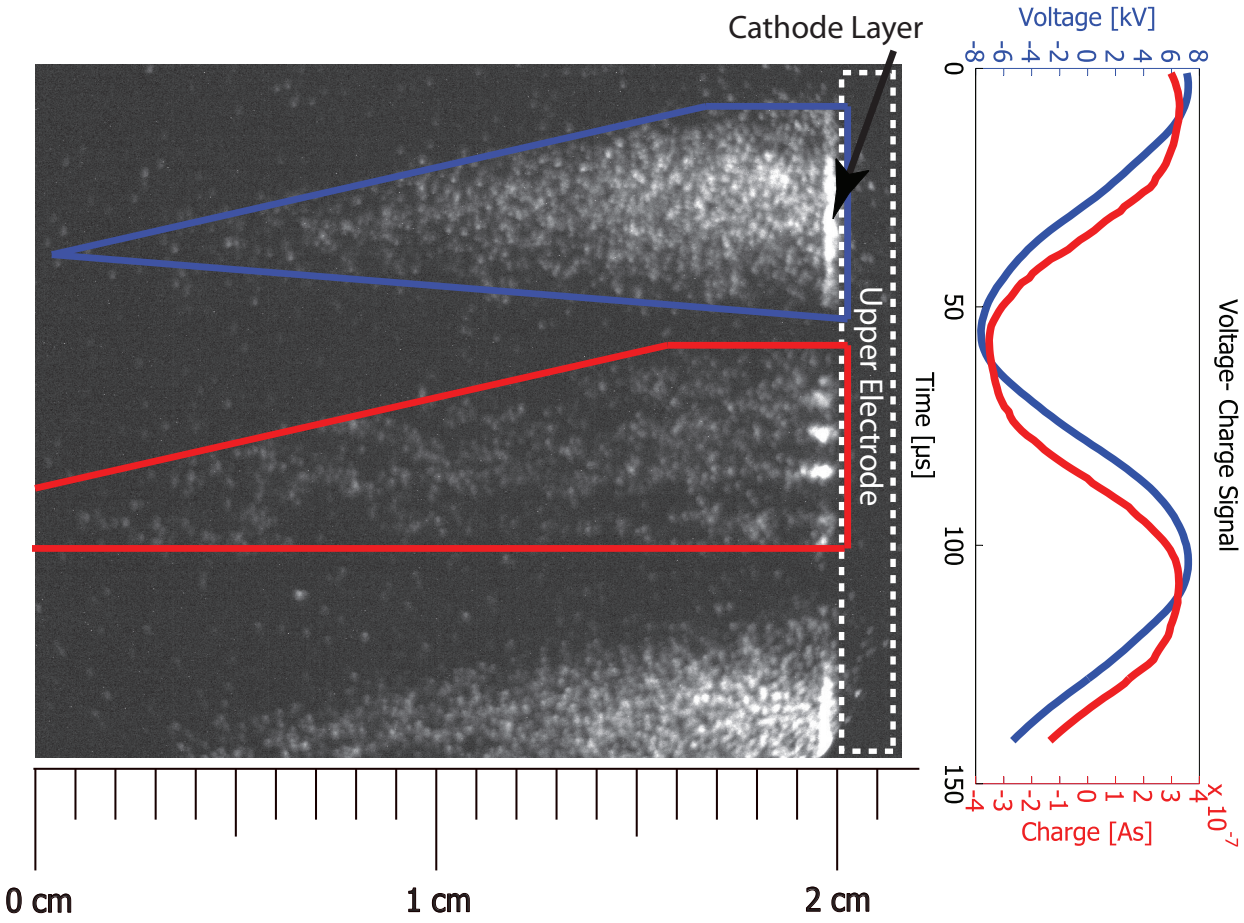

Figure 4.5: Streak camera image of the discharge, slot streamwise. The frequency was 10 kHz, the power consumption 440 W/m. The streak-time is 200 μs. The polygons indicate the ranges of the area of discharges for positive (red) and negative (blue) half-cycle [13].

The main results were:

- The discharge during the negative half-cycle is made out of a homogeneous glow with a cathode layer close to the upper electrode. The number and repetition rate of the discharges is such that the discharge appears as one continuous glow rather than single pulses. The discharge starts as soon as the drop in the voltage amplitude is sufiicciently high. The bright region close to the upper electrode in Figure 4.5 can be identified as a cathode layer according to the prediction of Soloview *et al.* [20]. The discharge starts with a minimal streamwise length close to the upper electrode. As the voltage decreases, the discharge grows linearly into streamwise direction.

- During the positive half-cycle, the discharge consists of a few single discharges of high luminosity, visible with the "dotted" region in Figure 4.5. These are presumably streamers. The discharge starts as soon as the voltage ramp is sufficiently high. The streamers begin to grow streamwise from the upper electrode towards the end of the lower electrode. When the growth starts, they have a minimal length. As the theory of streamers predicts, the discharge shows no hint of a cathode layer.
- During the extreme of the sinusoidal voltage amplitude, no discharges appear. This "dark periode" is dominant for lower voltage amplitudes and asymptotically reduces to 25% of the cycle time for higher voltages.
- Discharge-instabilities, as described in section 2.3, appear only during the negative half-cycle for the chosen setup. The origin of this effect is not clarified yet.

It is insightful to investigate the impact of the environmental conditions, particularly the flow velocity, on the discharge behavior of such a plasma actuator. Therefore, the streak camera is mounted onto the TVM150 as described in subsection 3.2.3. The Kapton actuator is attached to a lance in the flow in a co-flow configuration. The discharge is visible through a window in the test section sid walls.
During the experiments, the velocity of the flow within the discharge is either Ma = 0.42, 0.53, 0.62 or 0.7, respectively. In a first set of experiments, the flow velocity is varied between Ma = 0.42 and Ma = 0.7, while the power consumption and the voltage frequency are kept constant. In a second set, the impact of different power consumption levels is studied for different flow velocities whilst keeping the frequency constant. During a third set of experiments, the impact of different voltage frequencies on the discharge is investigated whilst keeping the power consumption constant and using different flow Mach numbers. The static pressure is roughly ambient pressure during all experiments. Figure 4.6 gives an overview of the varied parameter.

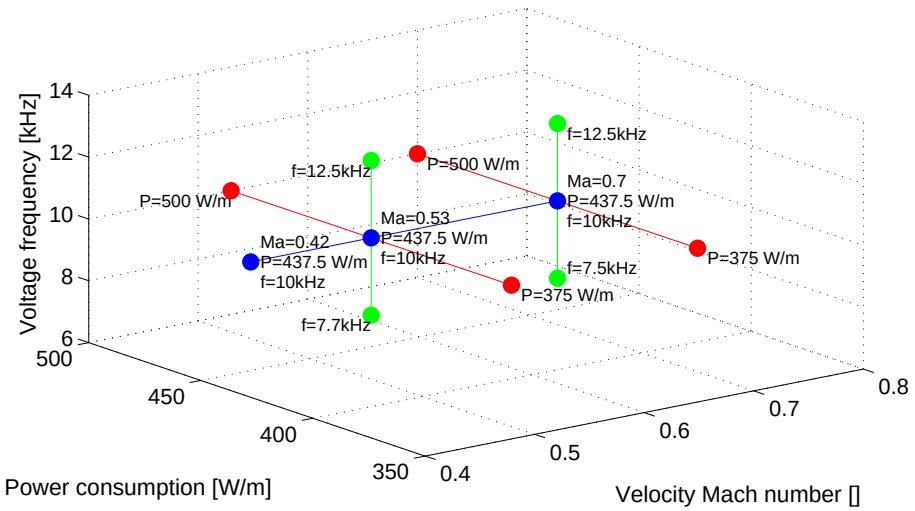

Figure 4.6: Overview of the TVM150 experiments: Flow impact (blue), combined flow and power consumption impact (red), combined flow and frequency impact (green).

Flow impact:

Figure 4.7 shows the discharge of the Kapton actuator without flow. The power consumption is 35 W (437 W/m) with an aplied voltage of 13.7 kV at a frequency of 10 kHz. The image is the reference of all images of experiments with a 35 W discharge. Identical to the results shown by Bürkle in [13], the discharge occurs only at increasing or decreasing voltage. During the voltage extreme, the dark zone without luminous discharges is evident. Significant differences between the two half-cycles are visible. During the positive half-cycle, big, homogeneously distributed discharge spots occur, corresponding to streamers. Smaller and inhomogeneously distributed spots dominate the discharge during the negative half-cycle. These correspond to corona discharges. Filaments due to the instable discharge are only visible in the negative half-cycle.

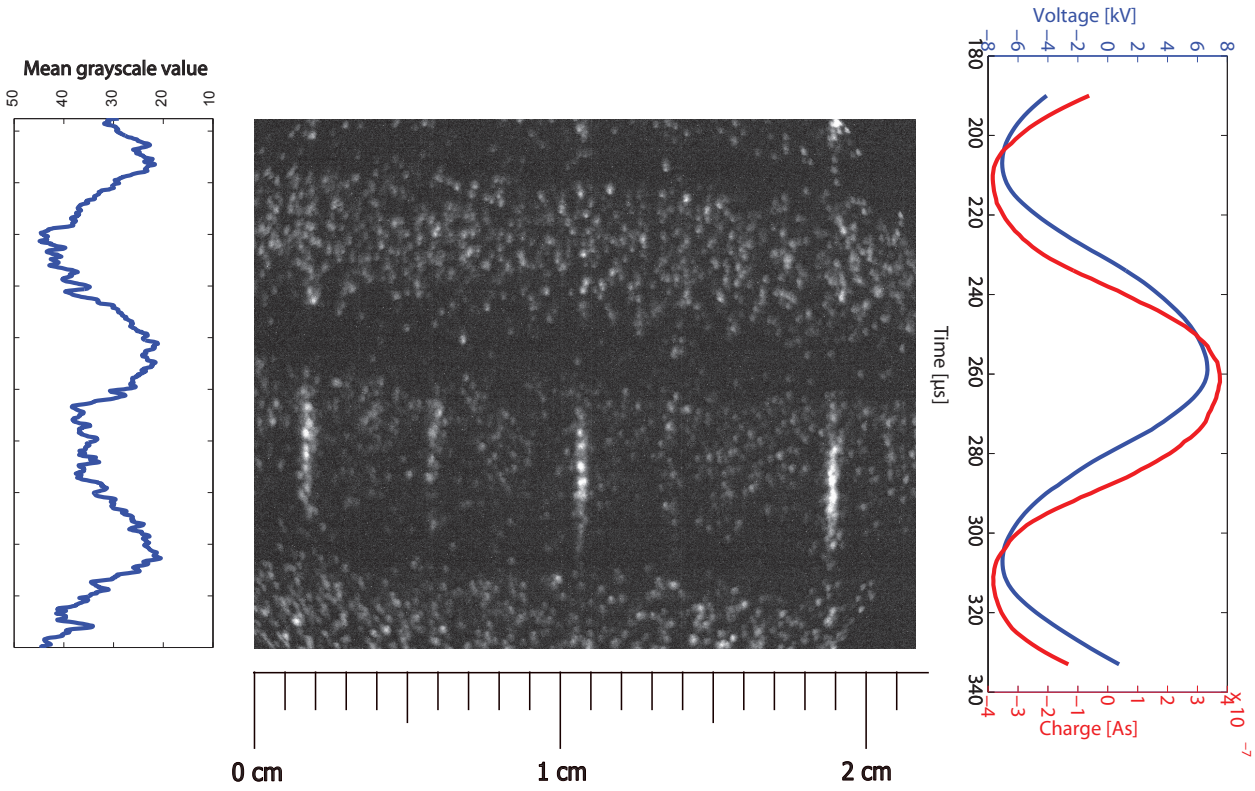

Figure 4.7: Reference streak camera image of a 35 W (437 W/m), 10 kHz discharge without flow.

Figure 4.8 shows an image of the same discharge, but exposed to a flow with Ma = 0.42. A controller keeps the power consumption constant, since the flow decreases the consumption for a constant voltage amplitude, as described during the previous subsections. Obviously, the discharge is not strongly affected by a flow of that Mach number. The discharge has roughly the same brightness and the number of discharges is constant. The dark time at minimal voltage amplitude increases slighly. Filaments only occur during the negative half-cycle, as in quiescent air. The filament spacing shows a large difference to the reference image as it significantly decreases when the plasma actuator is exposed to the flow. On the left side, the mean gray scale value in spanwise direction can be seen.

In an additional experiment, the actuator is exposed to an increased flow velocity of Ma = 0.53 flow. The discharge of that situation can be seen in Figure 4.9. The dicharges seem to concentrate

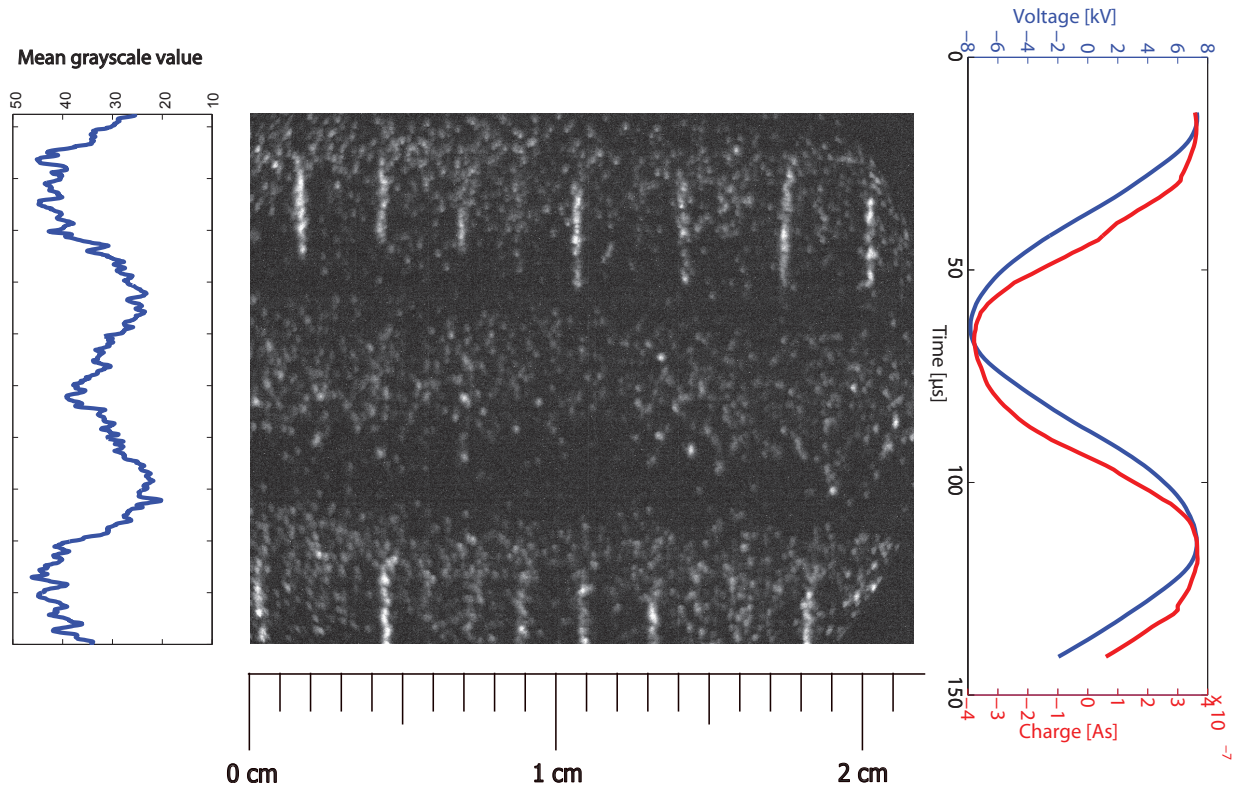

Figure 4.8: Streak image of a 437 W/m discharge in a Ma = 0.42 flow.

further, since the duration of the dark time is increasing whereas the overall number of dicharges is roughly constant. Thus, most discharges occur during the time of high voltage gradients. Additionally, their strength and thus luminosity seems do have decreased compared to the discharges in lower flow velocities. Filaments of the discharge still only occure during the negative half-cycle, no local concentration of the dicharges is evident during the positive half-cycle. Due to the flow impact, their spacing increases compared to the situation at Ma = 0.42. Also, the number of discharges within the filaments seems to decrease, since the filaments are less luminous and have a lower number of bright spots.

Figure 4.10 confirms this dependence. It shows the streak image of the discharge under the same power consumption, voltage frequency and static pressure as before, but exposed to a flow of a higher Mach number of Ma = 0.7. The dark time slightly increases further. Additionally, the number of dicharges per half-cycle and their luminosity decreases. During both half-cycles, the density of disharges is smaller. The filaments still occur during the negative half-cycle, but their spacing increases, whereas the number of discharges within one filament and their luminosity decrease further.

In summary it can be said that the flow forces the discharges to concentrate and occur mainly at times with high voltage gradient. The number of discharges is decreasing, both within and outside of filaments. Fewer filaments occur with a flow of higher Mach number. The latter effect will be discussed in subsection 4.4.1.
Pavon [17] explained the effect of the flow on the discharge with the decreasing number of ions: Due to the flow, an increasing number of ions are blown out of the discharge zone before a new

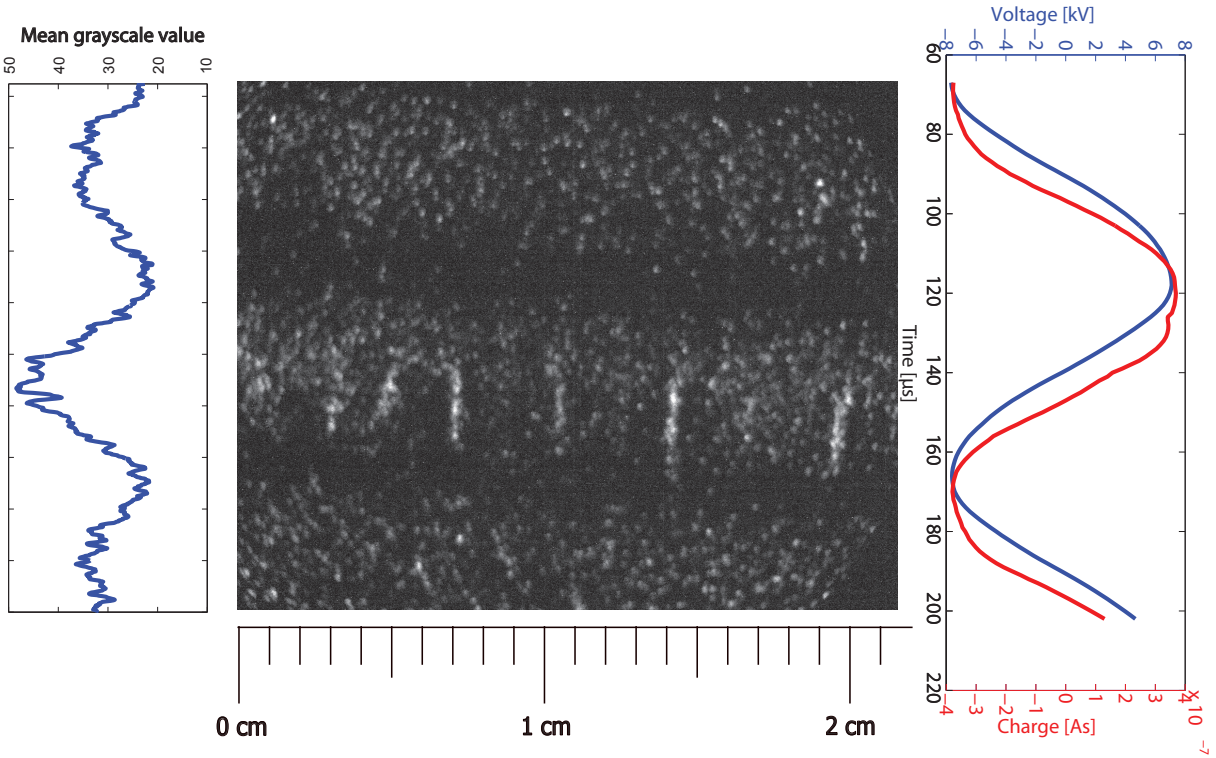

Figure 4.9: Streak image of a 437 W/m discharge in a Ma = 0.53 flow.

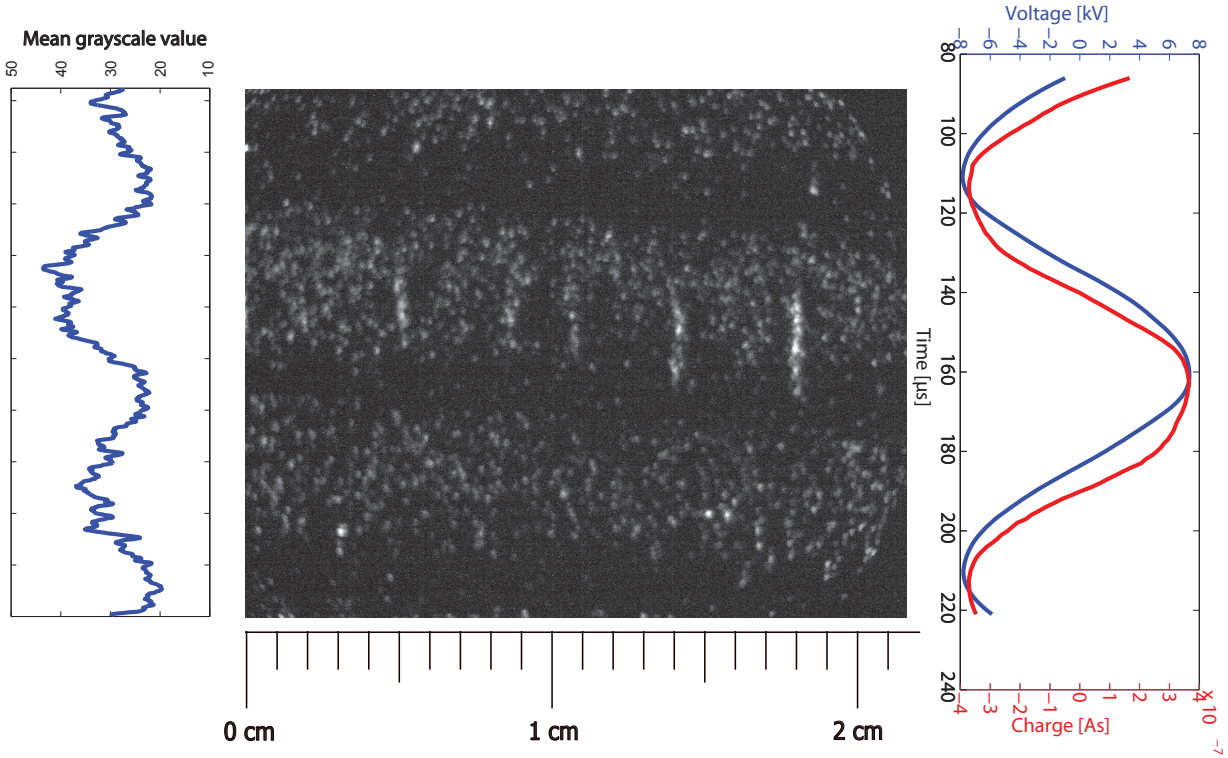

Figure 4.10: Streak image of a 437 W/m discharge in a Ma = 0.7 flow.

discharge can occur. These ions otherwisely support the discharge, such that a smaller voltage

gradient is necessary for a new breakdown. This explaines why the duration of the dark time is enhanced, since a higher voltage gradient is necassary to maintain the discharges. Thus, close to the voltage extreme, the discharges end earlier as the voltage gradient is not sufficient to maintain a further discharge. Also, fewer discharges occur, as a difference between the externally applied electric field and the field of the surface charge is necessary to create a breakdown.

Flow impact and power consumption effects:

During the experiments described in the following, the power consumption of the discharge is varied whilst exposing the actuator to a flow. The main aim is to study whether the flow has a different – stronger or weaker – effect on discharges with a low power consumption compared to those with a higher consumption. In that case, a different percentage of the power is dissipated in the passive element of the actuator. As it turns out, the luminosity of the discharge in a flow with Mach numbers Ma = 0.53 or Ma = 0.7 is too small to be captured by the streak camera when the power consumption is reduced to 30 W (375 W/m at a voltage amplitude of 13.8 kV or 13.1 kV, sespectively), even though the luminosity of the same discharge in quisecent air is sufficiently high to be captured. All images captured of the discharge in the flow are black. It is not clear weather the gas breakdown is totally prevented by the flow or if its luminosity is simply too small. Given the power of 30 W is fully dissipated in the passive actuator, as it would be if all breakdown is prevented by the flow, the voltage amplitude is strongly increasing as the power consumption of the passive element is significantly smaller than that of the discharge. As the voltage amplitude is in the same order of magnitude as for the case of an actuator operated in air, a discharge is most likely still existing but too dark to be detected in the flow by the streak camera. Thus, no conclusions can be drawn for discharges with a power consumption less than 30 W (375 W/m). Thus, the results of the experiments on a 35 W (437 W/m) discharge will be compared to ones with a higher consumption. Figure 4.11 shows the the discharge within a flow with Ma = 0.53, when the power consumption is increased to 40 W (500 W/m). Obviously, the dark time is significantly smaller than in the case of a 35 W discharge in the same flow, as shown in Figure 4.9. Also, the number of discharges is higher, especially in the negative half-cycle. The filaments are stronger and significantly larger in number.

When the flow velocity is increased to Ma = 0.7 and the power consumption kept constant, the number and luminosity of discharges is decreased and the dead time is longer, as can be seen by the gray-scale values. The corresponding steak-camera images can be seen in Figure 4.12. It seems that the flow has a stronger impact on the discharge for a high voltage consumption, as a comparison to Figures 4.9 and 4.10 reveals. This observation is suppoerted by the coltage amplitudes of the corresponding experiments. When the plasma actuator power consumption is controlled at 35 W (437 W/m), the voltage amplitude is 15 kV at Ma = 0.53 and increases to 15.4 kV at Ma = 0.7. The effect on the voltage amplitude for a 40 W (500 W/m) power consumption is significantly stronger, it increases from 15.1 kV at Ma = 0.53 to 16.2 kV at Ma = 0.7. Also, Thus, the increase of the voltage necessary to maintain a constant power consumption is significantly higher for higher power consumption levels. The number of discharges within the negative half-cycle seems to be stronger decreased than during the positive one. Thus, the flow has a stronger effect on the negative half-cycle. Also, the number and luminosity of the filaments has decreased stronger for the 500 W/m

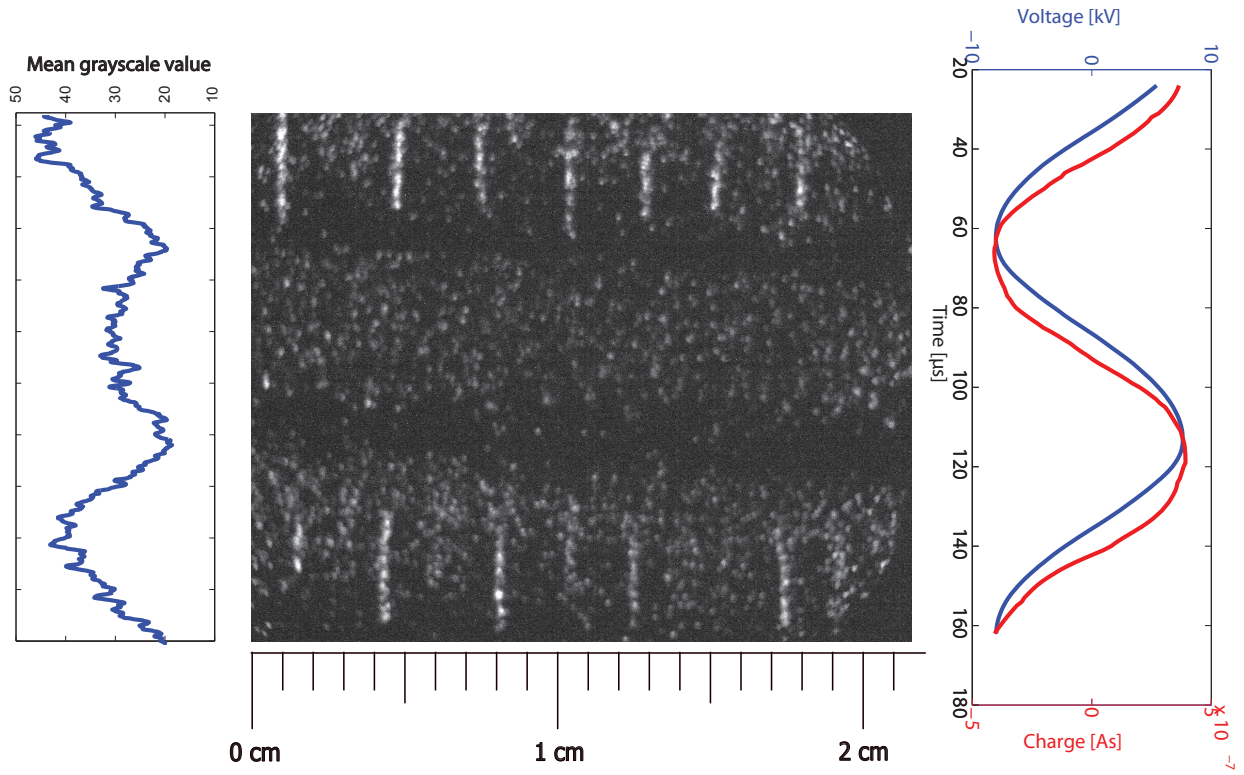

Figure 4.11: Streak image of a 500 W/m discharge in a Ma = 0.53 flow.

discharge, as they are almost invisible. The origin of the stronger impact on the negative half-cycle

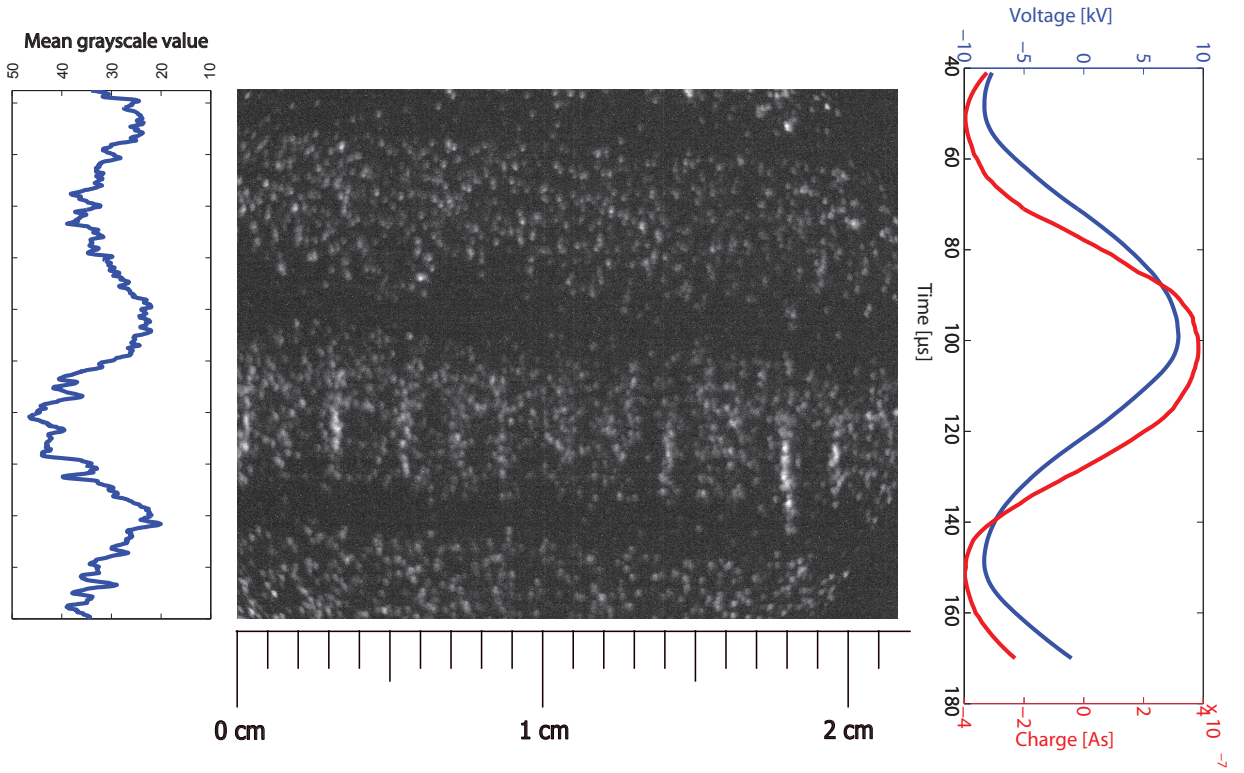

Figure 4.12: Streak image of a 500 W/m discharge in a Ma = 0.7 flow.

seems to be the different discharge regimes involved: On one hand, the negative half-cycle is domiated by the corona discharge. This discharge is strongly dependent on the positive ions within the cathode layer. When these are removed due to the flow, they can not knock out secondary electrons from the cathode surface through secondary electron emission. It is thus more difficult to maintain the discarge and it ends with a higher minimal breakdown voltage. The streamer discharge of the positive half-cycle on the other side is domiated by the photo effect. Neither the propagation of the UV radiation nore the photo effect are influenced by the flow. Thus, the impact of the flow velocity is only of minor nature, as it has only an effect on the generation of initial avalanche discharges.

The stronger imact of the flow on discharges with a high power consumption can not be explained easily. Presumably, the impact of the removal of ions has a nonlinear dependence. When most ions are removed, the removal of more ions has only a minor impact since the breakdown voltage barely depents on the number ions any more. In that case, a discharge with a low power consumption that has few ions to loose is less dependent on the flow velocity than a high power discharge with a high ion density. Future experiments are necessary to verify this theory.

Flow impact and frequency effects:

Figure 4.13 shows a 437 W/m discharge exposed to a flow with Ma = 0.53. The voltage frequency is reduced to to f = 7.5 kHz. Obviously, less voltage cycles are evident in an image of the same streak time, only one of each, positive and negative half-cycle. The dark time is longer than in a discharge with a higher frequency, as in Figure 4.9, which is no surprise as the duration of low voltage gradients is longer. Interestingly, the number of dicharges per time is roughly the same as during the experiment with a higher frequency. This is probably due to the fact that the voltage amplitude is increased to keep the power consumption constant. Thus, the voltage gradient remains roughly the same. Also, the filament spacing during the negative half-cycle is roughly the same as for the same experiment with a higher frequency.

Figure 4.13 shows the same discharge, only with a higher frequency of 12.5 kHz. In total, two voltage periods are visible. The dark time is shorter than for discharges with lower frequency, whereas the number of discharges during the discharges still remains roughly constant. This is probably due to the reverse effect of what was described above: As the voltage frequency is increased, the amplitude is decreased in order to keep the power consumption constant. Thus, even though the frequency is increased, the voltage gradient is roughly constant. Again, the frequency does not seem to have an impact on the filament spacing.

Experiments with f = 7.5 kHz and f = 12.5 kHz did not lead to sufficiant results in a flow with higher Mach number, as the lumiosity of the discharge with f = 7.5 kHz was too low to be recorded by the streak camera. The *MiniPuls 2.0* was not able to generate a 437 W/m discharge in a flow of Ma = 0.7 and a voltage of f = 12.5 kHz, as the voltage amplitude is too high. Thus, no results are gained for a flow with Ma = 0.7.

In summary it can be said that a flow forces the discharges to concentrate and occur mainly during periods of high voltage gradients, as the ions are blown away. Thus, the impact on the

negative half-cycle is stronger than on the positive one, as the streamer discharge is less sensitive to the ion concentration. The impact is higher on discharges with a higher power consumption. A reduced voltage frequency increases the duration of the dark time, whereas the number of discharges per time remains roughly constant, as the voltage amplitude is simultaniously increased. In the next subsection, the impact of pressure on a ceramic plasma actuator will be investigated.

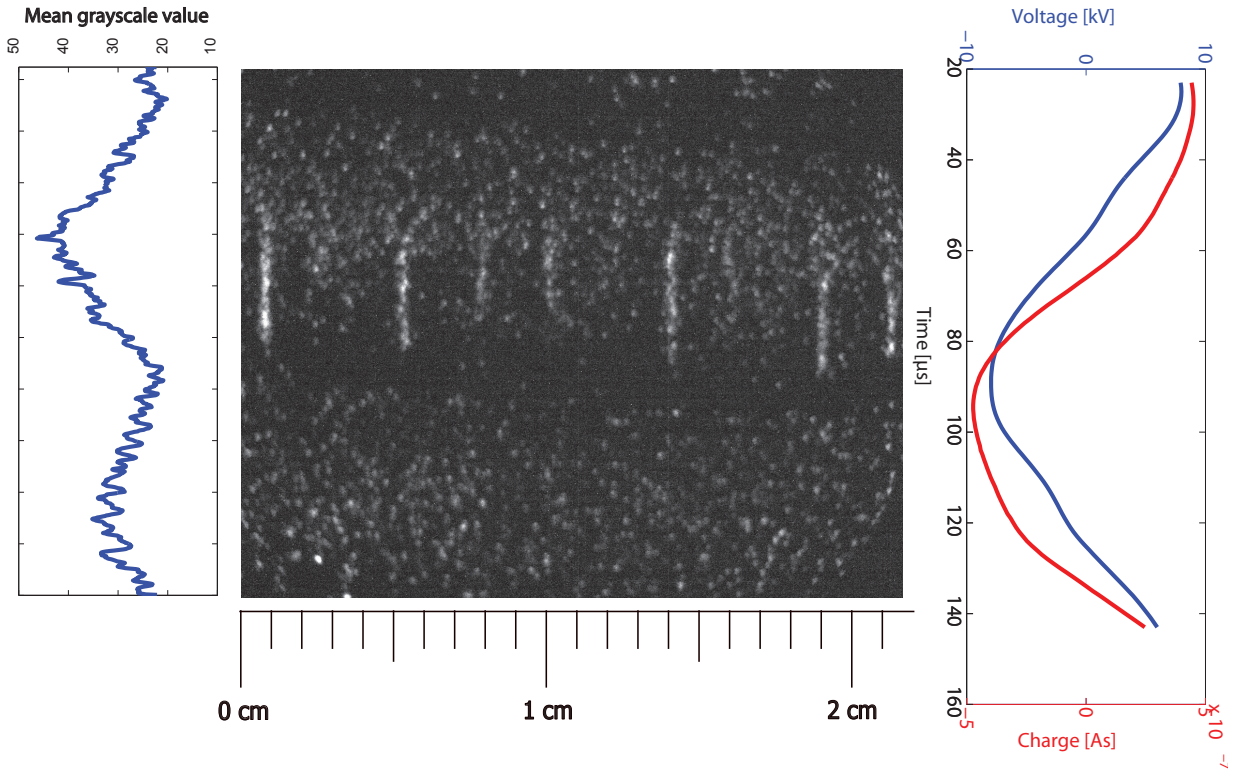

Figure 4.13: Streak image of a 437 W/m discharge in a Ma = 0.53 flow. The voltage frequency is 7.5 kHz.

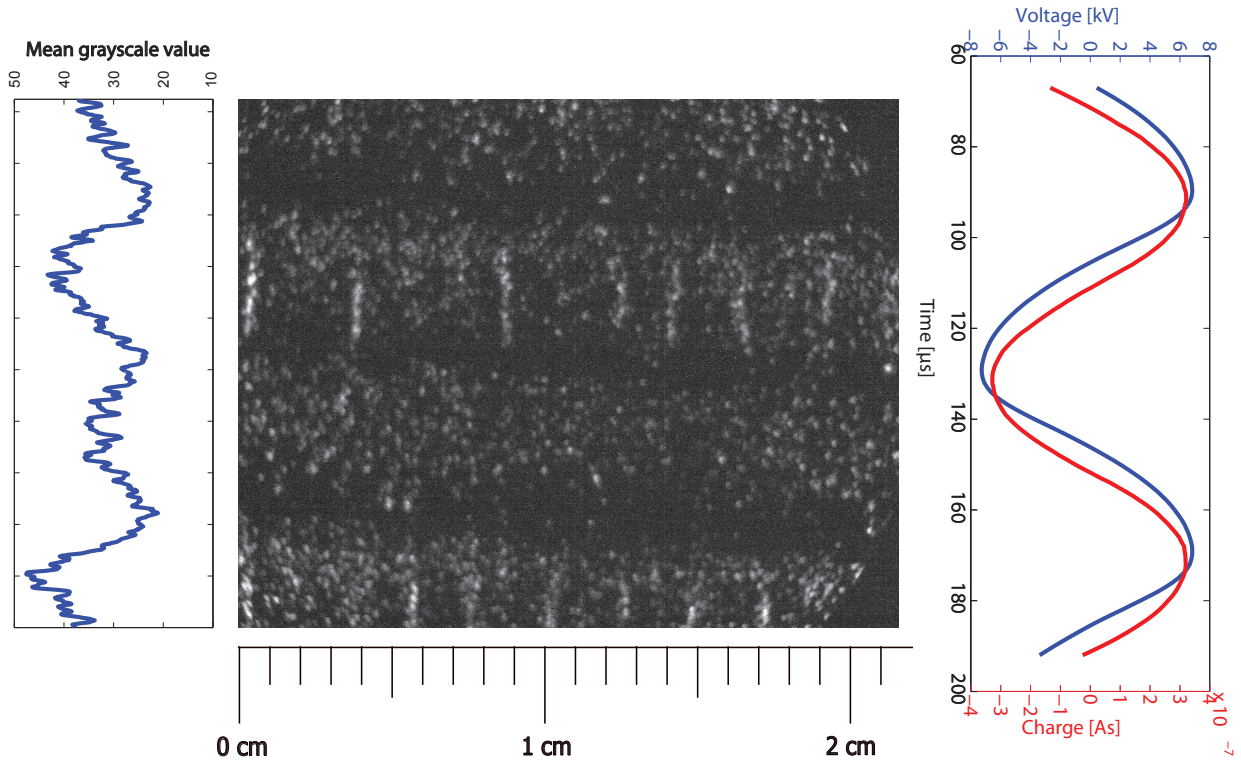

Figure 4.14: Streak image of a 437 W/m discharge in a Ma = 0.53 flow. The voltage frequency is 12.5 kHz.

4.2 Impact of pressure

As described in section 3.3.2, a vacuum chamber is built for pressure experiments. The investigations focus on the impact of the pressure at levels less than ambient pressure or equal to it. The power consumption characteristic is measured for different pressure levels and voltage frequencies. Afterwards, the impact on the resonance behavior and thus the impedance is investigated. Also, the variation of the plasma length with pressure and voltage frequency is studied.

4.2.1 Impact on power consumption

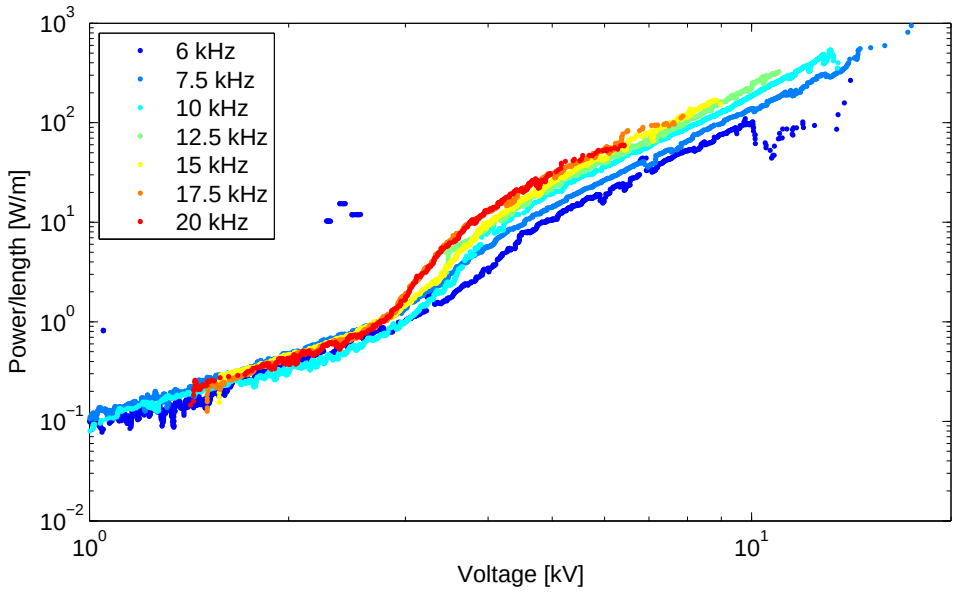

Figure 4.15: PVC of the discharge under ambient pressure and for different voltage frequencies.

Figure 4.15 shows the power consumption/ voltage-amplitude characteristics (PVC) of a ceramic actuator under ambient pressure and temperature. As can be seen, the PVC depends on the voltage frequency of the power generator. It can also be seen that the actuator is a purely passive element without a discharge for voltages less than approximately 3 kV. The PVC follows the power law of a capacitor $P_A \propto V^2$ in good agreement. Since the power consumption of a capacitor is independent of frequency, the PVC in this area is identical for all frequencies.
In between roughly 3 kV and 5 kV is a transition between a passive and an active element. First discharges begin to occur. The power consumption rises strongly during the transition. The onset voltage and consumption are frequency-independent in a first approximation. For ambient pressure, the voltage is roughly 3 kV and the consumption 1 W/m. The reason for this common onset voltage is obvious: the transition to an active element with a discharge starts as soon as the breakdown-voltage for air under ambient pressure is reached, as described by the Paschen-curve. This breakdown-voltage is frequency independent. During the transition, the parameter η in the power law $P_A \propto V^\eta$ is frequency-dependent during the transition. It ranges between 5 and 7 for

ambient pressure. Higher frequencies have higher η values. At a power consumption of approximately 10 W/m, the transition ends. Whereas the power consumption at the end of the transitions seems to be independent of the voltage frequency, the voltage is frequency dependent and ranges from 4 kV to 5 kV.
It can be seen that the power law dependence $P_A \propto V^{7/2}$ holds, when the plasma actuator is used as an active element, i.e. voltages greater than approximately 4 kV. The power consumption increases with the voltage amplitude. Further analysis of the data revealed that the dependence follows a $P_A \propto f{\cdot}V^{7/2}$ power law, as predicted by the theory.

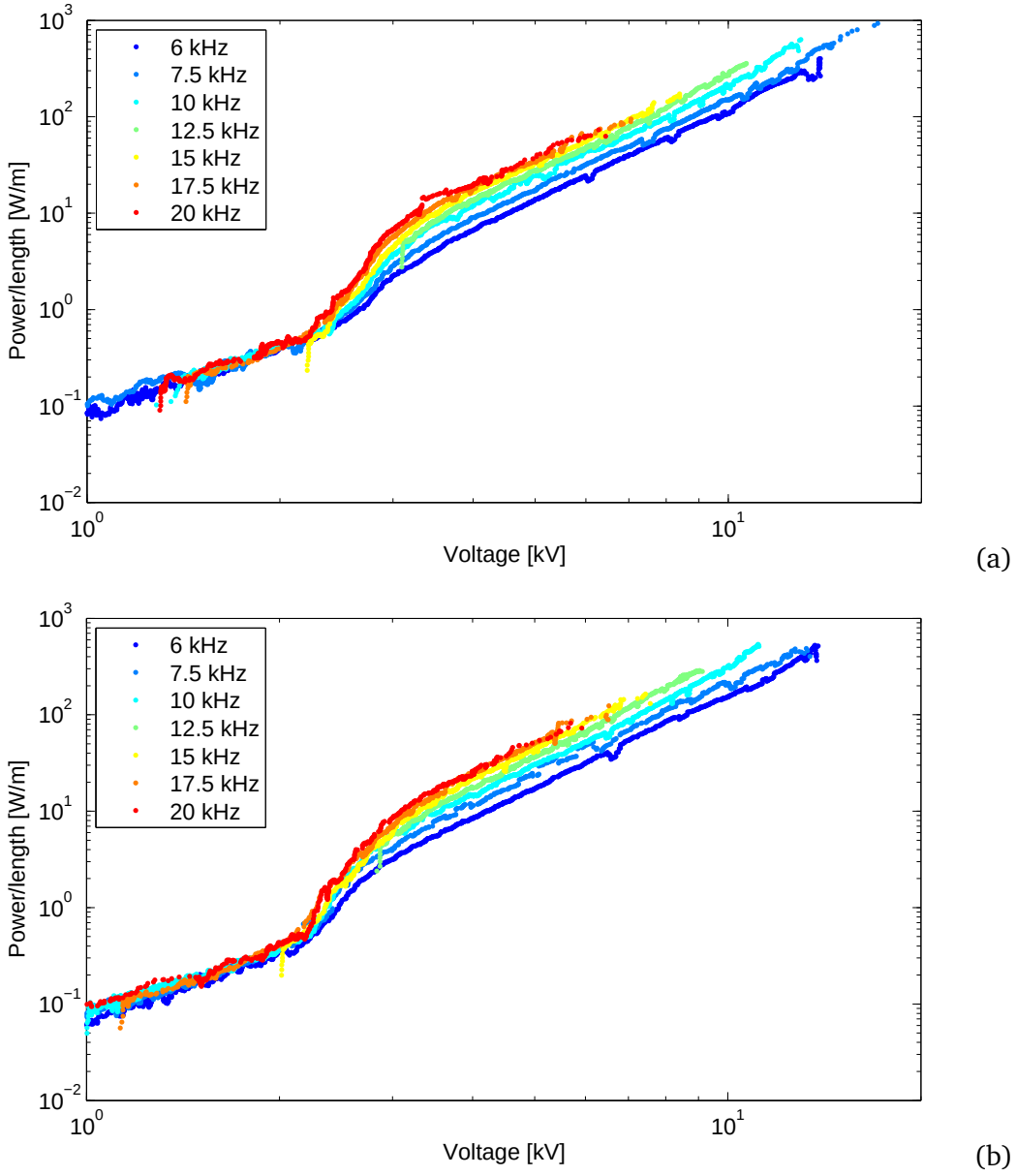

Figure 4.16: PVC of the discharge under different pressure levels and voltage amplitudes. (a) p = 0.8 bar (b) p = 0.6 bar.

Figures 4.16 and 4.17 show the PVCs of the ceramic actuator under pressures of 0.8 bar, 0.6 bar, 0.4 bar and 0.2 bar, respectively. As can be seen, the characteristics show the three sections (passive

element – transition – active element) during all pressure levels. The η-value of the passive section is 2, independently of the pressure, since the capacitance of a capacitor does not depend on the pressure. The onset voltage of the transition section is decreasing with lower pressure levels. It scales linearly with 2 kV/bar as a rule of thumb, down to 0.4 kV at a pressure of 0.2 bar. This is in a good agreement with the theory of the Paschen-curve, since the breakdown-voltage is smaller for lower pressure. Also, the transition to a fully active element ends earlier at low pressure.

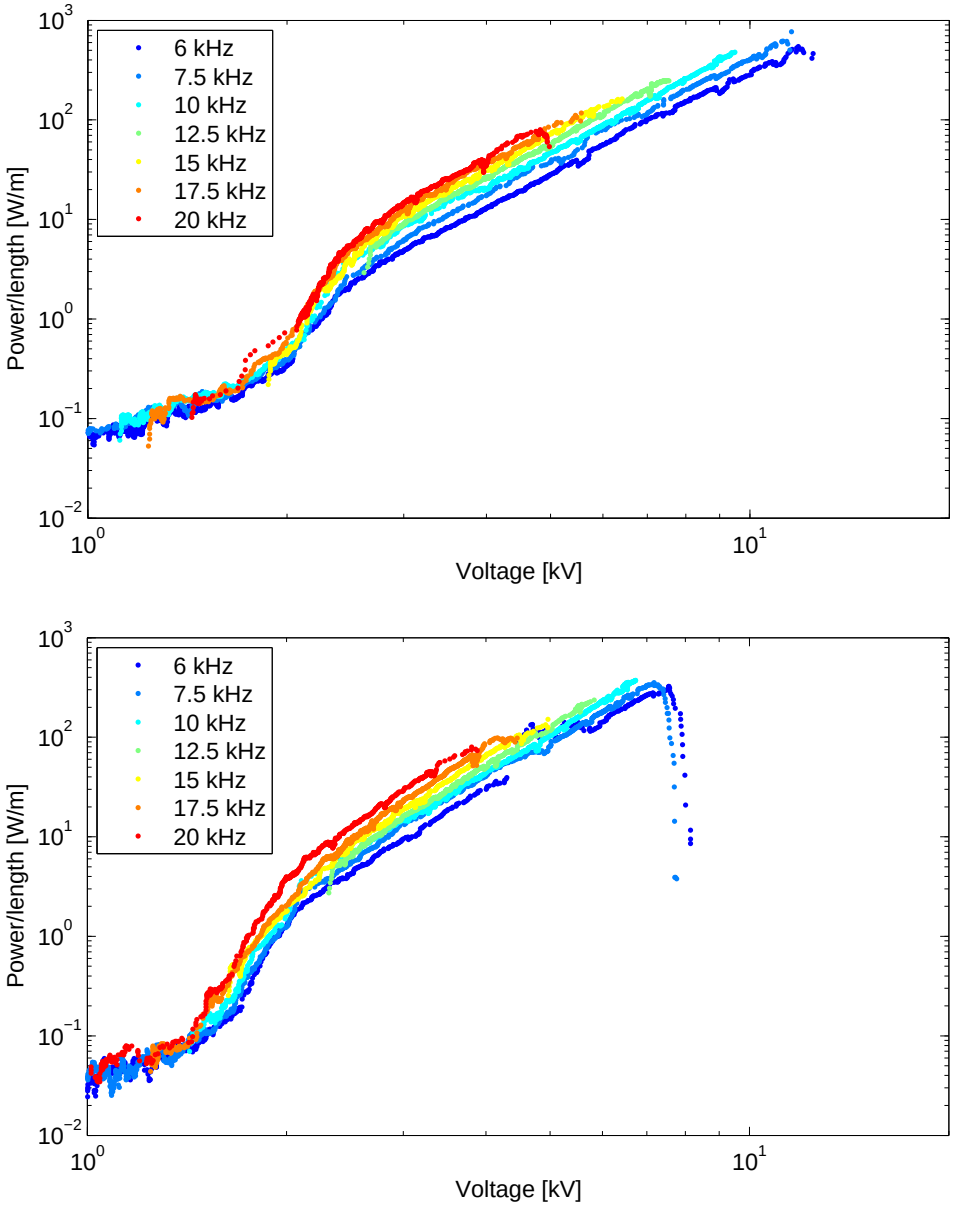

Figure 4.17: PVC of the discharge under different pressure levels and voltage amplitudes. (a) p = 0.4 bar (b) p = 0.2 bar.

In the active section, the power law $P_A \propto f \cdot V^{7/2}$ of the actuator power consumption holds during all pressure levels. With decreasing pressure but constant voltage amplitude and frequency, the plasma actuator consumes more power, due to the lower pressure and the thus higher mobility of ions in the discharge.

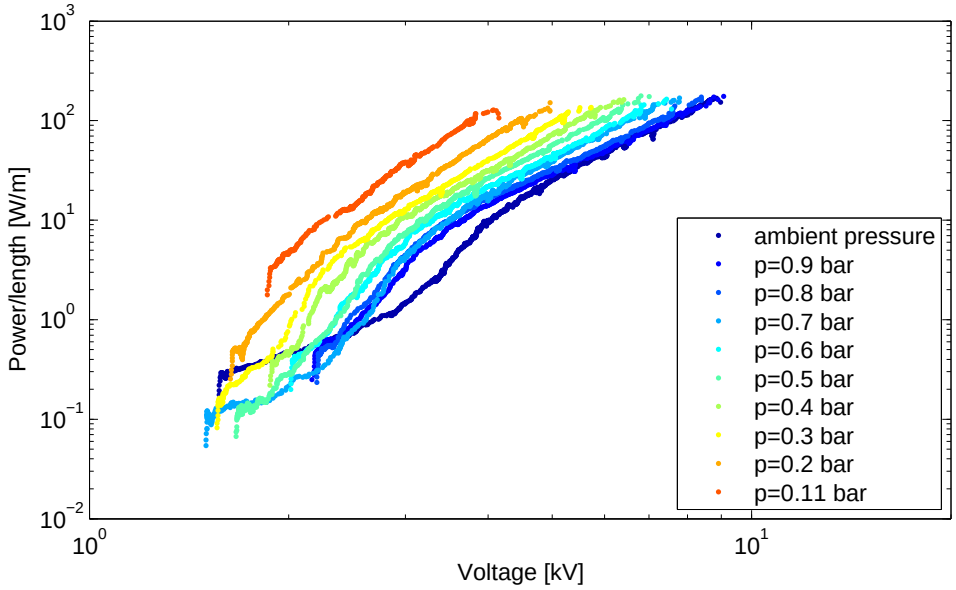

Figure 4.18: PVC of the discharge for different pressure levels between ambient pressure and p = 0.11 bar, exemplarily for 15 kHz.

Figure 4.18 shows the PVC of the ceramic actuator during different pressure levels, exemplarily for a frequency of 15 kHz. Obviously, the curves are different to each other, but parallel in the logarithmic representation. It is insightful to find scaling numbers that describe the PVC independently of the pressure. Due to the fact that the PVC shows three different sections, a unified theory would unnecessary complicated. Instead, the focus is on the active section only. Since the passive section is independent of pressure and the transition is not fully understood yet, these sections will be excluded.

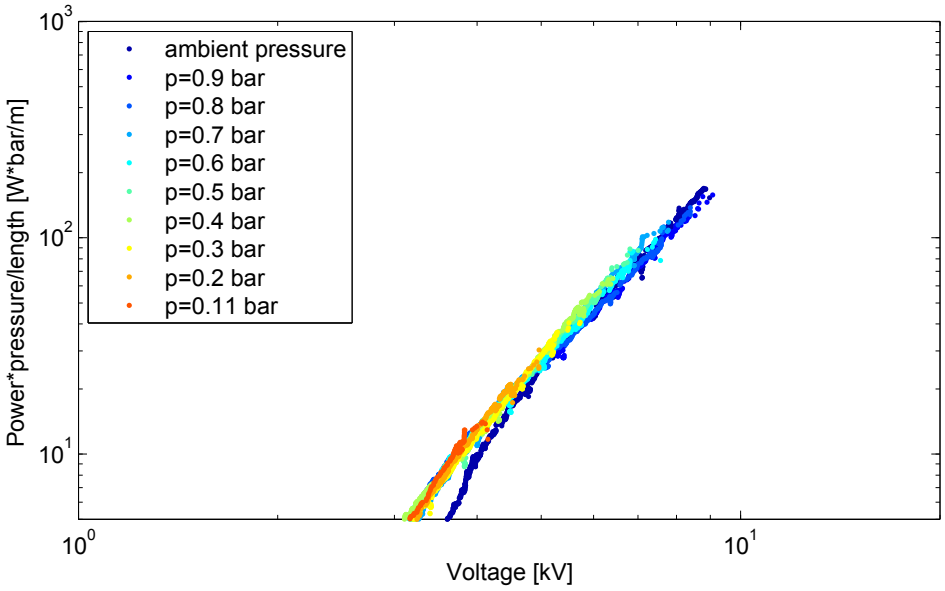

Figure 4.19: PVC of the discharge multiplied with the pressure for different pressure levels between ambient pressure and p = 0.11 bar, exemplarily for 15 kHz.

It is meaningful to use a power law dependence $P_A \propto p^{\kappa}$, as it was successfully established for other parameters (voltage amplitude, frequency). In fact, a power law is a good approximation, as can be seen in Figure 4.19. A fit revealed that the different curves coincide best for a $P_A \propto p^{-1}$ dependence when the actuator is used as an active element with a discharge. Thus, the pressure decreases the power consumption linearly. with increasing pressure, the voltage amplitude has to be increased in order to achieve the same power consumption. The same correlation applies for all other voltage frequencies used in the experiments.
Therefore, the scaling numer of the consumption of plasma actuators can be expanded to

$$\frac{P_A \cdot p}{V^{7/2} \cdot f \cdot L} \propto \Theta. \tag{4.1}$$

The theoretical explanation of this dependence will be given in section 4.3.1, as the pressure impact seems to be in strong connection to the temperature impact. First, the impact on the plasma length will be studied.

4.2.2 Impact on plasma length

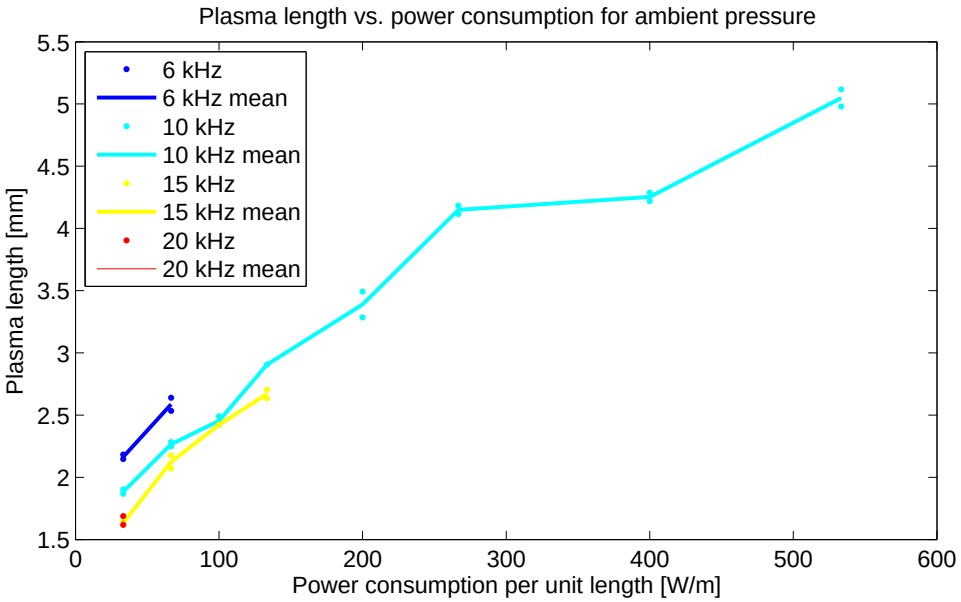

Figure 4.20: Plasma length as a function of power consumption and frequency for ambient pressure.

Figure 4.20 shows the plasma length of the ceramic actuator at ambient pressure. It is measured for a voltage frequency of 6 kHz, 10 kHz, 15 kHz and 20 kHz, respectively. Since *MiniPuls 2.1* cannot supply the actuator with high voltage amplitudes when the voltage frequency is far off resonance frequency, only few data of the power consumption is available for high and low frequencies.
Obviously, the plasma length is roughly increasing linearly with power consumption, but shows a regressive behavior at higher power levels. This can be explained due to observations made by Kriegseis in [15]. He described a linear correlation between voltage amplitude and plasma length,

$V \propto \Delta x$. Thus, the correlation between the plasma length should roughly be of $\Delta x \propto f^{-2/7} \cdot P^{2/7}$ type. It is obviously the case that the plasma length is higher for small frequencies than for higher frequencies at the same power consumption. As the correlation predicts, the differences in the plasma length becomes less dominant with higher frequencies. The curves of the plasma length for a constant frequency show a regressive dependency of the power consumption, as proposed by the scaling number, even though the exponent is rather 2/5 than 2/7.

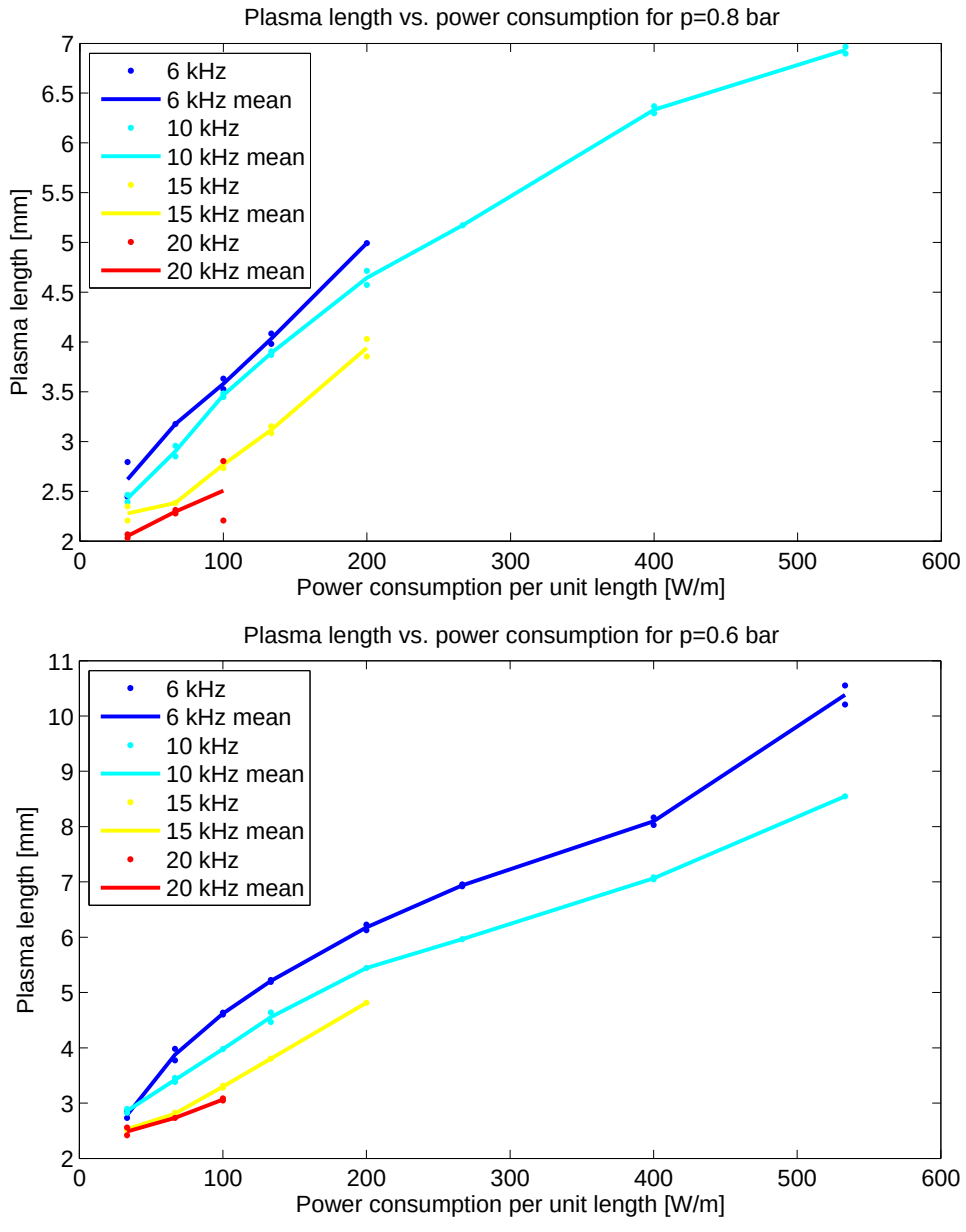

Figure 4.21: Plasma length of the discharge under different pressure levels and power levels. (a) p = 0.8 bar (b) p = 0.6 bar.

The measurement was repeated with different pressure levels, as can be seen in Figures 4.21 for p = 0.8 bar and p = 0.6 bar and 4.22 for p = 0.4 bar and p = 0.2 bar. The statements regarding the dependency of the plasma length on the voltage parameters hold, independently of the pressure. The increase in plasma length is regressive with power and decreasing with voltage frequency.

Obviously, the plasma length is strongly increasing when the pressure is decreased. At a pressure of 0.6 bar, the plasma length has increased by 50% compared to ambient pressure. At p = 0.2 bar, the plasma length is 400% the length under ambient pressure. The maximal plasma length is limited to 15 mm, the length of the lower electrode. The minimal plasma length is also increasing with decreasing pressure. The influence of the voltage frequency becomes less important for higher frequencies, independently of the pressure. Again, scaling numbers on the pressure impact need

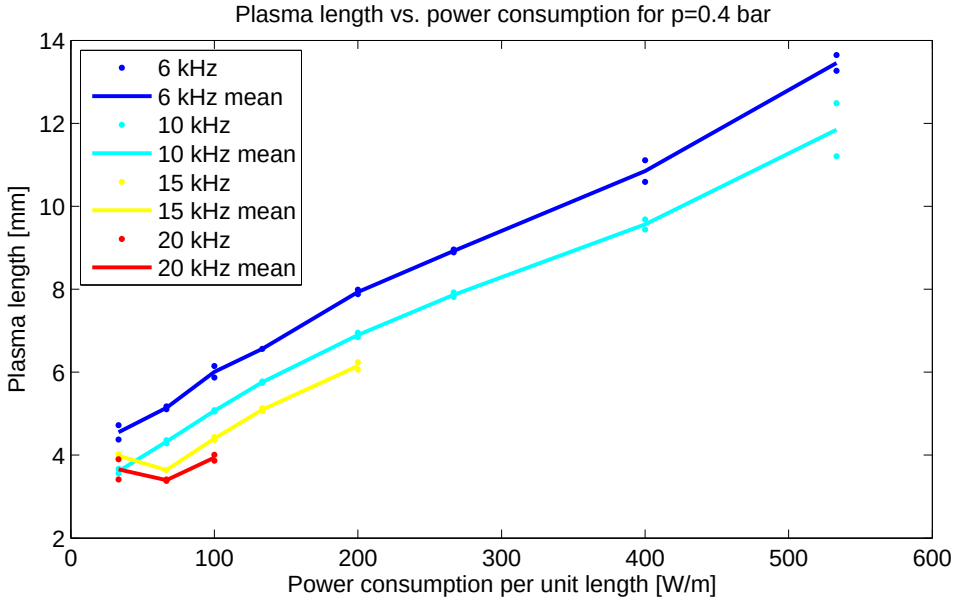

(a)

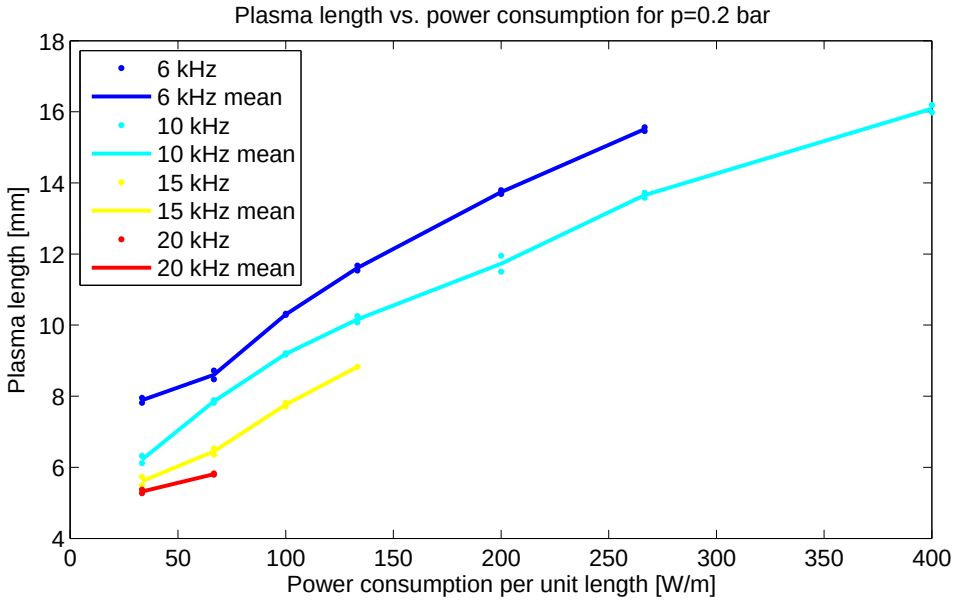

(b)

Figure 4.22: Plasma length of the discharge under different pressure levels and power levels. (a) p = 0.4 bar (b) p = 0.2 bar.

to be found. Following the argumentation of Kriegseis, a $\Delta x \propto p^{2/7}$ dependence would be appropriate, since $P_A \propto \Delta x$. In fact, a dependence such as $\Delta x \propto p^{-0.7}$ is far more appropriate, as can be seen in Figure 4.23. There is no physically satisfying explanation for this behavior available yet. In the Paschen-curve, the gap size d describes the longest distance a discharge can cross for a given voltage and pressure. Assuming that the plasma length scales with the length d, a dependence

such as $\Delta x \propto p^{-1}$ is expected to describe the dependence. This is not the case in this investigation. Hence, the Paschen-effect cannot be the only effect in the impact of the pressure on the plasma length.
In summary, it can be said that the plasma length is strongly decreasing with increasing pressure. Thus, higher power levels have to be established in order to maintain a constant plasma length under high-pressure applications. A physically satisfying explanation of the scaling number of the pressure dependence was not found yet.

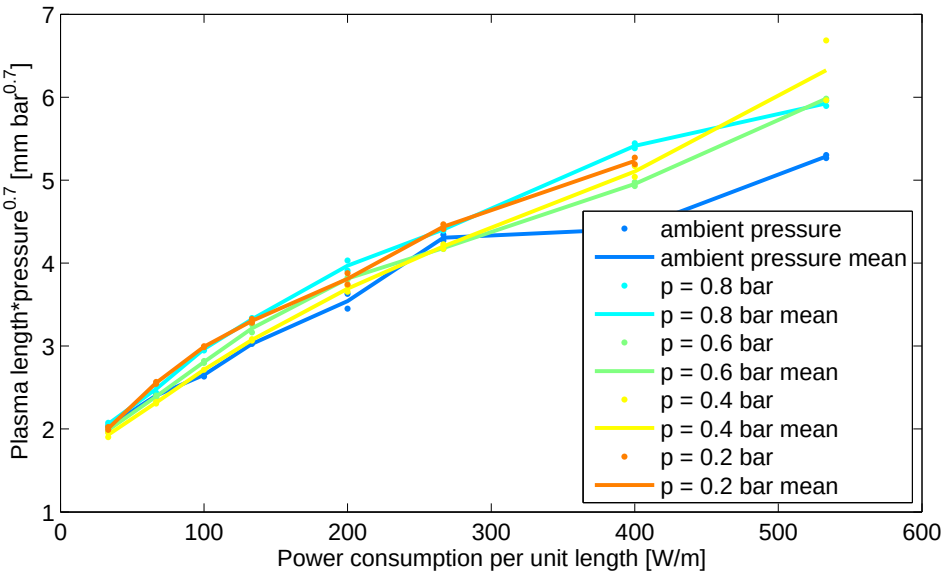

Figure 4.23: Plasma length of the discharge multiplied with the pressure scaling number for different pressure levels between ambient pressure and p = 0.2 bar, exemplarily for 10 kHz.

4.2.3 Impact on resonance behavior

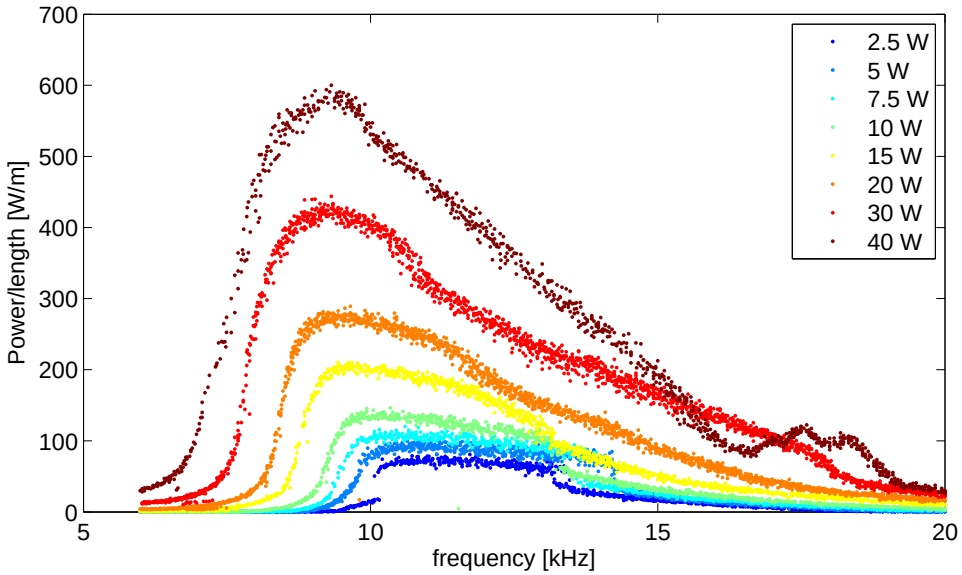

Figure 4.24: Resonance-curve of the ceramic actuator for different input voltages under ambient pressure.

In this subsection, the pressure impact on the resonance curves of a plasma actuator will be described. As described in section 2.2, the resonance frequency depends on both the impedance of the actuator and the power generation. Hence, the impact on the resonance frequency gives a good insight on the impact on the capacitance of the active actuator. For an increase in the capacitance, the resonance frequency is decreasing. This is not surprising, since even in an ideal LC-circuit the resonance frequency follows a $f_{res} = 1/\sqrt{LC}$ law. The capacitance depends on the discharge volume, since an actuator with higher discharge volume is able to contain more charges, as the electric field is decreased. Assuming the discharge volume scales with the plasma length, the resonance frequency should be smaller for low pressures than for high ones, since the plasma length is higher. This was shown in the previous section.

In order to measure this dependence, resonance curves are recorded for different input voltages and pressure levels during the experiment. The input voltages are chosen to lead to a power consumption of P = 2.5 W, P = 5 W, P = 7.5 W, P = 10 W, P = 15 W, P = 20 W, P = 30 W and P = 40 W, respectively, at a frequency of f = 10 kHz. As can be seen in Figures 4.24 - 4.26, the resonance frequency begins to shift to lower frequencies, independently of the input voltage. For the 40 W line, a second resonance frequency is visible that shifts to lower frequencies as well. This second peak is probably either a higher harmonic or arises due to a change in the high-voltage generation. For very low pressure levels, 30 W line shows the second peak as well.

Figure 4.27 shows the 20 W resonance curves of different pressure levels together in one plot. With the exception of p = 0.2 bar, the impact of the pressure on the resonance frequency is not strong. This is due to the fact that the curve is very flat at resonance frequency. Nevertheless, the effect is clearly visible. Additionally it can be seen that the resonance curve is broadening at lower

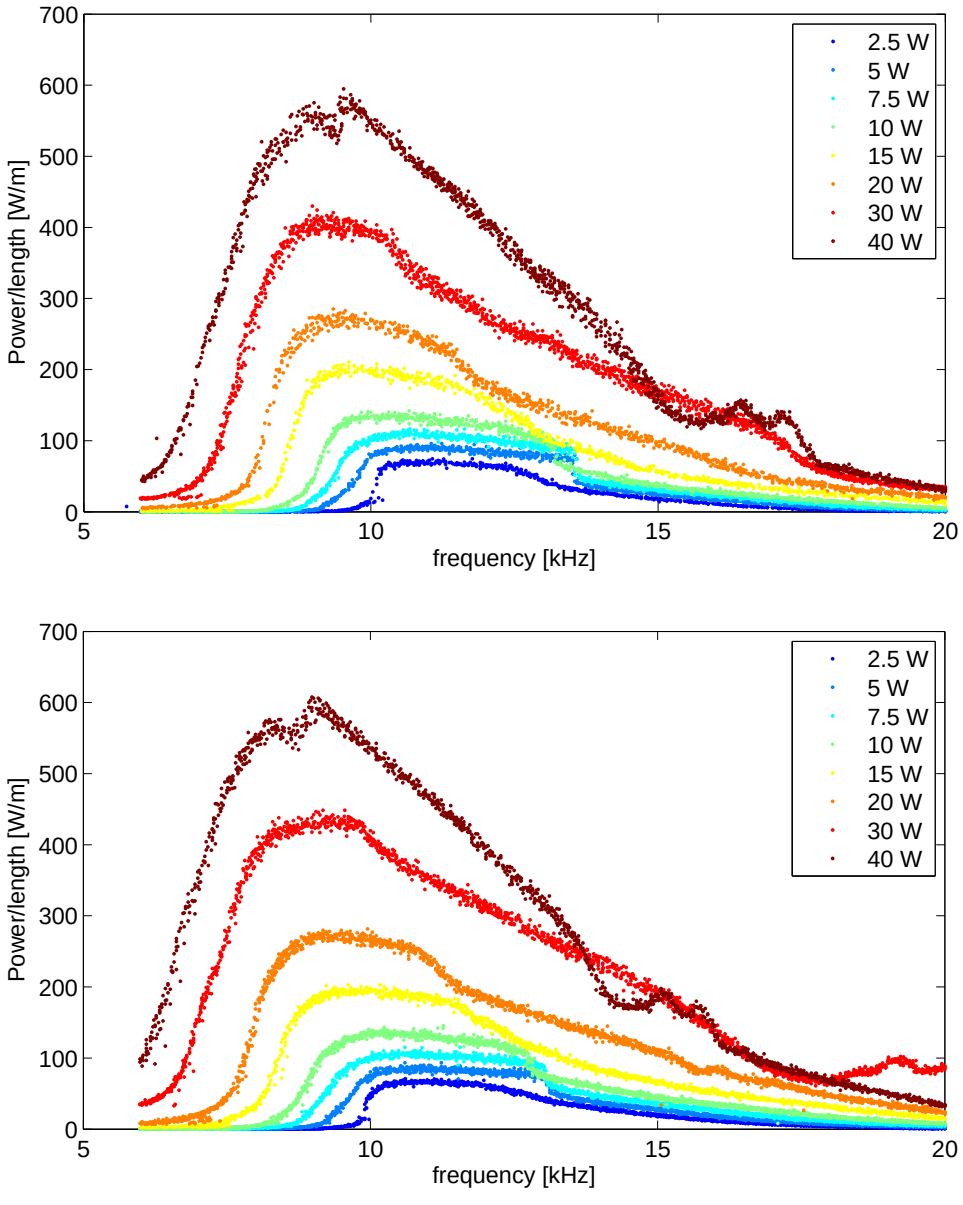

Figure 4.25: Resonance curve of the discharge for different input voltages (a) p = 0.8 bar (b) p = 0.6 bar.

pressure, since the cliff is moving to lower frequencies, but the back of the curve is has a lower slope at higher frequencies. Therefore, system becomes less sensitive to variations in the voltage frequency for low pressure, which enables to design a controller of the power consumption that has a lower dynamic behavior. At p = 0.2 bar the curve shows a totally different behavior, as the resonance frequency is significally reduced and the power consumption at the back of the curve is lower as for other input power levels. The origin of that behavior could not have been clarified yet.

In summary of the pressure impact on plasma actuators it can be said that low pressure levels improve the discharge. The Θ values are higher, thus lower voltage levels are needed in order to achieve a desired power consumption. This helps to reduce the complexity of the voltage genera-

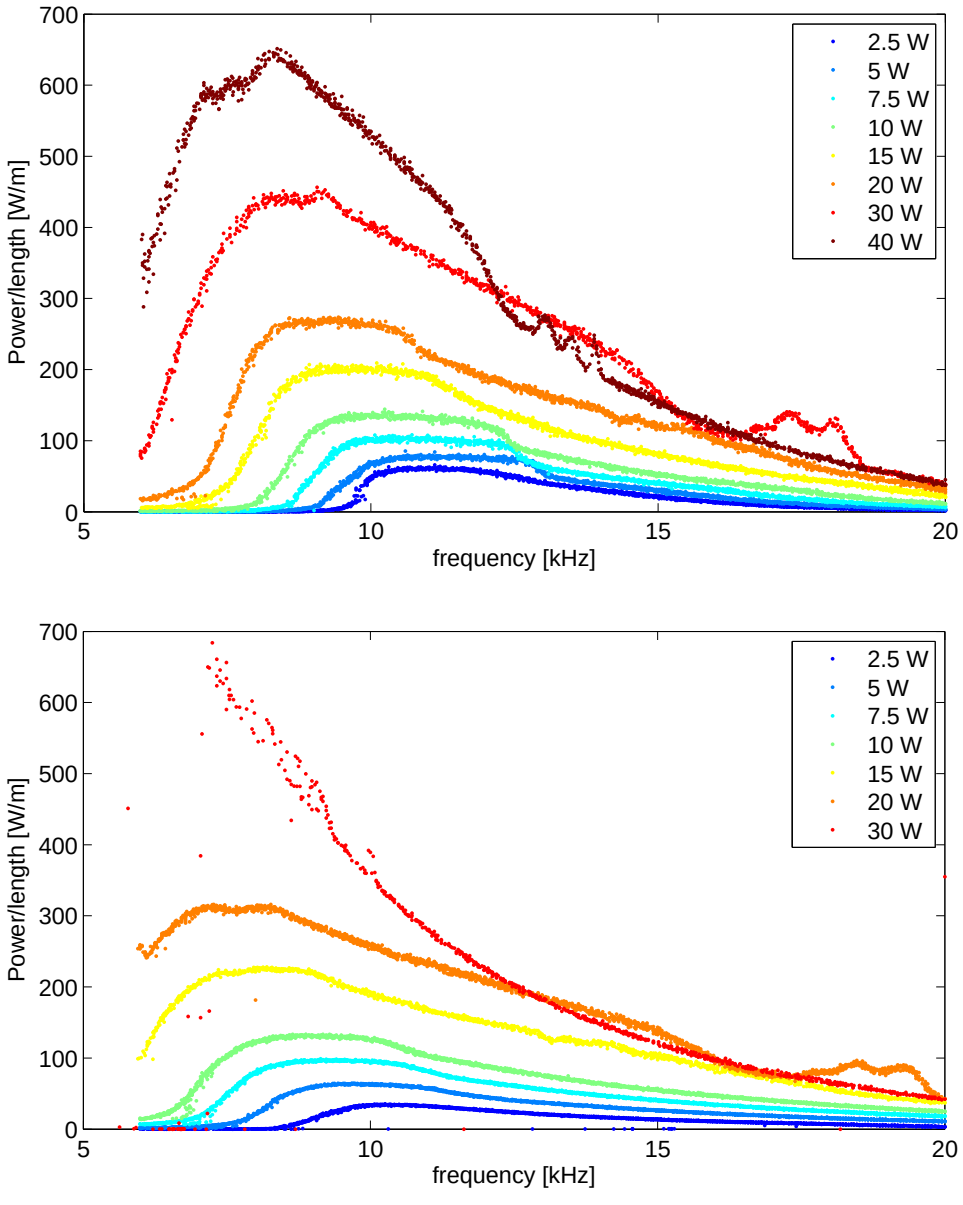

Figure 4.26: Resonance curve of the discharge for different input voltages (a) p = 0.4 bar (b) p = 0.2 bar.

tion, as the input voltage needs a smaller amplification. It is shown that the power consumption of the actuator scales anti-proportionally with the pressure, $P_A \propto p^{-1}$. Also, the plasma length is increasing with decreasing pressure. Most likely, this leads to a higher thrust production, at least to a certain level, when the decrease of the gas density exceeds the increasing velocity of the ionic wind, as shown by Abe *et al.* [6]. The plasma length scales with roughly $\Delta x \propto p^{-0.7}$. The resonance frequency is decreasing with decreasing pressure, due to a decreasing impedance. Additionally, the resonance curve is broadening. Further investigations at pressure levels above ambient pressure are needed to complete the investigations on the pressure impact.

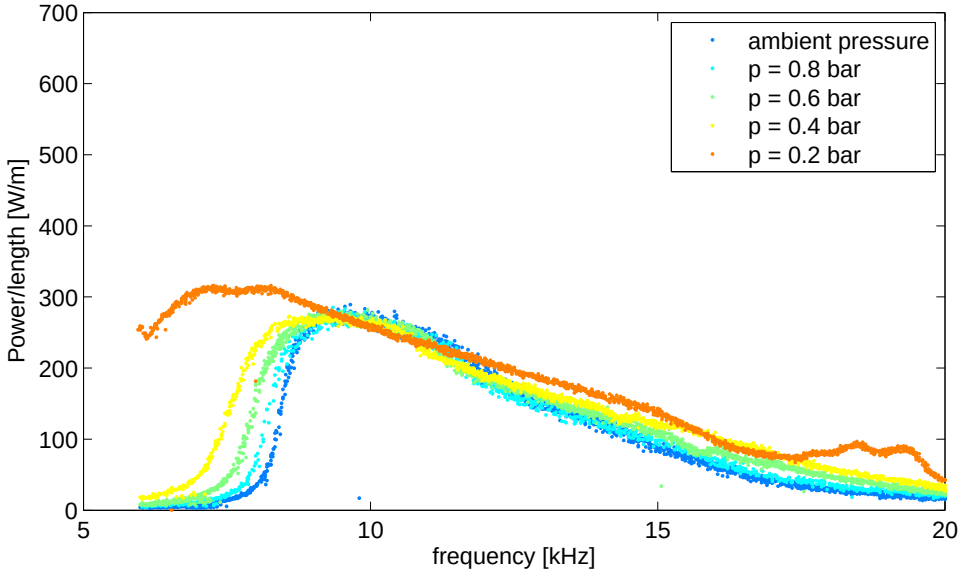

Figure 4.27: 20 W resonance-curve of the ceramic actuator for different pressure levels.

4.3 Impact of temperature

As described in section 3.4.2, two different types of ovens are used for temperature experiments, a baker oven and a furnace. The focus of the investigations is on the temperature impact on the actuator during temperature levels equal or higher than ambient temperature. The power consumption characteristic of a ceramic actuator is measured for different temperatures and voltage frequencies within both ovens. In the second subsection, the impact of temperature and voltage frequency on the plasma length is investigated. The experiments are performed in the baker oven only, since the furnace does not allow optical access. In the third section, the impact of the temperature on the resonance behavior is described, which is measured using both ovens.

4.3.1 Impact on power consumption

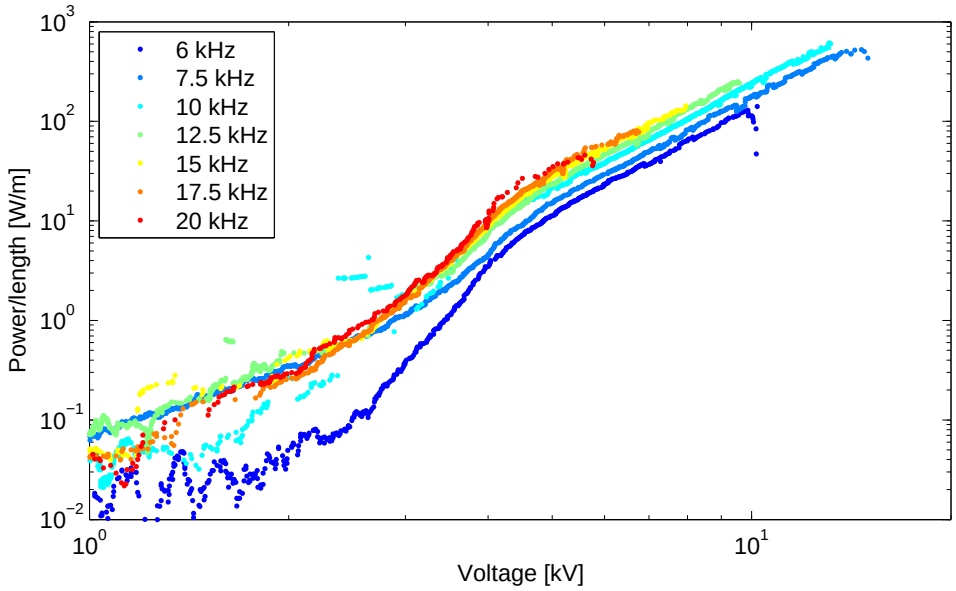

Figure 4.28: PVC of the discharge at ambient temperature and for different voltage frequencies between 6 kHz and 20 kHz.

Figure 4.28 shows the power consumption – voltage characteristics (PVC) of the ceramic actuator under ambient temperature. Since the actuator is of not the same as during the pressure experiments, but of the same geometry, the PVC is slightly different to that of Figure 4.15. The three domains – passive element, transition and active element – are evident. The slopes of the curves are the same at during the pressure experiments, as well as the location of the transition. Only during the domain of the passive element, the locations of the characteristics are slightly lower. This is probably due to a slightly higher passive capacitance of the actuator.

Figures 4.29 (a)-(e) show the PVCs of the ceramic actuator for various temperatures and frequencies. Obviously, the three domains persist during all temperature levels. Also, the exponent of the power law dependence of the consumption on the frequency remains constant 1 during all temper-

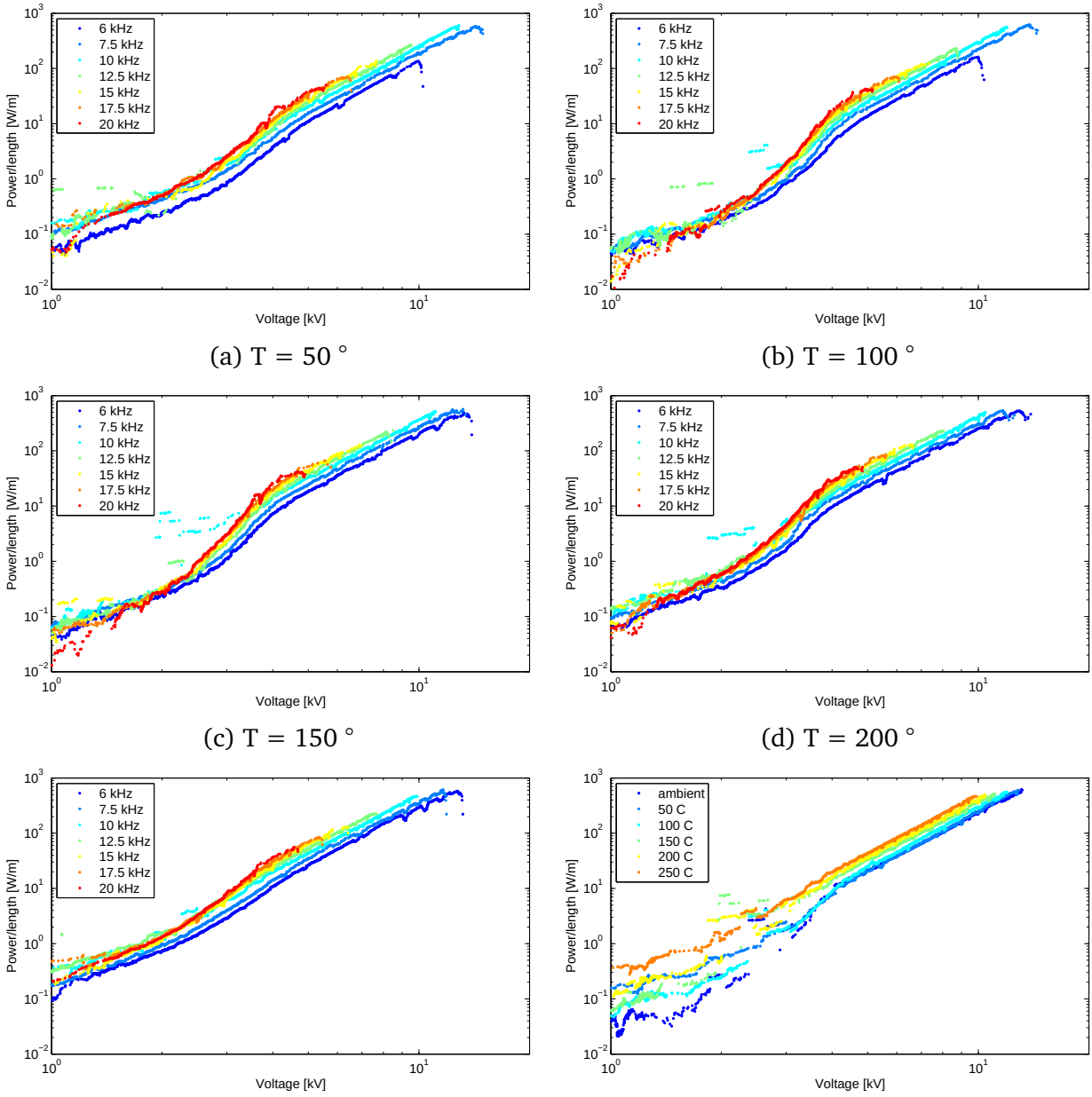

(a) T = 50 °

(b) T = 100 °

(c) T = 150 °

(d) T = 200 °

(e) T = 250 °

(f) f = 10 kHz

Figure 4.29: (a)-(e): PVCs of temperatures in between 50 °C and 250 °C and for different voltage frequencies. (f): PVC for f = 10 kHz for various temperatures.

ature levels. Generally, the power consumption of the passive element is increasing with increasing temperature. This is due to an increase of the permittivity of alumina with temperature. The increase in the permittivity increases the power consumption since more electric energy is necessary to re-orientate the electric dipoles in the barrier. The power consumption of the passive element is roughly twice as high at T = 250 ° C as during ambient temperature. Nevertheless, the power law of the PVC is roughly constant for all temperatures in this domain. The transition between the passive and the active element grows less distinct with increasing temperature, especially between T = 200 ° C and T = 250 ° C. The exponent of the PVC in this domain drops to roughly 3. Also, the onset voltage and power consumption are less distinct. This is probably due to the fact that the

power consumption of the passive element is rising stronger than that of the active discharge with temperature. Figure 4.29 (f) shows the PVCs of the actuator for temperatures between ambient temperature and T = 250 ° C, exemplarily for 10 kHz. Obviously, the power consumption of the passive element is rising more strongly than that of the active discharge. The temperature impact on the permittivity of the ceramic thus obviously exceeds that on the discharge. Since the real part of the impedance is correlated with the resistance, the real part of the passive impedance is thus increasing quicker with temperature than that of the active impedance. The power consumption during the active domain is also increasing with temperature. Nevertheless, the power law dependency $P_A \propto V^{7/2}$ of the actuator used as an active element persists during all temperatures. It is insightful to find scaling numbers for the temperature impact on the power consumption. The measurement error of the power consumption during the passive domain and the transition is too high to find reliable scaling numbers.

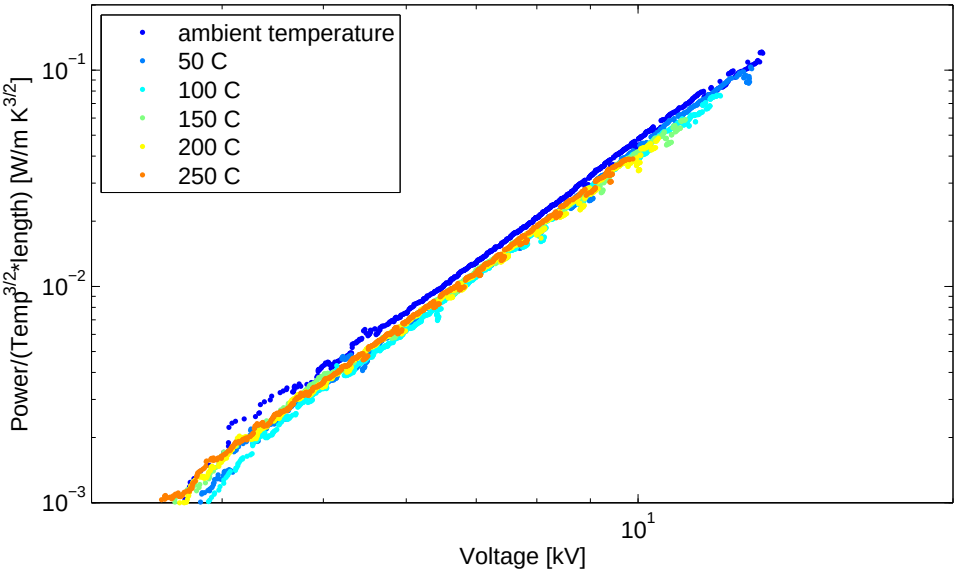

Figure 4.30: PVC of the discharge scaled with $T^{1.5}$ for various temperatures, exemplarily for f = 10 kHz.

Figure 4.30 shows the PVC of the discharge for various temperatures, scaled with $T^{-1.5}$. Obviously, the different PVCs coincide to one single line in a good approximation. The same correlation applies to all other voltage frequencies used during the temperature experiment. Thus, the power consumption of the ceramic actuator scales with $P_A \propto T^{3/2}$ with the temperature. Therefore, the power law of the environmental impact can be expended to

$$\frac{P_A \cdot p}{V^{7/2} \cdot f \cdot L \cdot T^{3/2}} \propto \Theta. \tag{4.2}$$

Presumably, two different effects contribute to the temperature impact on the power consumption of ceramic actuators:

First, the increasing permittivity of the dielectric barrier increases the power consumption of the passive element. When extrapolating the power law $P_A \propto V^2$ for the consumption of the

passive element towards higher voltage amplitudes, it can be shown that the power consumption of the passive element is more than one order of magnitude less than that of the active discharge. Therefore, the temperature dependence of the permittivity contributes to the overall temperature impact in only a minor way. The effect is assumed to scale with roughly $P_A \propto T^{0.1}$ - $P_A \propto T^{0.3}$.

The second effect is supposed to be the dominant one: The impact of the mean free path λ. The mean free path of an ion or electron in a gas is the average distance between its collisions with gas molecules. The higher the mean free path, the more energy ions or electrons can gain before colliding with gas molecules. The higher the energy of the collision is, the stronger the discharge becomes, since the electrons have a higher probability to knock out electrons. Therefore, the current of charges and thus the power consumption becomes stronger with increasing mean free path. Simultaneously, the minimal voltage necessary for a maintaining a steady discharge is decreasing. Thus, the transition between active and passive element occurs earlier. According to Kegel [14], the mean free path is roughly

$$\lambda = \frac{1}{n\sigma(T)} \tag{4.3}$$

with n the number density of the gas and $\sigma(T)$ the cross section for electron or ion collision of the gas molecules, which is temperature dependent. The number density n scales with p/T, according to the ideal gas law. The temperature dependence of the cross section is very small for air and ambient temperatures. Nevertheless, it is assumed to have a minor contribution to the temperature impact on the discharge. The impact of the mean free path would also explain why the pressure impact on the discharge scales with p^{-1}, since λ scales with p^{-1} as well. Thus, a more simplified and physically appropriate form of the power law dependency of the power consumption on temperature and pressure is

$$\frac{P_A}{V^{7/2} \cdot f \cdot L \cdot \lambda} \Re(1/\sigma(T)) \propto \Theta. \tag{4.4}$$

with $\Re(\sigma(T))$ the minor remainder term of the influence of the temperature on the cross section. For low temperatures, this impact can be neglected.

Figure 4.31 shows the PVC for various temperatures between 300 °C and 600 °C, exemplarily for f = 10 kHz, as they are measured in the furnace. Obviously, the different lines have different slopes. Also, within the transition and the passive domain, the measurements show different characteristics. This is most likely not due to a change in the discharge but more likely due to corrosion of the copper electrode as it occurs at high temperatures and a stronger increase in the permittivity of the alumina. Therefore, the measurements do not show the temperature effect on the discharge but on the passive element itself. In future studies, more appropriate actuator materials need to be used, such as tungsten for the electrode and Marcor for the barrier, since they are able to resist higher temperatures without a change in the properties than copper and alumina.

All in all it can be said that the dominant factor of the temperature and pressure impact on the discharge is the mean free path λ. The power consumption directly scales with this factor. Higher temperatures and pressures favor the discharge. Due to the higher mobility of the ions,

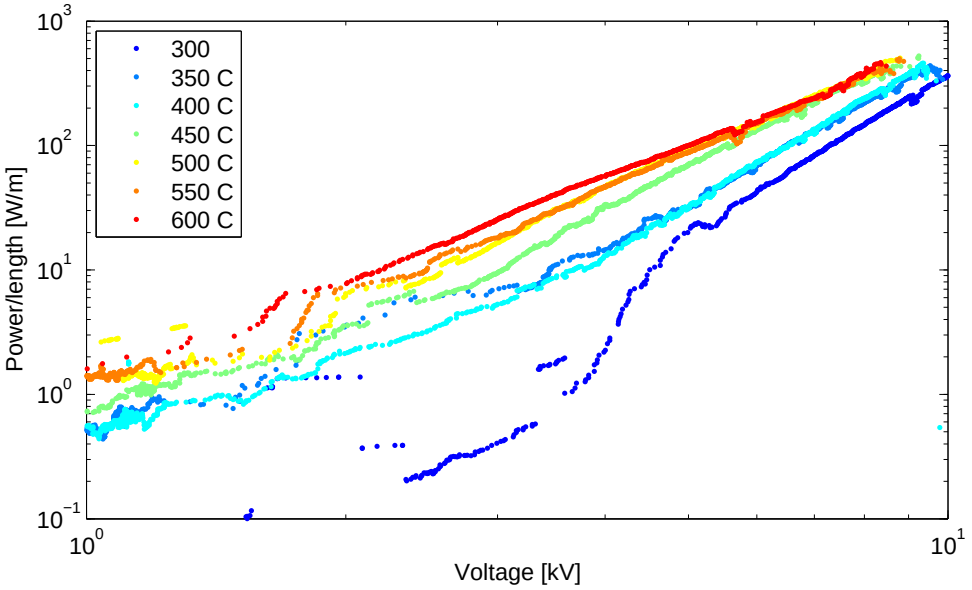

Figure 4.31: PVC of the discharge for temperatures between 300 °C and 600 °C for f = 10 kHz.

an increase of the ionic wind velocity is to be expected. Nevertheless, increase in the thrust will eventually end at a certain point, since the decreasing gas density opposes the beneficial effect of the increasing velocity.

4.3.2 Impact on plasma length

Figure 4.32 shows the plasma length of the ceramic actuator for temperatures between ambient temperature and T = 250 °C as well as frequencies between 6 kHz and 20 kHz. The length shows a regressive behavior with the power consumption, scaling with roughly $\Delta x \propto P_A^{2/5}$.

The behavior remains roughly constant during all measured temperatures. The minimal plasma length is roughly independent of the voltage frequency. With increasing power consumption, the plasma length is growing quicker for small frequencies than for higher frequencies, as it was the case during the pressure measurements. The plasma length is obviously increasing with the temperature. At 250 °C, it is roughly 30% longer than under ambient temperature.

Figure 4.33 shows the dependency of the plasma length for temperatures between ambient temperature and 250 °C, exemplarily for f = 10 kHz. Obviously, all curves show an identical power consumption behavior. As it was for the pressure, it is helpful to find a scaling number for the temperature impact on the plasma length.

As shown in Figure 4.34, the curves collapse quite well for a $\Delta x \propto T^{0.4}$ dependency. Most likely, this dependence has also to do with the Paschen-curve and the impact of the mean free path. Unfortunately, a good physical model of the correlation was not found yet. Nevertheless, it can be said that environmental impact on the plasma length follows a power law such as

$$\Delta x \propto T^{0.4} \cdot p^{-0.7}. \tag{4.5}$$

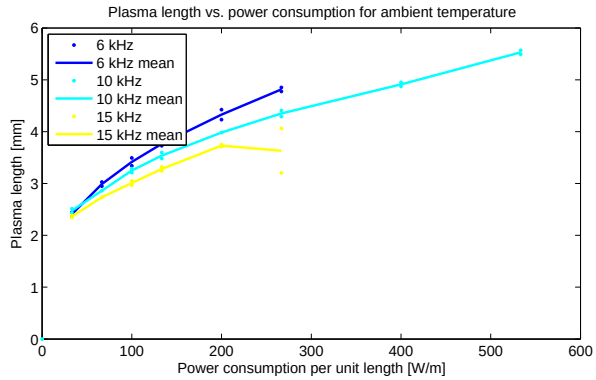

(a) ambient temperature

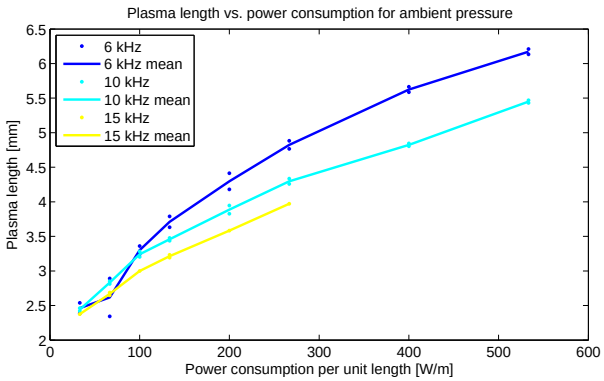

(b) T = 50 °

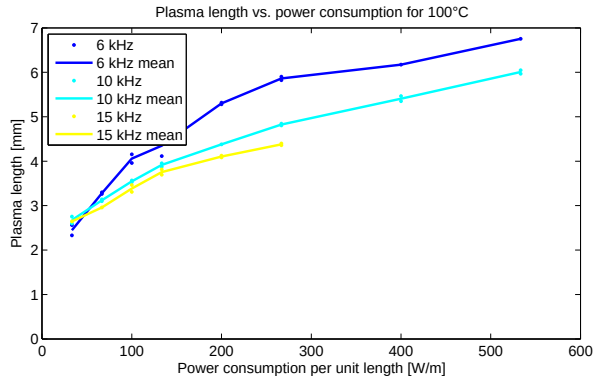

(c) T = 100 °

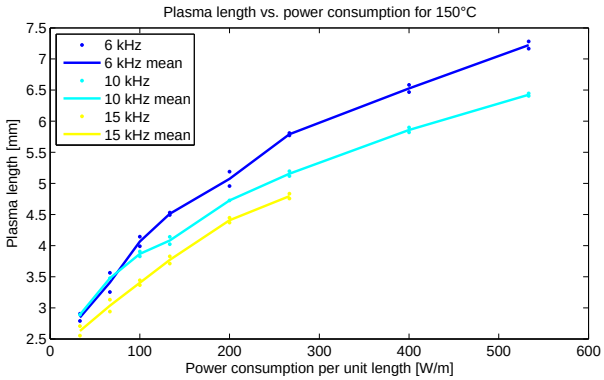

(e) T = 150 °

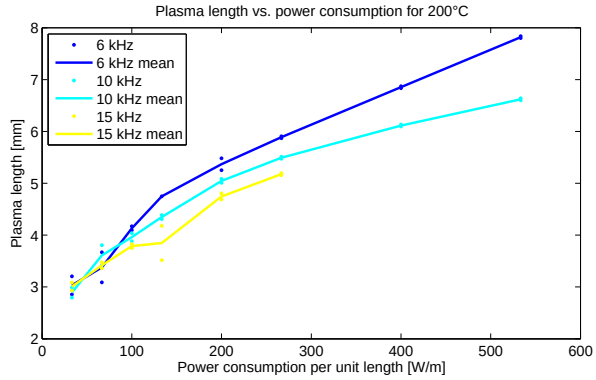

(f) T = 200 °

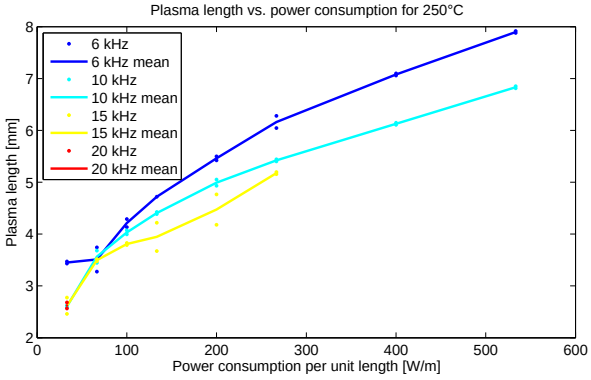

(g) T = 250 °

Figure 4.32: Plasma length of the discharge for temperatures in between ambient temperature and 250 °C and for different voltage frequencies.

for a given power level.

4.3.3 Impact on resonance behavior

During the experiments on the temperature impact on the resonance behavior of a plasma actuator, resonance curves for various temperature and input power levels are measured, as during the pressure impact experiments. The temperature was varied between ambient temperature and

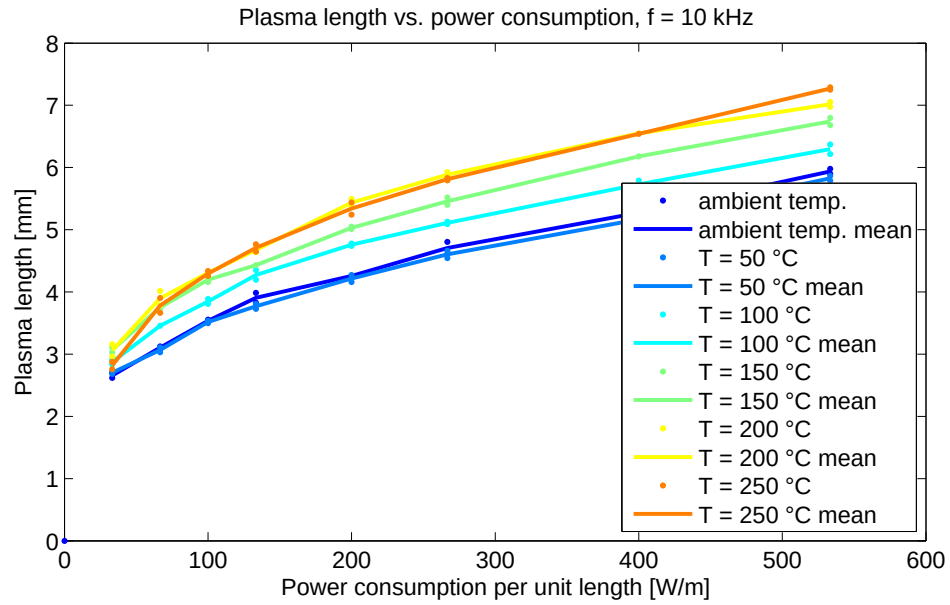

Figure 4.33: Plasma length of the discharge for temperatures between ambient temperature and 250 °C for f = 10 kHz.

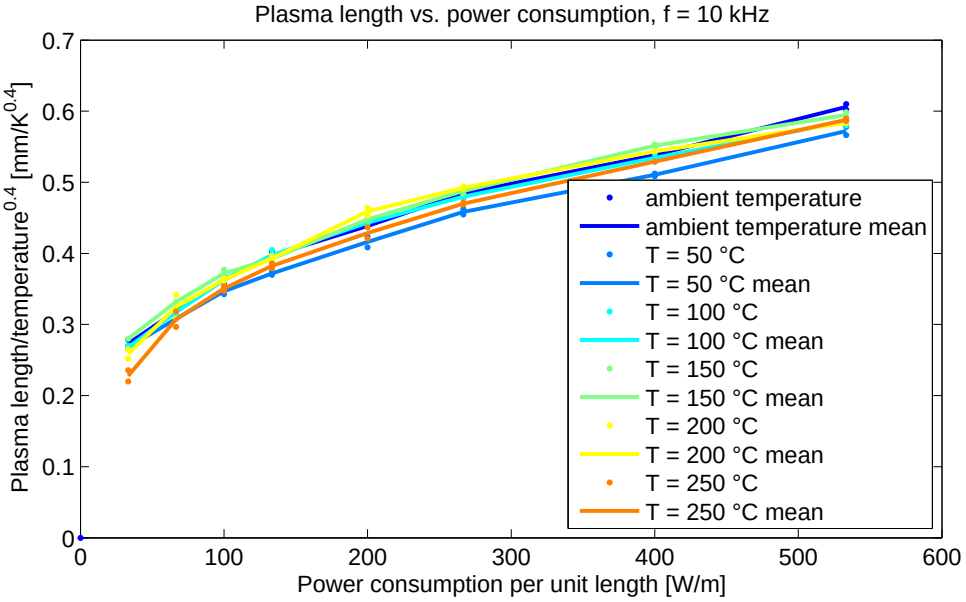

Figure 4.34: Plasma length scaled with $T^{-0.4}$.

250 °C in the baker oven and between 300 °C and 600 °C in the furnace. Figures 5.1 and 5.2 in the appendix show the evolution of the resonance curves with increasing temperature. As during the pressure experiments, the input power was chosen to lead to power consumptions of 2.5 W, 5 W, 7.5 W, 10 W, 15 W, 20 W, 30 W and 40 W, respectively, at a voltage frequency of f = 10 kHz. As described in section 4.2.3, the resonance frequency is decreasing with increasing input voltage, due to an increase in the capacitance of the active element. Obviously, this dependency of the resonance frequency on the input voltage becomes stronger with increasing temperature. The resonance frequency of the 2.5 W-curve always remains close to f = 11 kHz, whereas the 30 W-

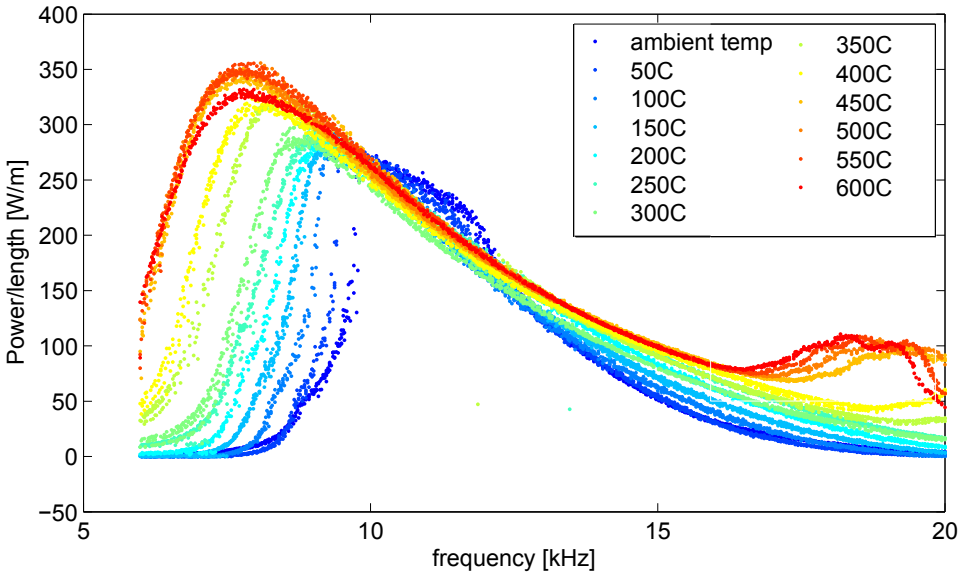

Figure 4.35: 20 W resonance curve for temperatures between ambient temperature and T = 600 °C.

curve shifts from f_{res} = 10 kHz to roughly f_{res} = 7 kHz. Therefore, it becomes more important to control the input power at higher temperatures, since small variations of the input voltages or the temperature cause significant variations in the resonance curve. It can also be concluded that the imaginary part of the active element's impedance is increasing more quickly with temperature than that of the passive element.
Additionally, the higher harmonic is visible in the 40 W-curve during all measurements. With increasing temperature, the frequency of the harmonic is decreasing, just as the resonance frequency. For reasons that cannot be explained yet, the frequency of the harmonic is decreasing faster than the resonance frequency. Starting with a temperature of T = 100 °C, the higher harmonic of the 30 W-curve becomes also visible. At T = 400 °C, even the harmonic of the 20 W-curve becomes visible. Figure 4.35 shows the evolution of the 20 W-resonance curve between ambient temperature and T = 600 °C. Obviously, the resonance frequency is decreasing with increasing temperature. The power consumption at resonance frequency is increasing with increasing temperature. Also, not only the resonance frequency is lowered, but also the power consumption at the back of the curve increased. This is most likely due to the increase of the power consumption at resonance frequency.

The decrease of the resonance frequency is most likely due to two effects: First, the passive capacitance is increasing due to an increase in the permittivity of the dielectric barrier, as described in subsection 4.3.1. Secondly, the discharge volume and the number of charges in the discharge zone is strongly increasing with temperature, since the free mean path greater. This effect increases the capacitance of the active element further. Combined, the two effects increase the active capacitance of the plasma actuator and lower the impedance. Thus, the resonance frequency is decreasing. The impact of increasing temperatures is very similar to that of decreasing pressure, as the assumption of the mean free path as the dominant scaling number predicts. It can therefore be assumed that the mean free path is the dominant factor of the impact on the resonance behavior

as well.

In summary of the temperature impact it can be said that higher temperatures favor the discharge. The power consumption is higher, since more and stronger discharges occur. It was shown that this effect scales with $P_A \propto T^{3/2}$. Also, it was shown that there are good reasons to assume the mean free path as the dominant impact factor on the discharge behavior. Thus, a model with the mean free path as scaling number of the power law of the power consumption is more appropriate:

$$\frac{P_A}{V^{7/2} \cdot f \cdot L \cdot \lambda} \Re(1/\sigma(T)) \propto \Theta \tag{4.6}$$

Also, it was shown that the plasma length scales with $\Delta x \propto T^{0.4}$. A reasonable theoretical model for this effect was not found yet. The resonance frequency is decreasing with increasing temperature, since both, the capacitance of the active and the passive element, are increasing. The increase in the passive capacitance is due to a higher permittivity, the increase in the active capacitance due to a greater plasma length, a greater discharge volume and an increased number of charges in the discharge volume. This is most likely also due to an increase in the mean free path.
During the next section, the environmental impact on discharge-instabilities is described.

4.4 Impact on discharge-instabilities

During this section, the impact of environmental conditions on discharge-instabilities is studied. In the first subsection, the impact of the flow on the onset-voltage of the instabilities are measured and compared to the theoretical model described in section 2.3. Also, the impact of the flow orientation on the formation of the filaments is studied with the help of thermo-camera images. In the second and third subsection, the impact of pressure and temperature on the onset voltage and the filament spacing is studied.

4.4.1 Impact of flow velocity on discharge-instabilities

During the first part of this subsection, experiments made by Bürkle in [13] are described. In these experiments, an actuator was placed in the Small Eiffel Wind Tunnel. The impact of the flow velocity on the onset voltage of instabilities was measured and compared to the theoretical model described in 2.3.

Impact on onset-voltage

It is insightful to know whether an external air flow can have an influence on the large-scale filaments. Within [13], Bürkle showed that that the occurrence of the filaments due to discharge-instabilities does not influence the power consumption/ voltage-caracterisitics of a plasma actuator in quiescent air. The same fact holds for flow velocities between 3 m/s and 21 m/s, as can be seen in Figure 4.2. The onset voltages for an unstable discharge range from 11 kV to 15 kV for the different flow velocities, but a change in the slope of the PVC is not evident. The minor variations of the PVC at voltage amplitudes higher than 14 kV are most likely generated by a change in the actuator geometry. The change is due the power dissipation in the dielectric barrier which generates temperatures during that voltage amplitude. Thus, the adhesive of the dielectric barrier starts to detach.

Nevertheless, onset voltage amplitude for the instabilities depends on the flow velocity, as the instability equation 2.20 of section 2.3.3 predicts.

$$n_e E^2 > \nu_{dc}/(1+\nu^*) N c_p T \tag{4.7}$$

The dependency is not evident, but, since the heat removal frequency $\nu_{dc} = \chi/\Lambda_T^2 + 2 \cdot u/\Delta x$ is linearly dependent on the flow velocity, the critical electric field is also dependent on the flow velocity. Thus an increase in the flow velocity increases the threshold of an unstable development. The threshold follows the law

$$E = \sqrt{\frac{(\chi/\Lambda_T^2 + 2 \cdot u/\Delta x)/(1+\nu^*) N c_p T}{n_e}} \tag{4.8}$$

Most of the coefficients, such as χ, Λ and n_e are unknown for the given discharge but assumed to be constant. Nevertheless, the voltage threshold characteristic should follow a

$$E = a \cdot \sqrt{b + u} \tag{4.9}$$

dependency, with a and b being unknown coefficients. Most importantly, those coefficients are approximately constant for constant actuator geometry and small variations in the temperature and pressure.
When the convective cooling is dominant compared to the diffusive cooling, as it is the case for $u/\Delta x >> \chi/2\Lambda_T^2$, equation 4.9 simplifies to

$$E \approx a \cdot \sqrt{u} \tag{4.10}$$

Figure 4.36 shows the dependency of the onset voltage for instabilities on the flow velocity for different sizes of instabilities. The actuator electrodes are mounted perpendicular to the flow in this experiment, such that the induced flow of the actuator and the external flow move in the opposite direction. Additional experiments showed the same dependency for different flow orientations. Within [13], Bürkle did not provide a precise definition of the onset voltage for the development

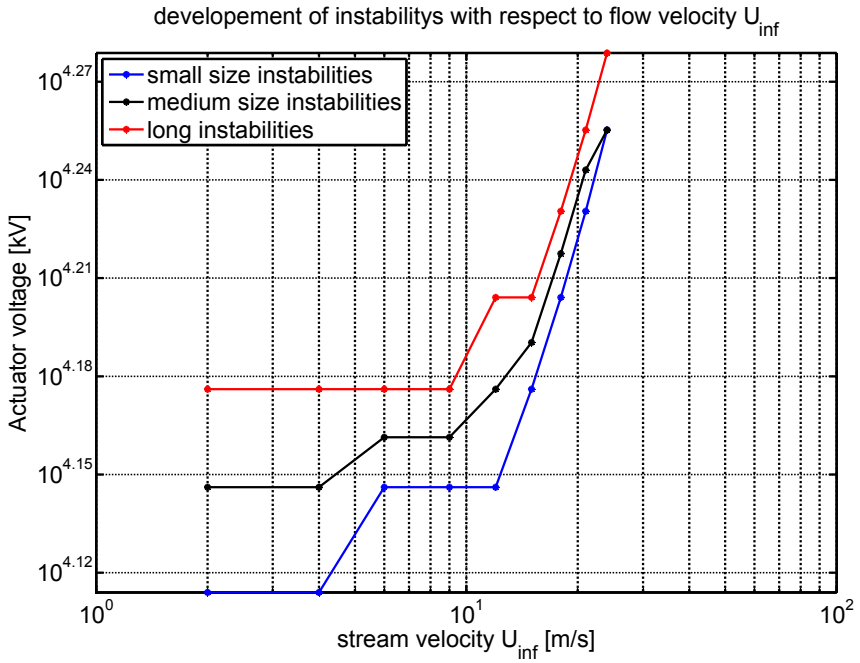

Figure 4.36: Dependency of the onset-voltage amplitude for an unstable discharge on the flow velocity in a logarithmic plot

of filaments with the help of a mathematical model, as it was done in this work. Therefore, three different types of instabilities were defined, dependent on their length. Small instabilities have a length less than 2 mm and are very thin, medium instabilities have a length of about 2-6mm and long instabilities a length greater than 6mm. The onset voltage of medium size instabilities is assumed to be the onset voltage of the unstable process, in order to have a more precise definition

of the onset voltage. Small-size and long instabilities are assumed to indicate the error of the measurement.
A closer look at the onset voltage/flow velocity-characteristic in Figure 4.36 shows that for high flow velocities and thus high convective cooling rates the slope of the function in a logarithmic plot remains roughly constant. That means that the exponent of the function is constant. It has a value of 0.360 ± 0.088 and is thus in a good agreement with the theory, since equation 4.10 proposes a value of 0.5. Considering that the theoretical model is obtained under strong simplifications, such as assuming the electric field to be homogeneous or the ionic wind velocity negligible, the model is in good agreement with the experiment.
This dependency shows a strategy to prevent the most undesired effect of the instabilities when necessary: the fatigue in the dielectric barrier due to high temperature and the highly energetic ions in the instabilities. It is desirable to prevent the instabilities in order to increase the actuator lifetime. According to the measurements, the drop in the lifetime can be prevented when the actuator is only used in external flows with a high flow velocity, such that the instabilities are prevented.

Within [13], Bürkle studied the impact of discharge instabilities on the temperature distribution of the dielectric barrier. As predicted by the theoretical model of the discharge instabilities, the temperature in the vicinity of the filaments was rising. It is thus of interest what impact of the flow and the flow orientation on the filaments and thus the temperature-distribution can be observed. Since the onset voltage of the discharge instabilities depends on the cooling rate and thus the flow velocity, the orientation of the external flow with respect to the direction of the ionic wind should also have an influence on the discharge an thus on the temperature distribution. This influence is investigated within an experiment described in the following.

The Kapton actuator is mounted in different orientations in the test section of the Small Eiffel Wind Tunnel. The three configurations are counter-flow, co-flow and orthogonal-flow orientation. The flow velocity is varied between 0 and 21 m/s, the voltage amplitude between 10.5 kV and 18 kV. The 10.5 kV level is the highest possible voltage amplitude of a discharge without filaments in quiescent air for a Kapton actuator. The images were taken with a *Optris PI160* thermo-camera by *Optris Infrared Thermometers GmbH*. The systematical error of the camera is ±2K or ±2%. It is fixed 30 cm above the plasma actuator during all experiments.
Figure 4.37 shows the temperature distribution of a discharge with filaments at 14 kV in quiescent air. The long equally spaced filaments are clearly visible in the region of high voltage close to the upper electrode. Further downstream, the area with smaller discharge strength remains homogeneous and stable. The temperature of the filaments is about 160°C. Discharges with a temperature of this level show a high fatigue in the dielectric Kapton and are thus to be avoided.
The nature of this 14 kV discharge changes completely when the actuator is exposed to an exter-

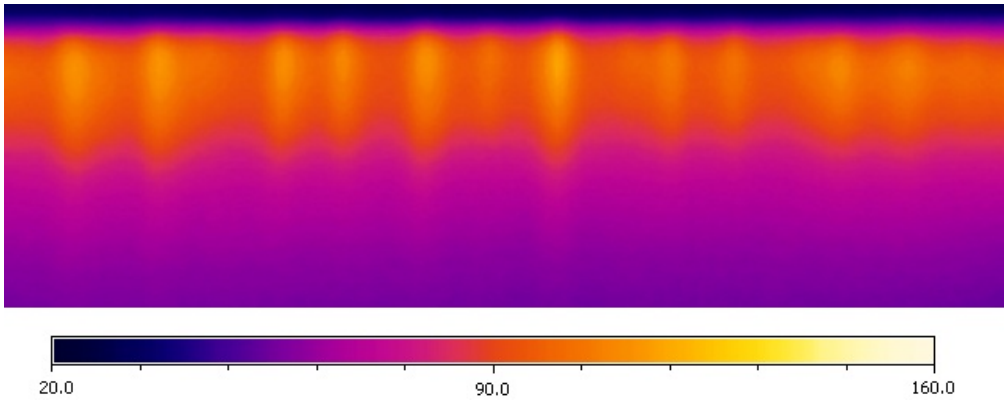

Figure 4.37: Temperature distribution of a 14 kV discharge in quiescent air.

nal flow. Figure 4.38 shows the same discharge as in Figure 4.37, but for an flow of a velocity of 21 m/s and different orientations. The temperature is considerably lower than in quiescent air, due to the increased cooling rate. The co-flow discharge is completely homogeneous with an average temperature of 90°C. The length of the heated region has decreased compared to quiescent air.
The counter-flow has a much shorter heated region compared to all other orientations. However, the heated region close to the upper electrode reaches a temperature considerably higher than during the co-flow orientation of about 120°C. The heat distribution is inhomogeneous with hot

spots. The width of the spots is large compared to the length and they are not equally spaced. Thus, it is not clear whether they arise due to instabilities or are rather inhomogeneities of the heat production and cooling rate.

The orthogonal orientation shows a behavior between the co-flow and counter-flow orientation.

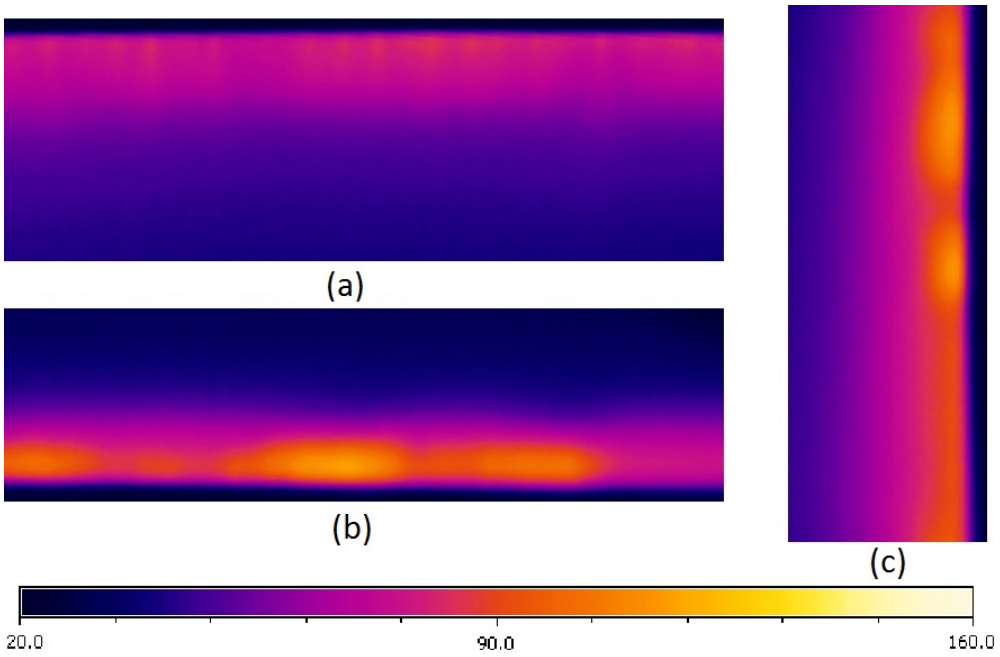

Figure 4.38: Temperature distribution of a 14 kV discharge in an external flow of 21 m/s. (a) co-flow (b) counter-flow (c) orthogonal flow.

The heated region is reduced compared to the co-flow, but still larger than during the orthogonal flow. The high voltage region close to the upper electrode is colder and less inhomogeneous than in the co-flow case, but more homogeneous than in the counter-flow orientation.

The power consumption of all three configurations is the same of roughly 346 W/m. Thus, the rate of cooling is the only parameter that is different within the different settings. The cooling rate effects the discharge stability and therefore the heat release. The cooling rate is effected by the flow velocity u. In the parallel configuration, the ionic wind increases the velocity of the external flow in the boundary layer ($u = |u_{external}| + |u_{ionic}|$), especially in the region of high body force close to the upper electrode. This area is also the area of the highest voltage drop and is thus the first one to show filaments.

The counter-flow has the reverse impact. Since the external flow and the ion wind move in opposite directions ($u = |u_{external}| - |u_{ionic}|$), the velocity of the boundary layer is lowered in the area of high body-force close to the upper electrode. The lowered flow velocity and thus lower cooling rate causes the discharge in this area to become instable at lower voltages than in the co-flow orientation. The velocity of the boundary layer further upstream of the upper electrode is higher. Thus, the cooling rate is higher and the discharge more stable.

These effects reduce the heated region in the counter-flow compared to the co-flow orientation and the heat release is enhanced in the area close to the upper electrode in the latter case.

In the orthogonal orientation, the absolute velocity ($u = \sqrt{u_{external}^2 + u_{plasma}^2}$) is greater than in

the counter-flow orientation but less than in the co-flow orientation. Therefore, the heat distribution ranges in between the two other cases. Differences arise due to the fact that the heated air is transported to downstream regions of the discharge. Thus, the temperature in these regions is higher.

All effects described above become stronger at a higher voltage amplitude. The heat distributions of a plasma actuator driven by a voltage amplitude of 18 kV is shown in Figure 4.39. Using the actuator in quiescent air under these conditions would quickly destroy it due to the high thermal fatigue. Within the flow with a velocity of 21 m/s, the actuator has a significantly larger lifetime since the temperature and the fatigue are smaller. The co-flow configuration clearly shows

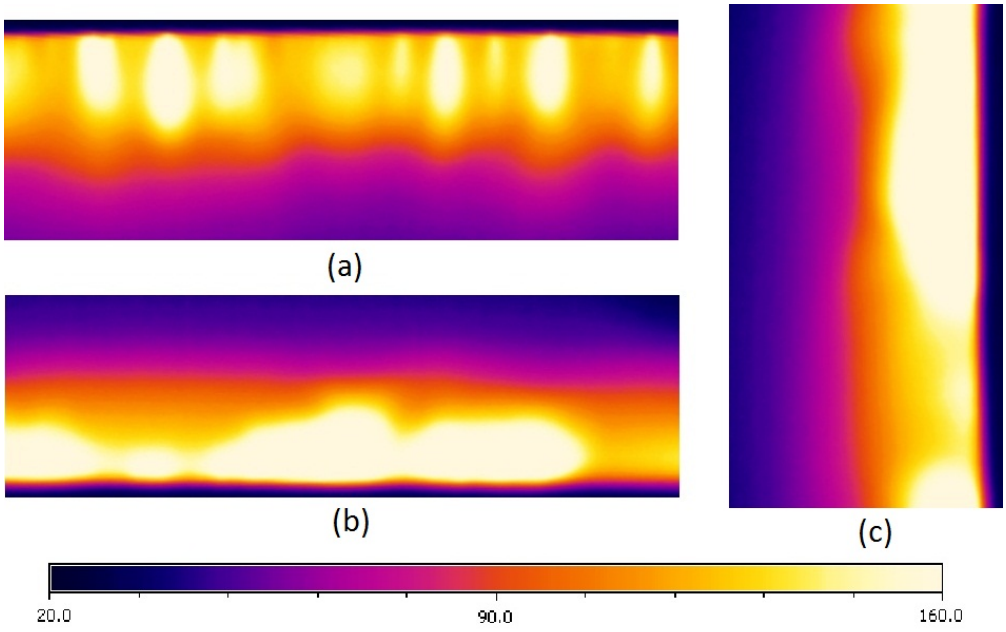

Figure 4.39: Temperature distribution of a 18 kV discharge in an external flow of 21 m/s. (a) co-flow (b) counter-flow (c) orthogonal flow

instabilities, with a spacing similar to those in quiescent air for a 14 kV voltage amplitude. The temperature is about 240 °C and thus higher than in the 14 kV case in a 21 m/s flow velocity. Some of the instabilities are more dominant than others. Presumably, this is due to the fact that at high voltages some of the filaments grow together, as the processes of the instability cycle becomes stronger. The counter-flow and orthogonal orientation show great inhomogeneities, as it was the case before. This is presumably due to an increased heat generation within a small region which is caused by the inhomogeneities. This heat is quickly distributed by the flow, creating the hot spots.

In summary it can be said that a flow inhibits the formation of instabilities. The onset voltage follows the dependency of the theoretical model in good agreement. The flow orientation seems to have an impact on the instabilities as well. During the next two sections, the impact of pressure and temperature on the onset voltage and filament spacing will be studied.

4.4.2 Impact of pressure on discharge-instabilities

Within this subsection, the impact of the temperature on the onset voltage of the discharge-filaments will be described. Afterwards, the impact of pressure, voltage amplitude and frequency on the average spanwise spacing between two filaments will be studied.

Impact on onset voltage

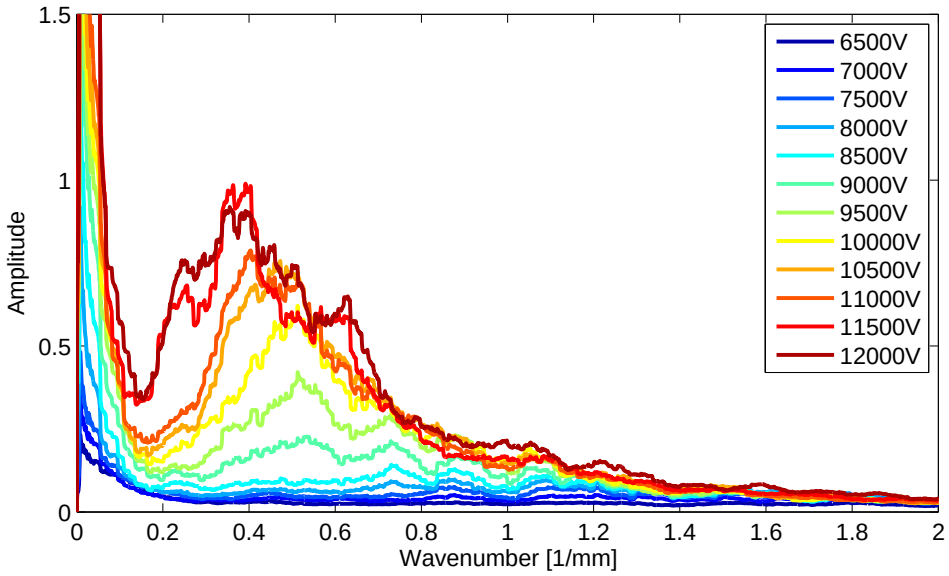

Figure 4.40: Amplitude spectrum of the filaments, captured for a voltage frequency of 10 kHz and ambient pressure.

As described in section 3.5, the onset voltage is determined with the help of the amplitude spectrum of the discharge's relative luminosity. An exemplary amplitude spectrum can be seen in Figure 4.40 for ambient pressure and temperature, a voltage frequency of 10 kHz and multible different voltage amplitudes. At a voltage amplitude of 9 kV, the spectrum begins to show a broad peak at a wavenumber of roughly 0.6 mm^{-1} due to the onset of filaments. The wavenumber is the inverse of the mean spacing between two filaments. It is thus evident that the onset voltage of the filaments corresponds to the minimal voltage that shows a peak in the amplitude spectrum. From the location of the peak, the mean spacing between the filaments can be derived for the given conditions. The amplitude spectra of the relative luminosity of all pressure levels, voltage amplitudes and frequencies that have been used during the experiments can be seen in Figures 5.3 and 5.5 in the appendix.

Figure 4.41 (a) shows the development of the onset voltage with pressure. Obviously, the voltage scales linearly with increasing pressure, i.e. a higher pressure inhibits the filaments. This is in agreement with equation 2.19 that predicts a higher onset voltage with increasing pressure.

Nevertheless, according to the equation, the dependency should not be linear but regressive, since $E \propto \sqrt{p}$. The origin of this discrepancy could not be explained. One reason might be, that the range of pressure levels is too small to observe the regressive dependency properly.

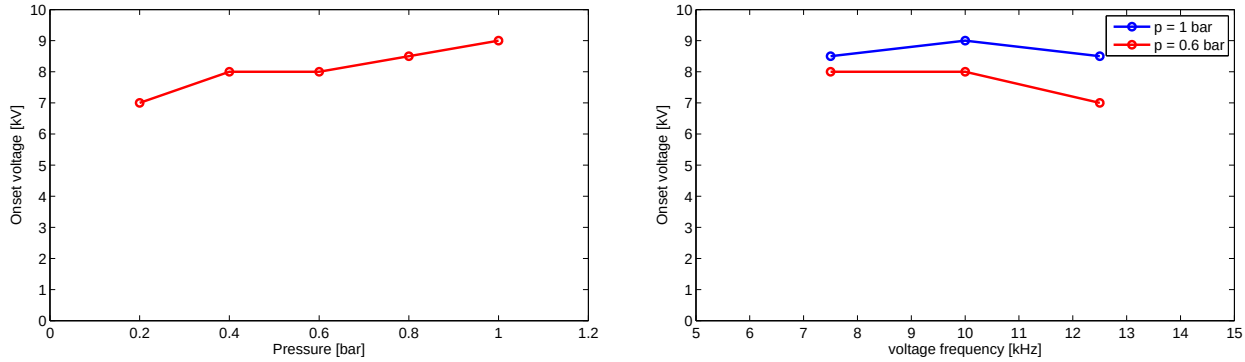

(a) (b)

Figure 4.41: Onset voltage of the formation of filaments as function of (a) pressure with a frequency of 10 kHz and (b) pressure and frequency.

Besides the experiments of the pressure impact on the onset voltage, additional experiments are made. The onset voltage is measured for three different voltage frequencies, 7.5 kHz, 10 kHz and 12.5 kHz, respectively, under ambient pressure as well as p = 0.6 bar. The results can be seen in Figure 4.41 (b). As already shown above, the onset voltage is higher for a higher pressure level. Additionally, a small impact of the voltage frequency is evident, but due to the raw measurement points a precise dependency can not be given. It can be said that the impact of the voltage frequency on the onset voltage is rather small between 7.5 kHz and 12.5 kHz.

Within the next subsection, the dependence of the filament spacing on the pressure, voltage frequency and amplitude will be studied.

Impact on filament spacing

From peaks in the amplitude spectra of Figures 5.3 and 5.5, the mean wavenumber of the filaments can be identified. The inverse of the wavenumber k yields the average spacing s between the filaments. For high pressure, the wavenumber can be identified easily, as the peaks are very distinct. The results of the experiments with a voltage frequency of 10 kHz can be seen in Figure 4.42. Obviously, a decreasing pressure stongly increases the spacing between the filaments. The results of the p = 0.4 bar and p = 0.2 bar are not reliable and only meant to give a hint on the dependence, since the peaks of the amplitude spectrum are not very destinct unter that pressure levels. Neverless, it can be said that the spacing ranges in between 2 mm and 4 mm for pressure levels between p = 0.6 bar and ambient pressure. A higher voltage amplitude increases the spacing during all reliable pressure levels.

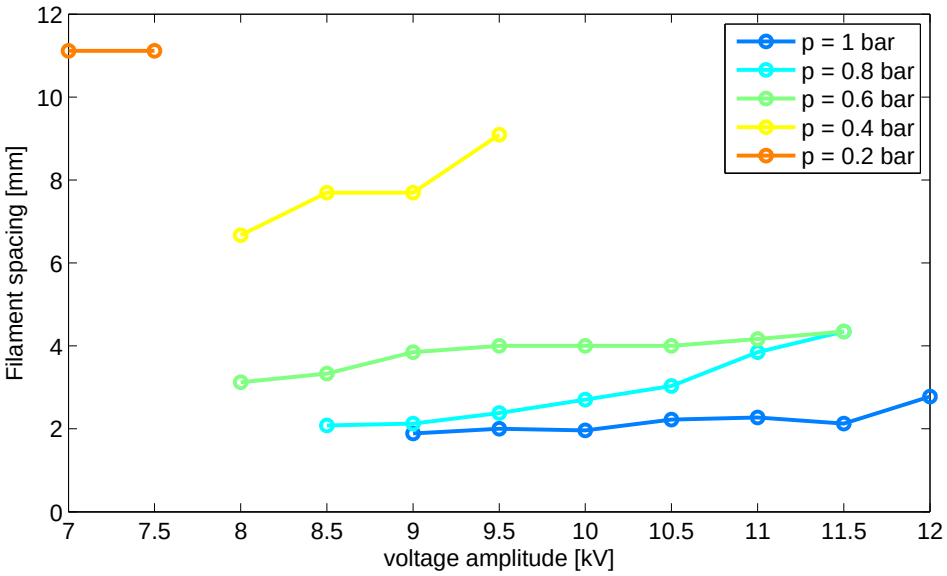

Figure 4.42: Filament spacing as function of pressure and voltage amplitude, captured for a voltage frequency of 10 kHz and ambient pressure.

Figure 4.43 shows the impact of the frequency on the filament spacing for a pressure of (a) ambient pressure and (b) p = 0.6 bar. Obviously, the spacing is strongly dependent on the voltage amplitude. A higher amplitude increases the spacing. The impact of the voltage seems to be roughly independent of pressure and frequency. The frequency seems to have a minor impact and no clear dependency, since the spacing is highest for a f = 10 kHz discharge. Both higher and smaller frequencies decrease the spacing.

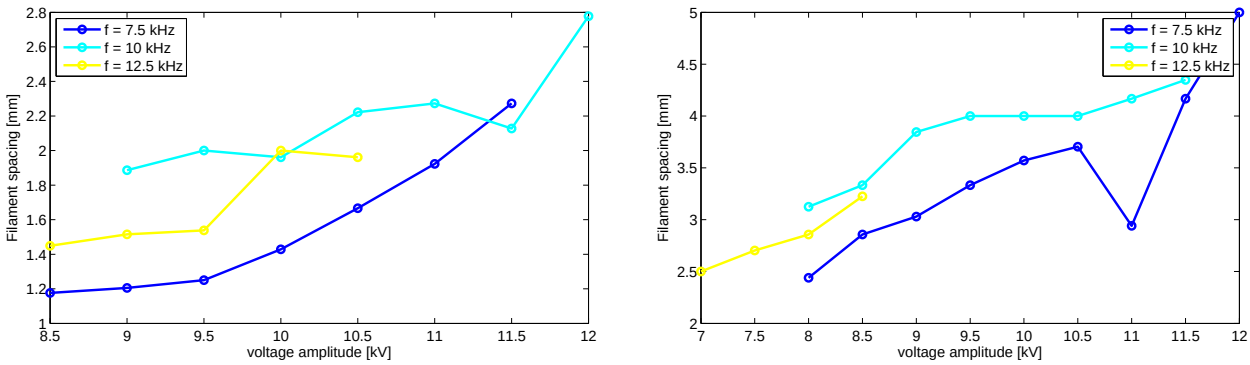

(a) (b)

Figure 4.43: Filament spacing as function of voltage amplitude and frequency for (a) ambient pressure and (b) p = 0.6 bar.

Currently, no physically satisfying theory of these effects can be provided. Therefore, more precise models of the filaments have to be developed.

4.4.3 Impact of temperature on discharge-instabilities

Within this subsection, the impact of the temperature on the onset voltage and the filament spacing will be studied.

Impact on onset voltage

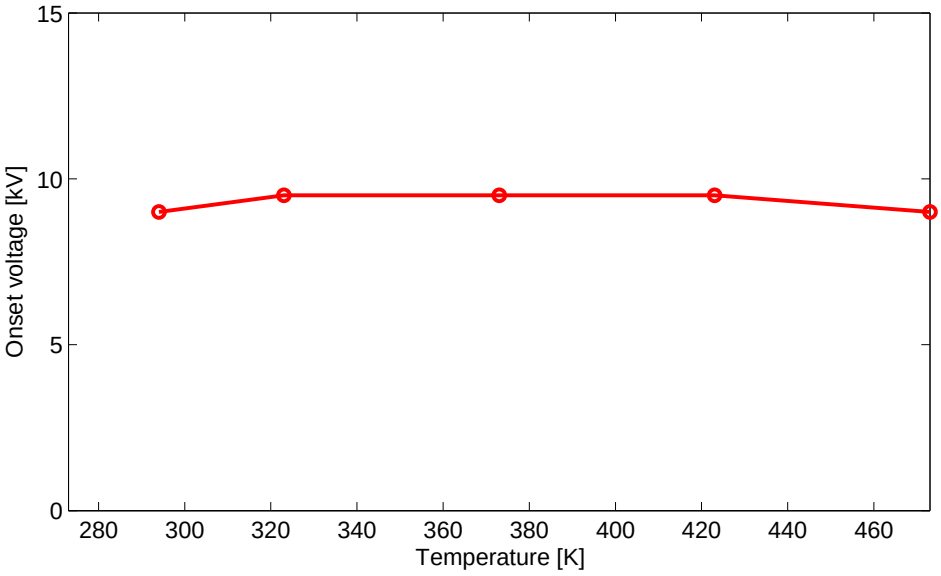

Figure 4.44: Onset voltage of the formation of filaments as function of temperature with a frequency of 10 kHz.

Figure 4.44 shows the onset voltage for discharge-filaments on the temperature. The corresponding experiments are made in the baker oven, since it allows optical access for the DSLR camera. The voltage frequency is fixed at 10 kHz. The corresponding amplitude spectra that give rise to the temperature impact can be seen in Figure 5.4 in the appendix. Obviously, the peaks in the spectra become less distinct at higher temperatures, since the filaments become smaller. Thus, the signal to noise ratio and the variance of the measurement is strongly increasing with temperature. Figure 4.44 shows that the onset voltage is roughly independent of the temperature. This effect is in good agreement to equation 2.19, since the equation is not directly dependent on the temperature. Only the adiabatic index γ shows a minor dependence on the temperature. In summary it can thus be said that increasing flow or pressure stabilize the discharge, whereas the temperature does not have a direct impact on the onset voltage.

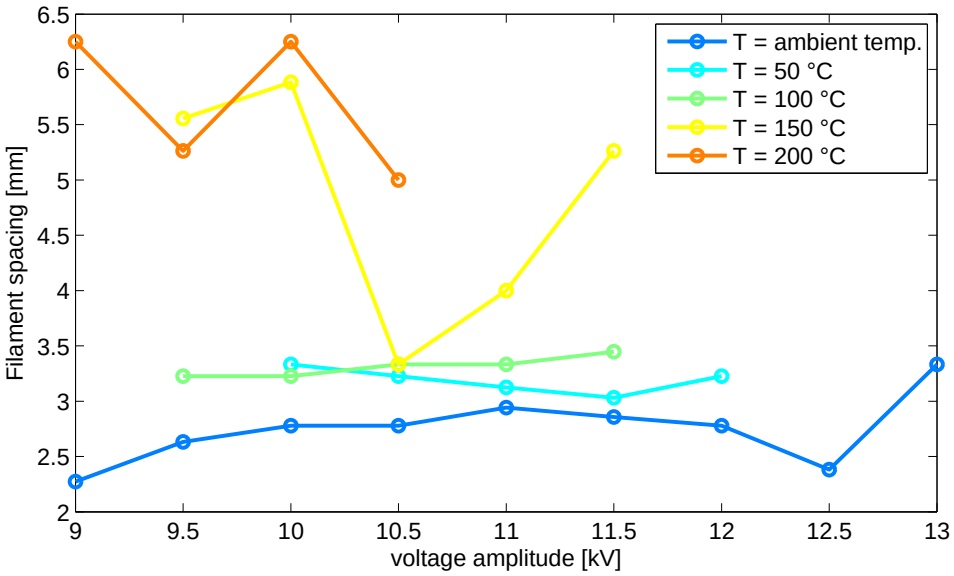

Figure 4.45: Filament spacing as function of temperature and voltage amplitude, captured for a voltage frequency of 10 kHz.

Impact on filament spacing

Figure 4.45 shows the filament spacing as function of the voltage amplitude for temperatures between ambient temperature and 200 °C. As can be seen in the corresponding amplitude spectra in Figure 5.4 in the appendix, the peaks for temperatures above 150 °C are less distinct. For 250 °C, no peaks are evident. Generally it can be said that an increasing temperature increases the filament spacing. In summary of the environmental and electric impact on the filament spacing it can be said that the spacing is increasing with increasing temperature and voltage amplitude. It is decreasing with increasing pressure. The impact of the voltage frequency does not seem to have a clear dependence. Currently, no theoretical model of the environmental and electric impact on the filamental spacing is available. In the next section, the impact of the filaments on the ionic wind will be studied.

4.5 Impact of discharge-filaments on ionic wind

Within this section, the impact of the filaments on the local velocity of the ionic wind will be studied. As proposed and shown in experiments by Bürkle [13], the formation of the filaments has an influence on the local power dissipation and thus temperature. Hence, the question is whether the increased local power consumption δjE also increases the velocity of the ionic wind, as more and faster ions are created. An increased velocity of the ionic wind would open the possibility of advanced flow control concept using the plasma actuator as vortex generator for bondary-layer control. The flow velocity behind the filaments and behind the spacing is measured in two experiments, once with a Pitot tube and once using PIV. The plasma actuator used in both experiments is a Kapton actuator, driven by a 15 kV, 10 kHz voltage in quiescent air.

Prandl tube:

The velocity of the ionic wind is measured using a *Setra Static Pressure Probe, Model 267*, as described in subsection 3.6. The measurements show that the velocity of the ionic wind in the spacing zone between the instabilities ranges from 5.2 m/s to 6.1 m/s, whereas it ranges from 6.7 m/s to 7.2 m/s within the instabilities. The ionic wind velocity of the filaments thus clearly exceeds that of the spacing in between by the factor 1.1 - 1.4.

Particle Image Velocimetry:

The flow field of the ionic wind within the filaments and the spacing in between can be seen in Figure 4.46. Obviously, shape of the flow field close to the actuator is simmilar in both regions. The wall jet of the filaments is thinner behind the filaments than behind the spacing, as the maximal velocity in the filaments is higher. In filaments, the maximal velocity is roughly 2.5 m/s, whereas that of the spacing in between is roughly 1.5 m/s. Thus, the maximal velocity of the filaments exceeds that of the spacing by the factor 1.66. This is in good agreement with the measurements of the Pitot tube, even though the velocity measured with the PIV is significantly smaller. This is probably due to an systematic error in the calibration of the PIV. Nevertheless, conclusions on the shape of the flow field and the relative velocity can be drawen.

In summary it can be said that the filaments increase the velocity of the local ionic wind by a factor of roughly 1.1 - 1.6 compared to the spacing in between. Also, the shape of the flow field is different as the wall jet of the filaments is thinner. Therefore, the flow produced by a plasma actuator with filaments is three-dimensional. This has to be taken into account in flow-control applications with a higher power consumption of the actuators, but enables advanced flow-control strategies using the three-dimensionality for the generation of vortices. As the spacing between the filaments can be adjusted by the voltage amplitude and frequency (as shown in subsection 4.4.2), the distance between the vortices could be adjusted. Future investigations have to show whether this is the case or not.

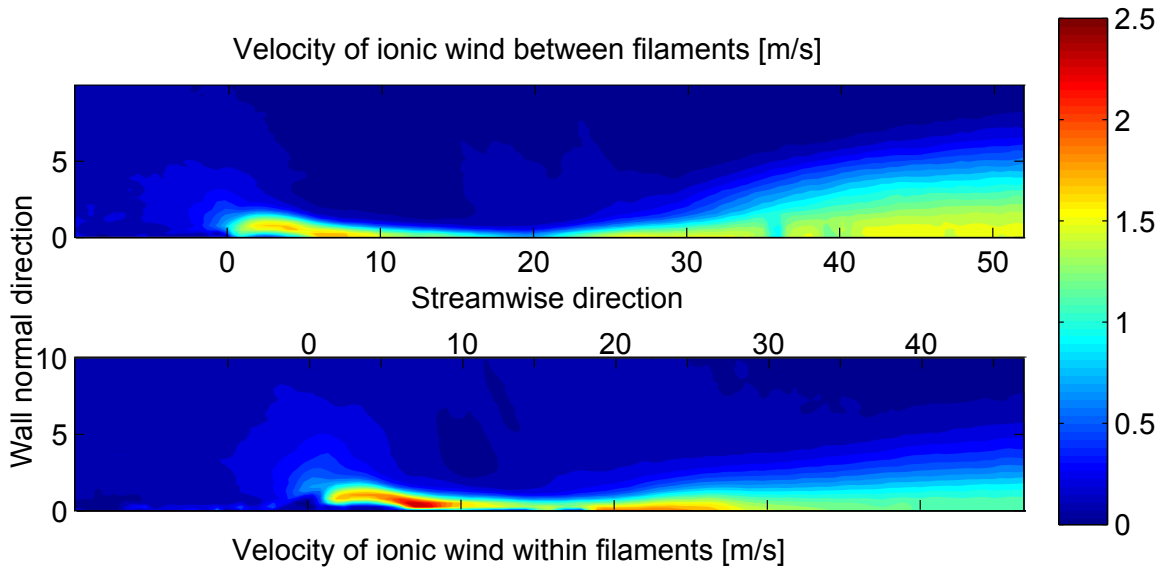

Figure 4.46: Velocity of the ionic wind within filaments and the spacing in between, measured using PIV. The voltage amplitude was 15 kV, the frequency 10 kHz.

5 Conclusions and outlook

This work shows that the environmental conditions clearly have an impact on the discharge. It was found out, that the discharge is stronger when the temperature is increased or the pressure lowered compared to ambient conditions, as the power consumption increases in both cases. The impact can be described using a power law. A new theoretical model has been proposed to explain these correlations, introducing the mean free path. The power consumption linearly increases as the mean free path of the ions is increased by a change in the environmental conditions. Additionally, the plasma length is increasing for lower pressure or higher temperature. The impact on the plasma length can also be described by a power law. The capacitance of the active actuator is pressure and temperature dependent. At higher temperature or lower pressure levels, the capacitance is increasing and thus the impedance of the plasma actuator decreasing. On one hand, flows with a high velocity decrease the discharge strength and capacitance, most likely as they blow the ions away that are needed for maintaining the discharge. The impact is stronger on discharges with high power consumption, presumably as they are more dependent on ions.

On the other hand, the flow is able to delay the formation of filaments in the discharge towards higher voltage amplitudes. Also, a higher pressure level increases the threshold for a formation of filaments. These effects follow a theoretical model in a good agreement. The temperature has no impact on the minimal voltage necessary for the formation of filaments. It was shown that an increase of the temperature or the voltage amplitude increases the spacing in between the filaments. The same effect is achieved by lowering the pressure level. Currently, no theoretical estimation of the impact of the environmental conditions on the filament spacing exists. It was clearly shown that the filaments increase the local velocity of the ionic wind and thus generate a three-dimensional flow field.

Future work should focus on the three-dimensionality of the ionic wind and the applicability of filaments for advanced flow-control. Presumably filaments induce vortices that could be used to damp disturbances in the laminar boundary layer as shown by Franson *et al.* [35] with passive vortex generators. This effect needs to be studied in detail.
In order to control the boundary layer, filaments with certain spacing are necessary. As it was shown within this work, the spacing depends on the environmental and voltage conditions. Currently, the spacing can only be determined empirically as no model of its dependence exists. Thus, a general model of the impact of voltage and environmental conditions on the spacing is necessary and should be developed in future projects. Finally, as further knowledge of the temperature impact on the plasma actuator was gained during this work, investigations on the improvement of a combustion using plasma actuators, the so-called "Plasma assisted combustion", can be performed in future.

Bibliography

[1] Roth,Xin Dai, *Optimization of the Aerodynamic Plasma Actuator as an Electrohydrodynamic (EHD) Electrical Device*, 44th AIAA Aerospace Sciences Meeting and Exhibit, AIAA 2006-1203, Reno, Nevada, USA 2006

[2] Kogelschatz, U., Eliasson, B., Egli, W., *From ozone generators to flat television screens: history and future potential of dielectric-barrier discharges*, Pure Appl. Chem., Vol. 71, No. 10, pp. 1819-1828, 1999

[3] J. R. Roth, R. C. M. Madhan, M. Yadav, et al, *Flow field measurements of paraelectric, peristaltic and combined plasma actuators based on the one atmosphere uniform glow discharge plasma (OAUGDP TM)*, Proceedings of the 42th Aerospace Sciences Meeting and Exhibit, Reno (USA), 2004

[4] Li, Y., Zhang, X., Huang, X., *The use of plasma actuators for bluff body broadband noise control*, Experiments in Fluids, 2010

[5] Jukes, N., Choi, K., Johnson, G.A., Scott, S. J., *Turbulent drag reduction by surface plasma through spanwise flow oscillation*, 3rd AIAA Flow Control Conference, volume 3, San Francisco, California, June 2006

[6] Abe, T., Takizawa, Y., Sato, S., Kimora, N., *Experimental study for momentum transfer in a dielectric barrier discharge plasma actuator*, AIAA JOURNAL Vol. 46, No. 9, September 2008

[7] Bernard, N., Moreau, E., *Effects of Altitude on the Electromechanical Characteristics of a Single Dielectric Barrier Discharge Plasma Actuator*, AIAA Plasmadynamic and Laser Conference Paper, USA, 2010

[8] Wu, Yun; Li, Yinghong; Jia, Min et al *Influence of operating pressure on surface dielectric barrier dischaerge plasma aerodynamic actuation characteristics*, Air Force Engineering University Xi'an and Tshinguan University, Bejing, Peoples Republic of China, Applied Physics Letters 93,031503, 2008

[9] Versailles, P., Gingras-Gosselin, V., Duc Vo, H., *Impact of Pressure and Temperature on the Performance of Plasma Actuators*, AIAA Vol. 48, No. 4, April 2010

[10] Barckmann, K., Kriegseis, J., Grundmann, S., Tropea, C., *Dielectric-barrier discharge plasmas for flow control at higher Mach numbers*, 5th Flow Control Conference, Chicago, Illinois, USA, 2010

[11] Kriegseis, Benjamin, Grundmann,Tropea, "*Capacitance and power consumption quantification of dielectric barrier discharge (DBD) plasma actuators*", Journal of Electrostatics 69 (2011) 302e312, 2011

[12] Kriegseis, J., Kurz, A., Duchmann, A., Grundmann, S., Tropea, C.,*Influence of air flow on the performance of DBD Plasma Actuators*, 50th AIAA Aerospace Sciences Meeting, January 9-12, Nashville, Tennessee , USA

[13] Bürkle, S., *On the nature and behavior of filaments in the dielectric barrier discharge of plasma actuators*, physics-master thesis, TU Darmstadt, January 2013

[14] H. Kegel *Plasmaphysik: Eine Einführung*, ISBN-10: 354063701X, Springer Berlin Heidelberg, 1. Auflage, Germany, 1998

[15] Kriegseis, Jochen; *Performance Characterization and Quantification of Dielectric Barrier Discharge Plasma Actuators*, Dissertation, Germany, 2011

[16] Raizer, Yuri P. *Gas Discharge Physics*, Springer-Verlag, Germany, 1991

[17] Pavon, Samantha *Interaction Between a Surface Dielectric Barrier Discharge and Transonic Airflows*, PhD - Thesis N° 4201, EPFL, Switzerland, 2008

[18] Choi, Jai Hyuk; Lee, Tae Il; Han, Inho et al. *Investigation of the transition between glow and streamer discharges in atmospheric air*, Yonsei University, Seoul, Institute of Physics Publishing, Plasma Sources Science and Technology, doi 10.1088/0963-0252/15/3/017, 2005

[19] Benard, Nicolas; Pons, Jerome; Audier, Pierre et al. *Filaments in a Surface Dielectric Barrier Discharge operating in Altitude Conditions* IEEE Transactions on Plasma Science, Volume 39, No. 11, November 2011

[20] Soloviev, V.R., *Analytical estimation of the thrust generated by a surface dielectric barrier discharge*, Moscow Institute of Physics and Technology, IOP Publishing, Russia, IOP Publishing, doi 10.1088/0022-3727/45/2/025205, 2012

[21] Pavon, Dorier, Hollenstein, Ott, Leyland *Effects of high-speed airflows on a surface dielectric barrier discharge*, J. Phys. D: Appl. Phys. 40 1733 - 1741, Switzerland, 2007

[22] Orlov, Font, Edelstein, *Characterization of Discharge Modes of Plasma Actuators*, AIAA Journal, 46(12):3142 - 3148, USA, 2008

[23] Meek,J. M., Craggs, J. D. , *Electrical breakdown of gases*, Clarendon Press, 1953

[24] Leonov, S.; Opaits, D.; Miles, R and Soloviev, V *Time resolved measurents of plasma induced momentum in air and nitrogen under dielectric barrier discharge actuation*, Phys. Plasmas No. 17, 113505, 2010

[25] Moreau, Eric *Airflow control by non-thermal plasma actuators*, J. Phys. D: Appl. Phys. 40 605, 2007

[26] Forte, M; Jolibois, J; Pons, jerome et al. *Optimization of a Dielectric Barrier Discharge Actuator by stationary and non- stationary Measurements of the induced flow Velocity; application to airflow control*Exp. Fluids No. 43, 917-28, 2007

[27] Roth, R., Rahel, J., Dai, X., Sherman, D., *The physics and phenomenology of one atmosphere uniform glow discharge plasma reactors for surface treatment applications*, Journal of Physics: Applied Physics, 38:555-567, 2005

[28] Yang, X.,Zhitao, Z., Cheng, L., Yu, X., *Effect of systematic resonance on dbd device*, Plasma Science and Technology, 7(5):3030, 2005

[29] Brauer, I.; Punset, C.; Purwins, H.-G,; Boef, J.P., *Simulations of self-organized filaments in a dielectric barrier glow discharge plasma*"', journal of applied physics Volume 85, Number 11, 1999

[30] Chirokov, Alexandre V., *Stability of Atmospheric Pressure Glow Discharges*, PhD Thesis, Drexel University, 2005

[31] Velikhov, E. P.; Golubev, V. S.; Pashkin, S. V., *Glow discharge in a gas flow*, Sov. Phys. Usp. 25 340-358, 1982

[32] Lagmich, Callegari, Pitchford and Boeuf, *Model description of surface dielectric barrier discharges for flow control*, J. Phys. D: Appl. Phys. 41 (2008) 095205 (10pp), 2008

[33] http://www.csi.tu-darmstadt.de/institute/dcc/facilities/trisonicwindtunnel/index.en.jsp 15.1.2013

[34] Raffel, M., Willert, C. *et al*, *Particle Image Velocimetry: A Practical Guide*, 10th edition, Springer print, l998

[35] Franson, J. *et al.*, *Delaying Transition to Turbulence by a Passive Mechanism*, PRL 96, 064501 Physical Review Letters, 2006

Appendix

Resonance curves of a ceramic actuator for temperatures between ambient temperature and T = 600 °C. The input voltage is chosen to lead to power consumptions of 2.5 W, 5 W, 7.5 W, 10 W, 15 W, 20 W, 30 W and 40 W, respectively, at a voltage frequency of f = 10 kHz.

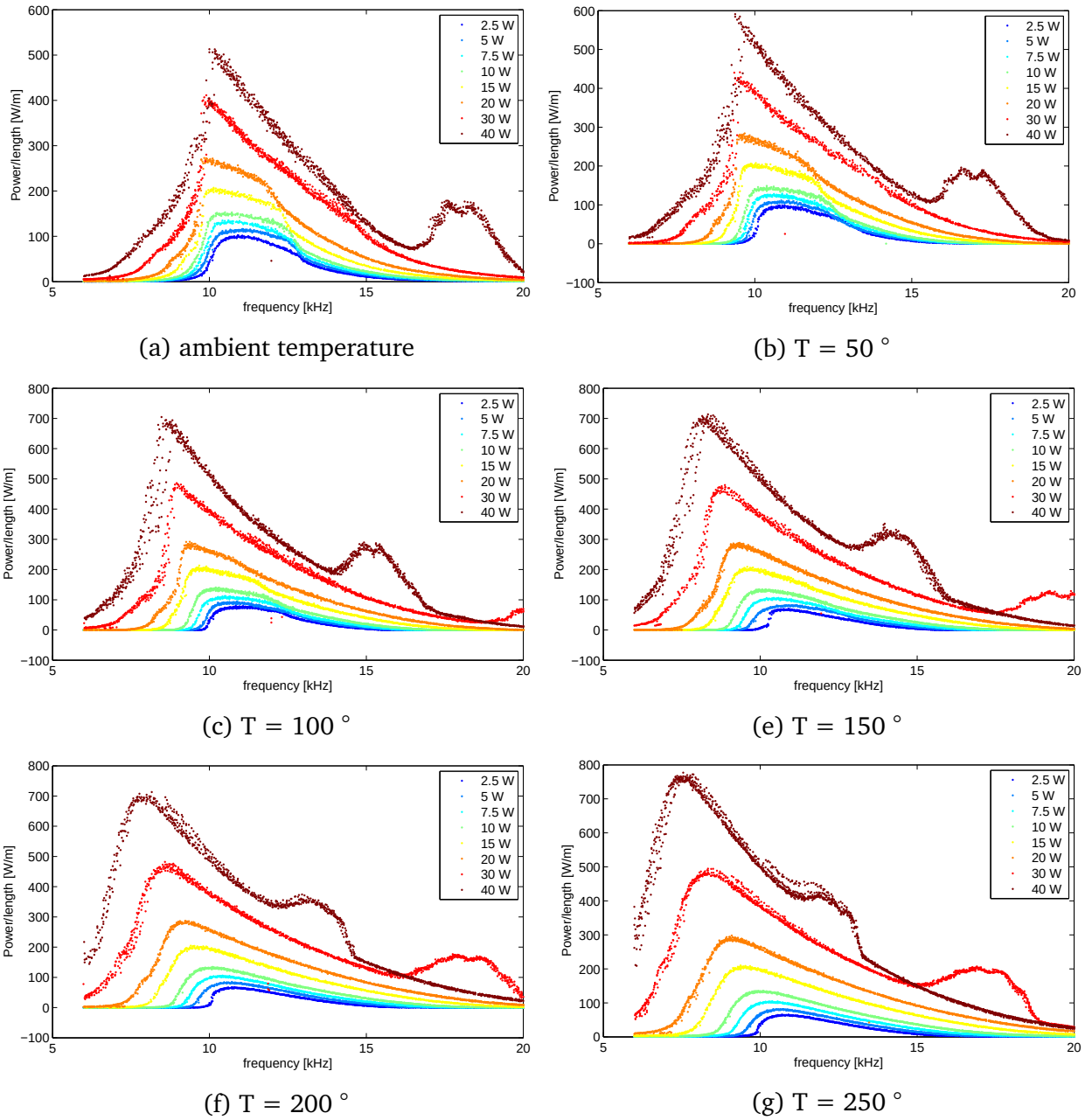

(a) ambient temperature

(b) T = 50 °

(c) T = 100 °

(e) T = 150 °

(f) T = 200 °

(g) T = 250 °

Figure 5.1: Resonance curves for temperatures in between ambient temperature and 250 °C and for different input voltages, all measured in the baker oven.

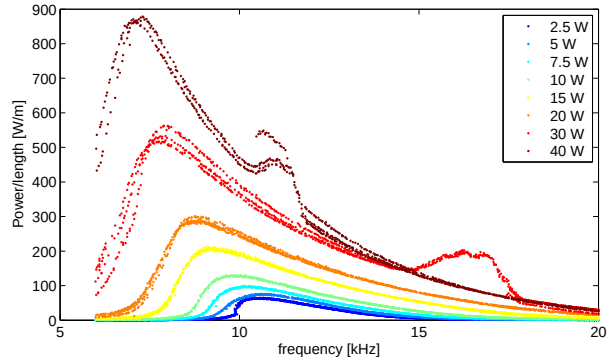

(a) T = 300 °C

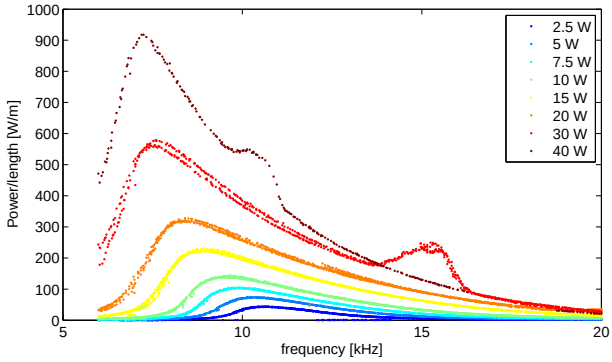

(b) T = 350 °C

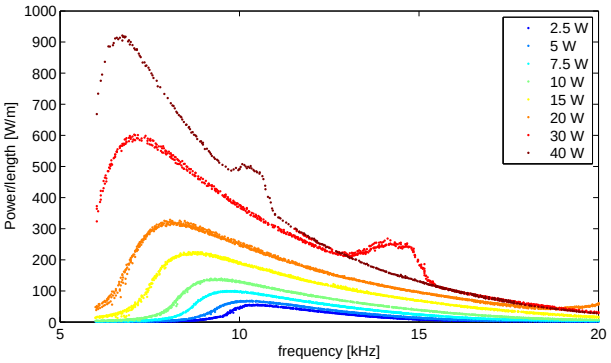

(c) T = 400 °C

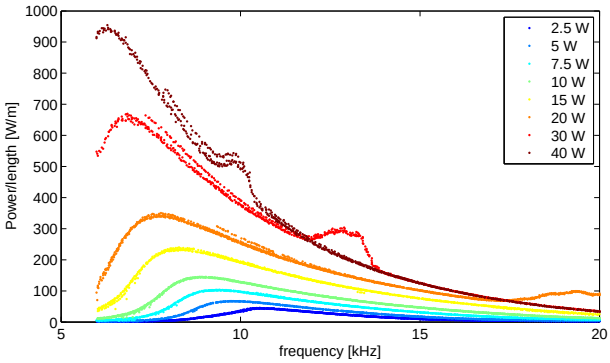

(e) T = 450 °C

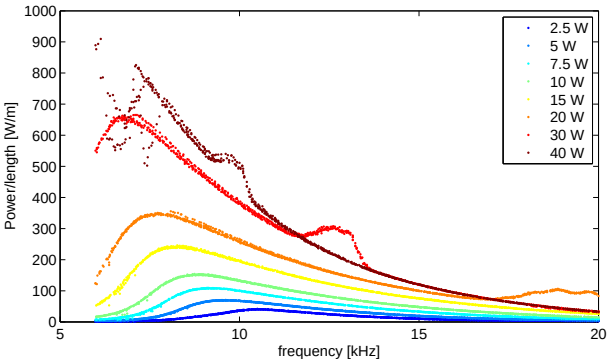

(f) T = 500 °C

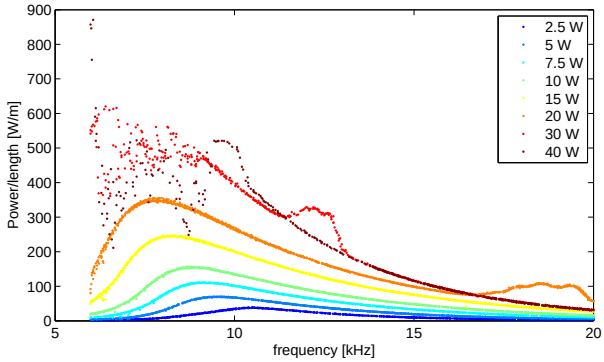

(g) T = 550 °C

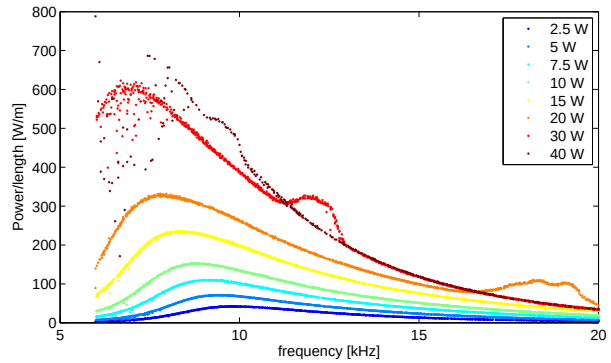

(g) T = 600 °C

Figure 5.2: Resonance curves for temperatures in between 300 °C and 600 °C, for different input voltages.

Single sided amplitude sprectra of the discharge's grayscale-intensity, captured with a *Nikon D 70 coolpix*. The curves correspond to different voltage amplitudes on the actuator.

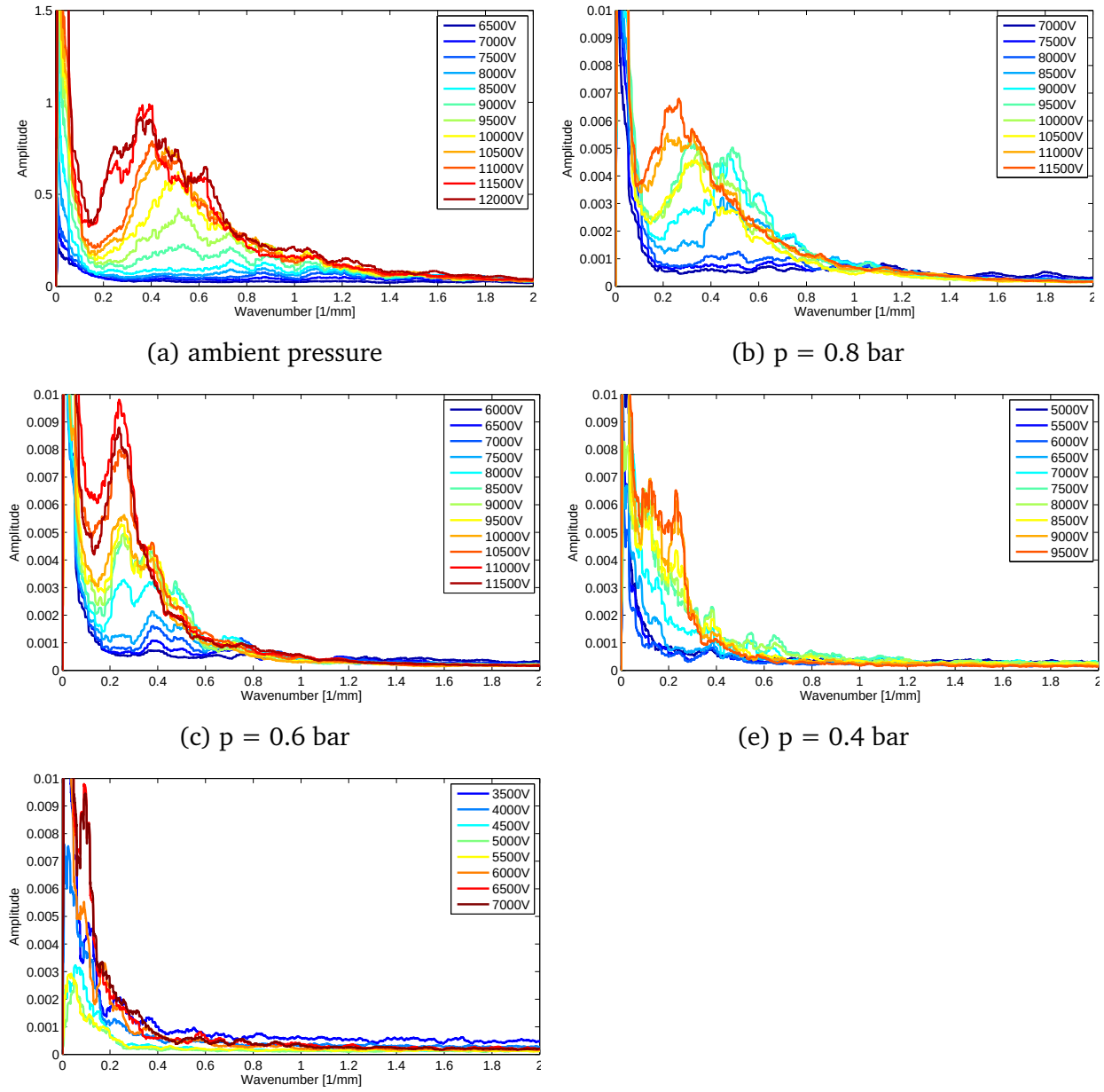

(a) ambient pressure

(b) p = 0.8 bar

(c) p = 0.6 bar

(e) p = 0.4 bar

(f) p = 0.2 bar

Figure 5.3: Amplitude spectra of the discharge under different voltage amplitudes and pressure levels between p = 0.2 bar and ambient pressure. The voltage frequency is fixed at f = 10 kHz.

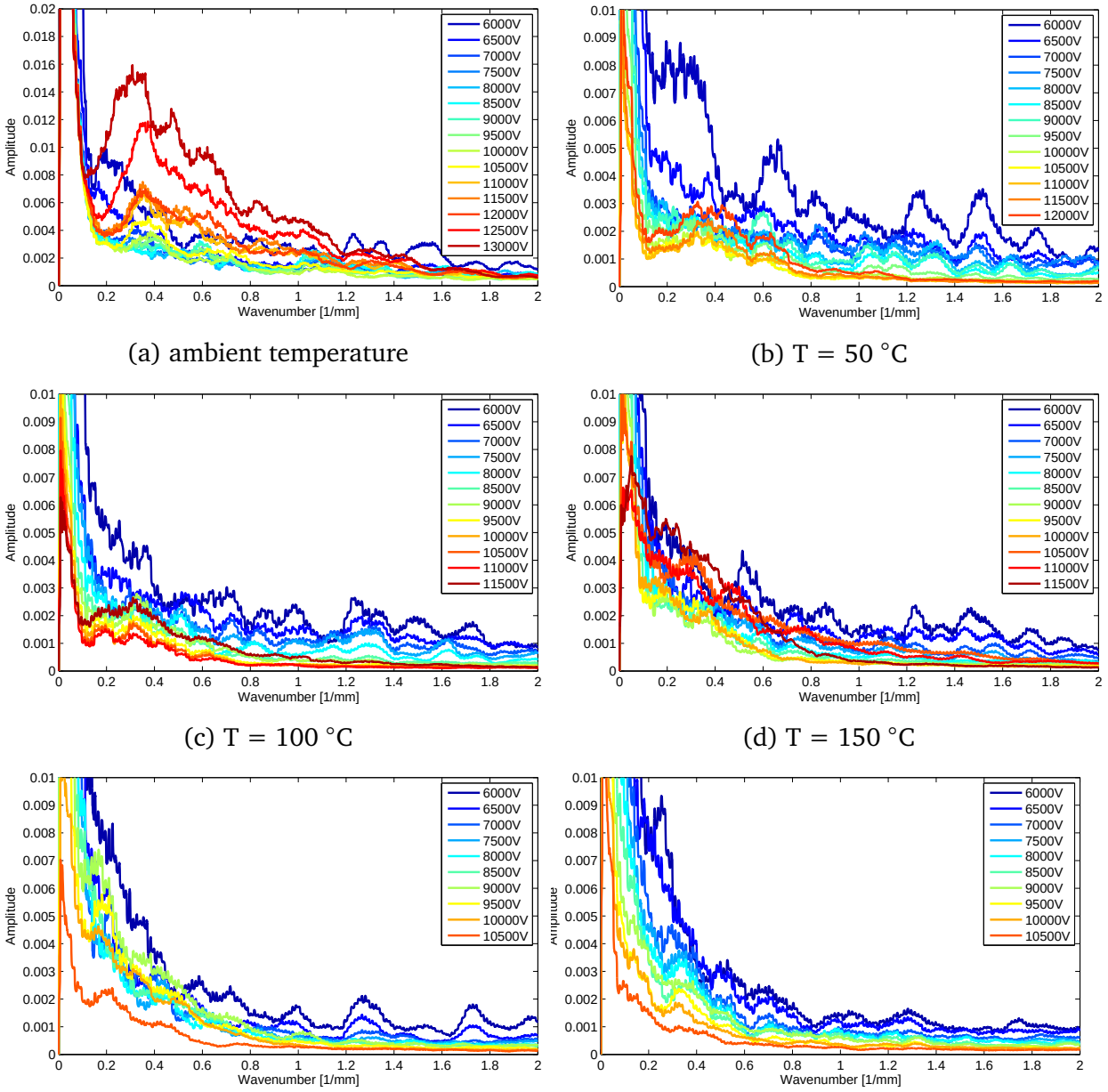

(a) ambient temperature

(b) T = 50 °C

(c) T = 100 °C

(d) T = 150 °C

(e) T = 200 °C

(f) T = 250 °C

Figure 5.4: Amplitude spectra of the discharge under different voltage amplitudes and temperatures between ambient temperature and T = 250 °C. The voltage frequency is fixed at f = 10 kHz.

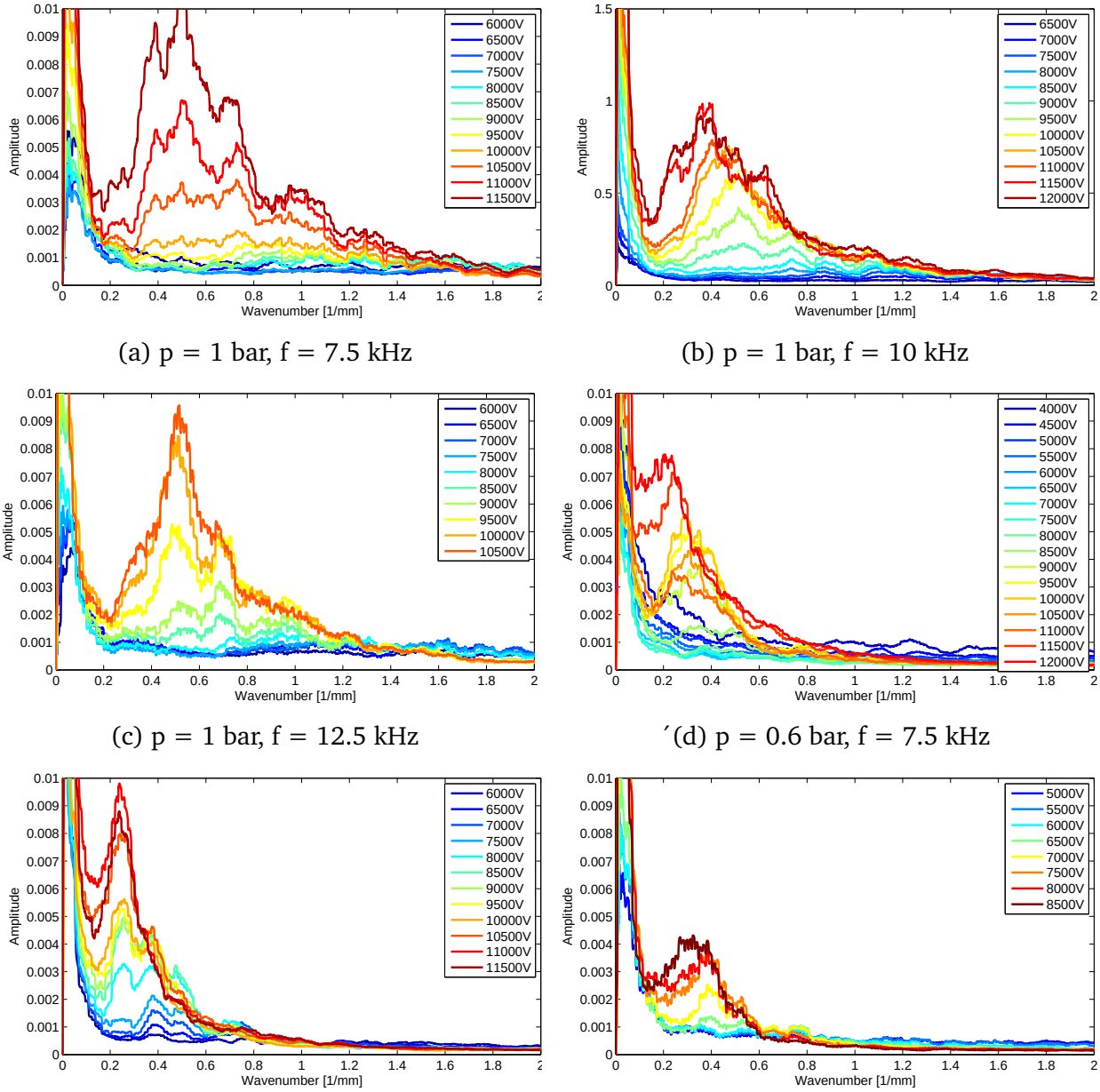

(a) p = 1 bar, f = 7.5 kHz

(b) p = 1 bar, f = 10 kHz

(c) p = 1 bar, f = 12.5 kHz

´(d) p = 0.6 bar, f = 7.5 kHz

(e) p = 0.6 bar, f = 10 kHz

(f) p = 0.6 bar, f = 12.5 kHz

Figure 5.5: Amplitude spectra of the discharge under different voltage amplitudes and frequencies. The experiments were made at p = 0.6 bar and under ambient pressure, respectively.